Synthetic carbohydrate-based materials as models to describe natural carbohydrate assemblies

Inaugural-Dissertation

To obtain the academic degree

Doctor rerum naturalium (Dr. rer. nat.)

submitted to the Department of Biology, Chemistry, Pharmacy

of Freie Universität Berlin

by

Soeun Gim

from Busan/Republic of Korea

2021

This work was performed between September 2017 and September 2021 under the supervision of Dr. Martina Delbianco and Prof. Dr. Peter H. Seeberger in the Department of Biomolecular Systems, Max Planck Institute of Colloids and Interfaces Potsdam, and the Institute of Chemistry and Biochemistry, Freie Universität Berlin. I declare that this dissertation is an original report of my research and has been finished by myself. All contributions from colleagues and collaborators have been indicated clearly and acknowledged.

1st reviewer: Prof. Peter H. Seeberger

2nd reviewer: Prof. Rainer Haag

Date of oral defense: 6th, December, 2021

Acknowledgement

I would like to express my deepest gratitude to Dr. Martina Delbianco for the supervision of my PhD study, for her patience in providing me with suggestions on research, and for her continuous support on this thesis.

I would like to thank Prof. Dr. Peter H. Seeberger for providing me the opportunity to work and offering the excellent research environment in Department of Biomolecular Systems at the Max-Planck-Institute of Colloids and Interfaces and for reviewing this thesis.

I am also grateful to Prof. Dr. Rainer Haag for kindly agreeing to review this thesis.

I would like to thank all former and current members of carbohydrate materials group, Dr. Yang Yu, Dr. Vittorio Bordoni, Dr. Yuntao Zhu, Dr. Denisa Vargová, Dr. Manishkumar Chaube, Giulio Fittolani, Theodore Tyrikos-Ergas, Zhouxiang Zhao, Jhih-Yi Huang, Surusch Djalali, Marlene Dal Colle, for their help in the lab work, valuable discussion, proofreading of all the papers and the thesis, and warm atmosphere. I really enjoyed co-working with the group members and especially thank Dr. Yang Yu, Dr. Yuntao Zhu, Giulio Fittolani, Theodore Tyrikos-Ergas, and Jhih-Yi Huang, for providing valuable carbohydrate materials. I also want to thank Theodore Tyrikos-Ergas for computer simulation and Surusch Djalali for translating the summary of the thesis.

I want to acknowledge my external collaborator, Dr. Yu Ogawa (CERMAV, Grenoble, France), for microcrystal electron diffraction and electron tomography.

I want to thank the technicians and colleagues, Eva Settels and Olaf Niemeyer for kind introduction and maintenance, Heike Runge, Rona Pitschke, Bolortuya Badamdorj, Dr. Tobias Heil, and Dr. Nadja Tarakina for electron microscopes, Daniel Werner for X-ray diffractograms, Carmen Remde for confocal microscope, Dr. Oleksandr Savatieiev for fluorescence spectrometry, Gunho Song for circular dichroism, Reinhild Dunnebacke for atomic force microscope. I am also grateful to Dorothee Bohme for the help with administrative works. I would like to thank all members of Department of Biomolecular Systems.

I would like to thank my family and friends in South Korea for their love and encouragement. Last but not least, I send my deepest gratitude to Hanhee for his help, patience, and support all the time.

Table of Contents

Summary

Nature is based on self-assembling systems that generate functional structures. Inspired by nature, programmable artificial architectures have been developed, often making use of synthetic peptides and nucleic acids. In contrast, only limited examples of programmable carbohydrate assemblies have been reported. This can be partially ascribed to the limited knowledge of carbohydrates' structure. Structural complexity, heterogeneity of natural carbohydrate samples, and the lack of suitable analytical techniques have prevented the molecular level description of carbohydrate materials. The introduction of synthetic model systems, able to generate chemically defined assemblies, could help the understanding of carbohydrate materials. Here, simple and well-defined oligosaccharides were employed to create model systems to study supramolecular carbohydrate-based assemblies and produce useful data for the formation of tailor-made materials. This approach also shined light on the interactions involved in the formation of natural systems, such as bacterial biofilms, where carbohydrate and peptides interact to form valuable nanocomposites.

In chapter 2, I investigated the supramolecular structure formation of synthetic oligosaccharides. Systematic variation in their chain length, substitution pattern, and glycosidic linkages, generated distinctive morphologies, including spherical particles or fiber-like structures. The compounds showed unique intrinsic optical properties (e.g. red edge excitation shift), highly dependent on their aggregation status. Potential applications of glycomaterials in bioimaging and optical devices are envisioned.

Among these six compounds, disaccharide **13** (**13-D** in chapter 3), growing into needle-like structures, offered the perfect model system to explore details of oligosaccharide assemblies and optimize analytical techniques to study carbohydrate materials. The stability of the assembly enabled the implementation of microcrystal electron diffraction (MicroED) for oligosaccharide samples. This technique allowed for the reconstruction of the crystal unit cell and permitted correlating the local molecular organization with the supramolecular assembly. Synthetic analogous of compound **13** with specific single-site modifications were designed to identify key stabilizing interactions. The combination of organic chemistry and electron diffractions methods will be implemented to reveal molecular details of natural polysaccharide assemblies.

In chapter 4, a new model system was introduced to study bacterial biofilms, nanocomposites of cellulose and proteins (e.g. curli fibers). Specific *E. Coli* strains produce phosphoethanolamine (pEtN) cellulose as part of their protective biofilms, providing increased adhesion. I employed synthetic peptides and oligosaccharides to generate artificial biofilm and study the role of pEtN cellulose in biofilm formation. Different amounts and patterns of pEtN substitution in the oligosaccharide modulated the length and aggregation tendency of the peptide fibers. The mechanical properties of the protein-carbohydrate network were affected by the chemical nature of the carbohydrate component, with high adhesion measured for highly substituted pEtN cellulose analogues. Synthetic oligosaccharides able to interrupt fibrillary assembly

were identified and could serve as promising drug candidates for the treatment of neurological diseases or as antibacterial agents.

Overall, the synthetic oligosaccharide models presented in this thesis will establish the foundation of our understanding of carbohydrate interactions in nature and will promote several applications of carbohydrate materials in nanobiotechnology.

Zusammenfassung

Die Natur basiert in großen Teilen auf selbstorganisierenden Systemen, die funktionelle Strukturen erzeugen. Durch diese inspiriert, entwickelten sich programmierbare künstliche Architekturen, die in der Regel auf synthetischen Peptiden und Nukleinsäuren basieren. Auf Seiten der Kohlenhydrate sind nur wenige Beispiele zu programmierbaren Systemen bekannt. Dies ist teilweise auf das begrenzte Wissen über die Struktur-Wirkungsbeziehung von Kohlenhydraten zurückzuführen. Vor allem die strukturelle Komplexität und die Heterogenität der natürlichen Kohlenhydratproben sowie das Fehlen geeigneter Analysetechniken stellen die Beschreibung von Kohlenhydratmaterialien auf molekularer Ebene als eine Herausforderung dar. Synthetische Modellsysteme mit einer wohldefinierten chemischen Struktur, könnten zum besseren Verständnis von Kohlenhydratmaterialien beitragen. In dieser Arbeit wurden einfache und wohldefinierte Oligosaccharide aufgebaut und als Modellsysteme für supramolekulare Verbindungen auf Kohlenhydratbasis verwendet. Mit Hilfe dieser konnten nützliche Daten für die Bildung maßgeschneiderter Materialien gewonnen werden. Darüber hinaus erlaubt der Ansatz die fundamentalen Wechselwirkungen zwischen Kohlenhydraten und Peptiden zu beleuchten, die während der Bildung von natürlichen Systemen wie bakterieller Bio-Filme auftreten.

Im zweiten Kapitel wurde die supramolekulare Strukturbildung von synthetischen Oligosacchariden untersucht. Durch die systematische Variation der Kettenlänge, des Substitutionsmusters und der Art der glykosidischen Bindungen wurden Strukturen mit kugelförmiger bis hin zu faserartiger Morphologie erzeugt. Diese Verbindungen weisen einzigartige intrinsische optische Eigenschaften auf (z. B. red edge excitation shift), die stark von ihrer Aggregation abhängen. Eine potenzielle Anwendung dieser Glykomaterialien könnte die biologische Bildgebung in optischen Geräten darstellen.

Von den sechs untersuchten Verbindungen bildet das Disaccharid **13** (**13-D** in Kapitel 3), welches in nadelartigen Strukturen heranwächst, das perfekte Modellsystem zur Erforschung des Selbstorganisationsprozesses von Oligosacchariden und zur Optimierung entsprechender analytischer Methoden. Dank der hohen Stabilität des Aggregats konnte die Technik der Mikrokristall-Elektronenbeugungstechnik (MicroED) verwendet werden. Diese ermöglicht die Rekonstruktion der Elementarzelle des Kristallgitters sowie die lokale, molekulare Ordnung mit dem supramolekularen Aufbau zu korrelieren. Des Weiteren wurden synthetische Analoga von Verbindung **13** mit spezifischen Modifikationen entwickelt, mit denen wichtige stabilisierende Wechselwirkungen untersucht werden konnten. Dabei wurden das Wissen der organischen Chemie und die Methoden der Elektronenbeugung kombiniert eingesetzt, um die molekularen Einzelheiten natürlicher Polysaccharidanordnungen zu erforschen.

Im vierten Kapitel wurde ein neues Modellsystem zur Untersuchung von bakteriellen Biofilmen und Nanokompositen aus Cellulose und Proteinen (z. B. Curli-Fasern), eingeführt. Bestimmte E. Coli-Stämme produzieren Phosphoethanolamin (pEtN)-Cellulose als Teil ihres schützenden Bio-Filmes und sorgen so

für eine erhöhte Adhäsion. Es wurden künstlichen Biofilme aus synthetischen Peptiden und Oligosacchariden erzeugt um damit die Rolle der pEtN-Cellulose bei der Biofilmbildung zu untersuchen. Dabei konnte ein Zusammenhang zwischen der Menge und dem Muster der pEtN-Substitution im Oligosaccharid, und der Länge sowie der Aggregationstendenz der Peptidfasern festgestellt werden. Die mechanischen Eigenschaften des Protein-Kohlenhydrat-Netzwerks wird dabei stark durch die chemische Beschaffenheit der Kohlenhydratkomponente bestimmt – ein hoher pEtN-Substitutionsgrad der Cellulosebestandteile führt zu einer erhöhten Adhäsion. Des Weiteren konnten synthetische Oligosaccharide identifiziert werden, deren Fibrillen-Bildung unterbrochen ist. Diese könnten als Basis für vielversprechende Arzneimittelkandidaten bei der Behandlung neurologischer Erkrankungen oder als antibakterielle Wirkstoffe dienen.

Zusammenfassend werden die in dieser Arbeit vorgestellten synthetischen Oligosaccharidmodelle zu dem Grundverständnis der Kohlenhydratinteraktionen in der Natur beitragen und dabei unterschiedlichste nanobiotechnologische Anwendungen von Kohlenhydratmaterialien unterstützen.

List of Publications

Scientific Publications and Reviews

1. **S. Gim**, G. Fittolani, Y. Yu, Y. Zhu, P. H. Seeberger, Y. Ogawa, M. Delbianco, Targeted chemical modifications identify key features of carbohydrate assemblies and generate tailored carbohydrate materials. *Chem. Eur. J*., **2021**, 27(52), 13139-13143.

2. **S. Gim**, G. Fittolani, Y. Nishiyama, P. H. Seeberger, Y. Ogawa, M. Delbianco, Supramolecular assembly and chirality of synthetic carbohydrate materials. *Angew. Chem. Int. Ed.,* **2020**, 132(50), 22766-22772.

3. J. Zhang, **S. Gim**, G. Paris, P. Dallabernardina, C. N. Z. Schmitt, S. Eickelmann, F. F. Loeffler, Ultrasonic-assisted synthesis of highly defined silver nanodimers by self-assembly for improved surface-enhanced raman spectroscopy. *Chem. Eur. J*., **2020**, 26(6), 1243-1248.

4. Y. Yu[‡], **S. Gim**[‡], D. Kim, Z. A. Arnon, E. Gazit, P. H. Seeberger, M. Delbianco. Oligosaccharides self-assemble and show intrinsic optical properties. *J. Am. Chem. Soc*., **2019**, 141(12), 4833-4838.
[‡]Equal contribution

5. **S. Gim**, Y. Zhu, P. H. Seeberger, M. Delbianco, Carbohydrate-based nanomaterials for biomedical applications. *WIREs Nanomed. Nanobiotechnol.*, **2019**, 11, e1558.

Scientific Conferences and Symposia Presentations:

1. Jul. 2020 RSC Carbohydrate Webinar, Oral Presentation
2. Sep. 2019 International Symposium of SFB 765, Berlin (Germany), Poster presentation
3. Oct. 2018 2nd JCF Potsdam PhD symposium, Potsdam (Germany), Oral presentation

List of Abbreviations

Ace	acetone
AFM	atomic force microscopy
AGA	automated glycan assembly
Amimcl	1-*N*-alkyl-3-methylimidazolium chloride
Bmimcl	1-*N*-butyl-3-methylimidazolium chloride
Bn	benzyl
BNC	bacterial nanocellulose
BSE	backscattered electrons
CA	cellulose acetate
CCI	carbohydrate-carbohydrate interaction
CD	circular dichroism
CMC	carboxymethyl cellulose
CNC	cellulose nanocrystal
CPI	carbohydrate-protein interaction
Cryo-SEM	cryogenic scanning electron microscopy
Cryo-TEM	cryogenic transmission electron microscopy
DA	degree of acetylation
DMAc	dimethylacetamide
DLS	dynamic light scattering
EC	ethyl cellulose
ED	electron diffraction
EM	electron microscopy
ESEM	environmental scanning electron microscopy
F-D	force-distance
FF	diphenylalanine
FTIR	fourier transform infrared
HFIP	hexafluoroisopropanol
HPC	hydroxypropylcellulose
*i*PrOH	isopropanol
IR	infrared
LMWG	low molecular weight gelator

MicroED	microcrystal electron diffraction
NC	nanocellulose
NFC	nanofibrillated cellulose
NMR	nuclear magnetic resonance
pEtN	phosphoethanolamine cellulose
PFB	pentafluorobenzyl
POM	polarized optical microscopy
PSD	photodiode sensor deflection
QI	qualitative imaging
SANS	small angle neutron scattering
SAXS	small angle X-ray scattering
SD	standard deviation
SE	secondary electron
SEM	scanning electron microscopy
SPM	scanning probe microscopy
ssNMR	solid state nuclear magnetic resonance
TEM	transmission electron microscopy
ThT	thioflavin T
TOCSY	total correlation spectroscopy
UV	ultraviolet
VUV	vacuum ultraviolet
XRD	X-ray diffraction

1. Introduction

This chapter has been modified in part from the following articles:

S. Gim, G. Fittolani, Y. Yu, Y. Zhu, P. H. Seeberger, Y. Ogawa, M. Delbianco. Targeted chemical modifications identify key features of carbohydrate assemblies and generate tailored carbohydrate materials. *Chem. Eur. J.*, **2021**, 27(52), 13139-13143.

S. Gim, G. Fittolani, Y. Nishiyama, P. H. Seeberger, Y. Ogawa, M. Delbianco. Supramolecular assembly and chirality of synthetic carbohydrate materials. *Angew. Chem. Int. Ed.,* **2020**, 132(50), 22766-22772.

Y. Yu[‡], **S. Gim**[‡], D. Kim, Z. A. Arnon, E. Gazit, P. H. Seeberger, M. Delbianco. Oligosaccharides self assemble and show intrinsic optical properties. *J. Am. Chem. Soc*., **2019**, 141(12), 4833-4838.
[‡]Equal contribution

S. Gim, Y. Zhu, P. H. Seeberger, M. Delbianco. Carbohydrate-based nanomaterials for biomedical applications. *WIREs Nanomed. Nanobiotechnol.*, **2019**, 11, e1558.

1.1. Self-assembly

Nature is based on self-assembling systems, resulting in highly complex and dynamic architectures.[1] Individual components are able to relocate and remodel to generate ordered structures. Classical examples include nucleic acids and proteins, able to fold to offer specific functions, and phospholipids, able to align forming cell membranes. The process is not only limited to nature, but it has also been applied to produce functional materials with applications in nanotechnology, medicine, and catalysis.[2]

The formation and stabilization of supramolecular nanostructures are mediated by non-covalent interactions, such as electrostatic, van der Waals, π-π, and hydrophobic interactions, as well as hydrogen and coordination bonds (**Figure 1-1A**).[3] These noncovalent interactions are weaker than typical covalent bonds, in a range of few kJ/mol to several hundreds of kJ/mol depending on the type of interactions, yet they can act at longer distances promoting the formation of molecular clusters.[4] These weak interactions can be enhanced with multivalency, increasing the numbers of interactions.[5]

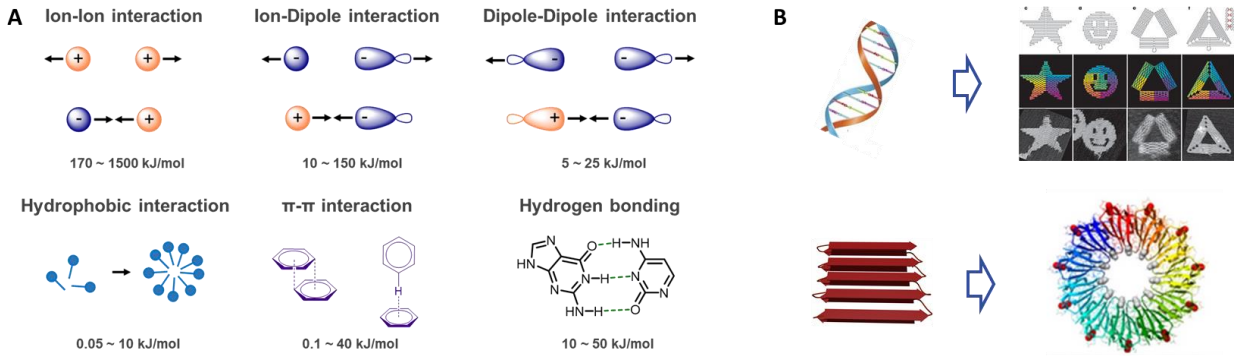

Figure 1-1. (A) Examples of the non-covalent interactions. (B) Self-assemblies in nature (left) and artificial systems (right) based on nucleic acids (top) and peptides (bottom). Adapted with permission from Rothemund[6] Copyright (2006) Springer Nature and Malay et al.[7] Copyright (2019) Springer Nature.

Inspired by nature, several artificial systems based on simple peptides[8] and nucleic acids[9] have been generated (**Figure 1-1B**). These systems can spontaneously self-assemble to form defined supramolecular architectures which are the essence of modern nanotechnology, with implications in the medical[10] and energy[8d, 11] fields. Assembly of DNAs is highly programmable due to a high degree of fidelity, predictability, and directionality with its base pairing rules.[12] DNA origami, the nanoscale folding of DNA, is a good example showing precise controllability of high-order architectures.[13] A similar approach was adapted to the rational design of protein folding.[14] Linear polypeptide chains can fold into defined three-dimensional structures and generate secondary and tertiary structures that can be modulated by carefully planning the amino-acid sequences. Computational simulations guide the structural design and analytical techniques are well-established to analyze the resulting assemblies.[15]

In contrast to DNAs and peptides, examples of supramolecular materials based on carbohydrates are rare. This can be partially ascribed to the limited knowledge available on carbohydrate three-dimensional structures and conformations. Moreover, natural carbohydrates exist as polydisperse samples with multiple lengths and branching, making the analysis, reproducibility and quality control of such materials very difficult. Due to the single chain flexibility, a detailed 3D investigation as well as defined structure-function correlations are still lacking. In addition, chemical modifications that serve to tune the polysaccharides' properties suffer from low regioselectivity, increasing the sample polydispersity even further.[16] Simple model systems based on well-defined oligosaccharides are highly needed to reveal the relationship between molecular structure, aggregation tendency, and properties. Such systems will also offer the perfect substrate for the development and optimization of novel analytical techniques suitable to study carbohydrate materials.

1.2. Carbohydrate materials

Carbohydrates comprise more than 80% of biomass, making them the most abundant class of biopolymers on earth. They are essential for energy storage and structural functions. More recently, the regulatory role

of carbohydrates in several biological processes has become evident.[17] Cell differentiation, proliferation and adhesion, inflammation and immune responses are connected to carbohydrate-carbohydrate (CCIs)[18] and carbohydrate-protein (CPIs)[19] interactions. These interactions are weak, often in the micro to millimolar range, so nature makes use of multiple weak interactions to circumvent this issue (multivalency). The concept of multivalency has been exploited by synthetic chemists in order to mimic nature.[20] Several nanostructures, coated with multiple copies of the same carbohydrate ligand, permitted to increase the CPI and CCI strength.[3c, 21] Enhanced water solubility and stability are also observed. Glycosylated scaffolds, such as polymers, nanoparticles, and surfaces, have been reviewed extensively as potential drug delivery systems, vaccines, and therapeutics.[3c, 22] In contrast, the tendency of carbohydrates to form supramolecular networks via a multitude of hydrogen bonds, is much less studied, but could guide the development of novel carbohydrate-based self-assembling systems. [3c]

1.2.1. Polysaccharides as materials

Natural polysaccharides, including cellulose[23] and chitin,[24] have a strong tendency to aggregate in well-defined architectures with different physical properties. Chemical modification tunes polysaccharide properties[25] to serve as biocompatible,[23c, 26] cheap, and renewable self-assembling materials for application in nanotechnology,[27] optics,[23b, 28] drug delivery,[29] and tissue engineering.[24a] Polysaccharides extracted from natural sources offer a valuable substrate for the formation of materials.[30] Their abundance, biocompatibility, and tendency to form stable supramolecular networks are extremely appealing features for the creation of nanomaterials, like nanoparticles or gels. Additionally, these polymers could be easily functionalized to improve solubility, stability, encapsulation and responsiveness.[25a, 31]

Cellulose is the most abundant biopolymer on earth and a major structural component in plants, algae, fungi, and bacteria.[32] D-glucopyranose monomers are connected through β-(1,4)-glycosidic linkages forming elementary fibrils (protofibrils). Cellulose microfibrils arise from a large number of inter- and intramolecular interactions of the protofibrils, ensuring high mechanical strength, durability, and water-insolubility. These features allow for the use of cellulose in the paper, textile, filter, and building material industry.[33] Recently, nanocellulose (NC) has gained attention as materials.[34] Three main classes of NC exist: cellulose nanocrystals (CNCs), nanofibrillated cellulose (NFC), and bacterial nanocellulose (BNC). NC can be extracted from various biosources and can be easily chemically or physically modified.[35] Like other nanomaterials, NC shows a high surface to volume ratio and improved solubility compared to natural cellulose. Indeed, the limited water solubility of cellulose is a critical obstacle for applications. For a better usage of cellulose, structural modifications have been introduced to decrease inter- and intramolecular hydrogen bonding.[36] The cellulose backbone, rich in hydroxyl groups, can be esterified and etherified. To overcome the poor solubility of cellulose in common solvents, ionic liquids, such as 1-*N*-butyl-3-methylimidazolium chloride (BmimCl) and 1-*N*-alkyl-3-methylimidazolium chloride (AmimCl), can be employed. Cellulose acetate (CA), ethylcellulose (EC), hydroxypropylcellulose (HPC), and carboxymethylcellulose (CMC) are the most common cellulose derivatives (**Figure 1-2B**), showing

improved water solubility. Hydrophobic segments, like poly(L-lactic acid), have been grafted onto the cellulose backbone to give rise to amphiphilic copolymers.[37]

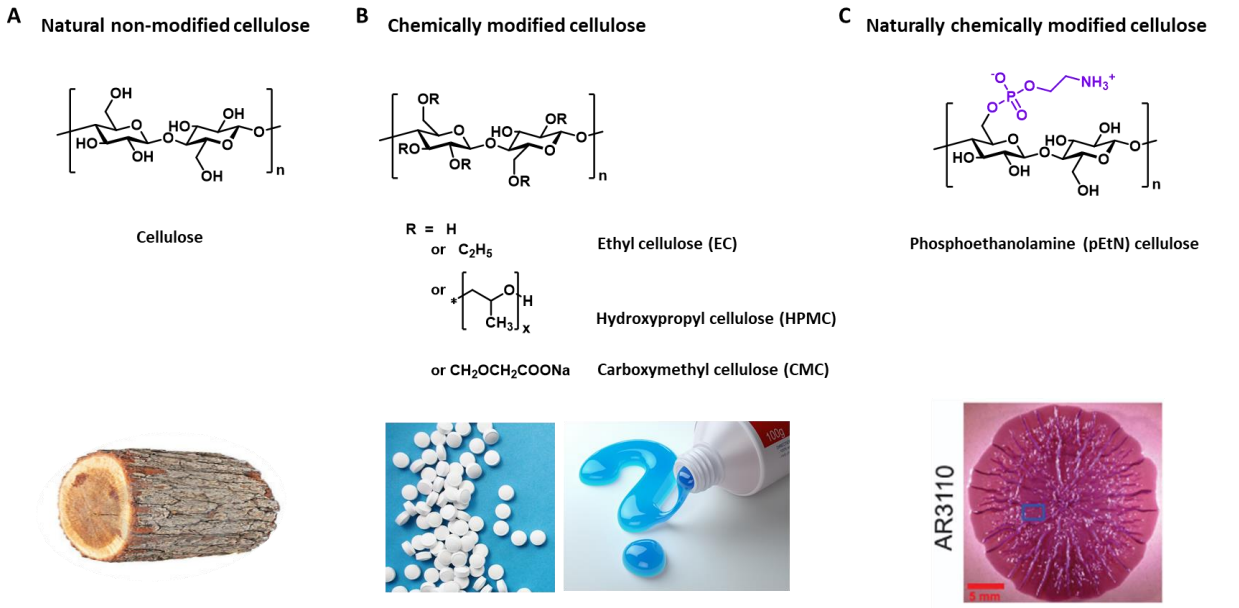

Figure 1-2. Chemical structure of cellulose and its most common derivatives (top) and images showing materials composed of natural non-modified cellulose (A), chemically modified celluloses (B), and naturally produced chemically modified cellulose (C). Adapted with permission from Thongsomboon et al.[38] Copyright (2018) AAAS.

Recently, the first example of naturally modified cellulose was reported (**Figure 1-2C**).[39] The phosphoethanolamine (pEtN) cellulose was discovered as part of the protective biofilms produced by certain bacteria, such as the uropathogenic *E. Coli* strain UTI89 and *Salmonella typhimurium*. Bacterial biofilms are nanocomposites of amyloidogenic proteins (i.e. curli fibers) and cellulose that surround bacterial colonies. It was demonstrated that the pEtN modification is essential to alter the biofilm morphology and to tune its mechanical properties, resulting in enhanced adhesion. Still, the molecular level interactions between the peptide and carbohydrate components in these biofilms remain unclear. A better understating of how these nanocomposites are formed could open up new possibilities to utilize bacterial biofilms as biological “factories” for the production of functional materials.[40]

Chitin, poly β-(1-4)-*N*-acetylglucosamine, is the second most abundant polysaccharide in nature, mainly constructing the exoskeleton of crustaceans, insects, and the fungal cell wall. Despite its superior biocompatibility, biodegradability, and physical stability, chitin has been rarely studied for biomedical applications due to its poor solubility in water. To overcome this drawback, chitin is treated with concentrated sodium hydroxide or chitin deacetylase to obtain chitosan, its partially deacetylated derivative (**Figure 1-3**). Chitosan is the most important derivative of chitin, generally with a degree of acetylation (DA) lower than 50%. The DA, distribution of amine and acetylamine groups, and molecular weight determines solubility and biological activity of chitosan.[41]

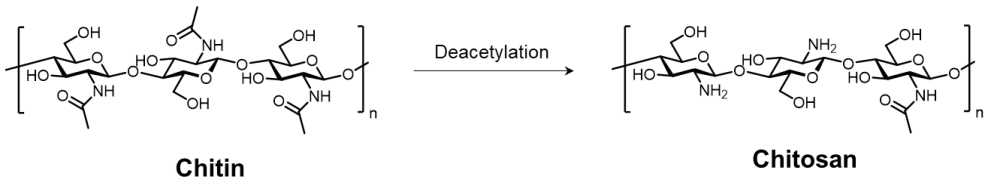

Figure 1-3. Chitin and its deacetylated analogue chitosan.

Similar to cellulose, chitin forms strong inter- and intramolecular hydrogen bonds, which hamper its use. In addition, chitin possesses a fibril structure that is not soluble in most organic solvents. Complex solvent mixtures, such as $CaCl_2 \cdot 2H_2O$ saturated methanol, lithium chloride/*N,N*-dimethylacetamide (LiCl/DMAc), NaOH/urea, hexafluoroisopropanol (HFIP), and ionic liquids are employed to disrupt the dense hydrogen bond network of chitin.[42] Ultrafine nanofibers can be obtained by simple solvent evaporation from HFIP solutions or from precipitation induced by addition of water to a LiCl/DMAc solution. These nanofibers are important materials for tissue engineering, as confirmed by *in vitro* cell cytotoxicity and cell proliferation assays.[43] Chitin in NaOH/urea rapidly aggregated into nanofibrous microspheres with high cellular affinity.[44]

These and other polysaccharides have been used extensively to generate materials with diverse applications. Still, most systems suffer from low reproducibility and programmability due to large variations in molecular weight, conformations, and substitution patterns of natural polysaccharides.[25a, 45] Synthetically prepared polysaccharides, with well-defined compositions, can offer an alternative to extracted natural polysaccharides and could be useful substrates to deliver information on the natural counterpart.

1.2.2. Mono- and oligosaccharides as materials

Mono- and oligosaccharides have been extensively modified to generate glycoamphiphiles able to assemble in diverse morphologies like micelles, vesicles, and fibers (**Figure 1-4**). Non-covalent interactions promote the formation of the assembly. Several examples of dissociation of the assembly in response to external stimuli, such as heat, light, and ultrasound, have been reported. This behavior is particularly important for drug delivery systems, where the responsive release can be exploited to minimize drug side effects. In addition, the amphiphilic nature of most sugar materials permits the encapsulation of both hydrophilic and hydrophobic molecules. Water-soluble compounds like enzymes, plasmid DNA, and genes as well as water-insoluble dyes can be delivered upon encapsulation into sugar micelles and vesicles (**Figure 1-4, top**).[46]

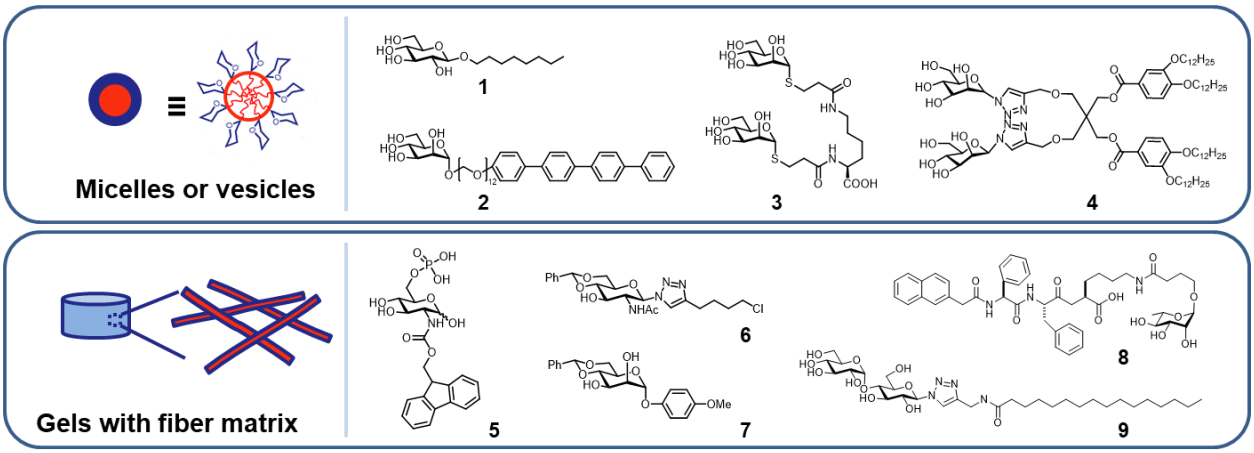

Figure 1-4. Supramolecular assemblies and chemical structures of monosaccharide amphiphiles. Adapted from Gim *el al*.[47]

Modified mono- and disaccharides have been used as low molecular weight gelators (LMWGs). Most sugar gelators are conjugated to hydrophobic moieties (**Figure 1-4, bottom**), such as aliphatic chains or aromatic groups.[48] These sugar-derived supramolecular structures can encapsulate hydrophobic drugs to increase drug solubility and serve as scaffolds for biomedical applications. Moreover, 3D gel matrixes from sugar gelators were exploited as tissue engineering scaffolds and for cell proliferation.[49]

Cyclodextrins are cyclic oligosaccharides constituted of glucopyranose units linked via a α-(1,4) glycosidic bond, commonly produced during the degradation of starch. The most common cyclodextrins are α-, β-, and γ types, consisting of six, seven, and eight glucose units. Because of their cavity, cyclodextrins can form unique inclusion complexes with specific molecules, and further assemble into supramolecular structures.[50] Hence, they are potential structural units to build nanomaterials.[3c, 51]

Supramolecular structures formed from mono- and oligosaccharides showed potential for biomedical applications, such as bacterial infection inhibition and bone regeneration.[47, 52] The majority of these systems require several modifications with bulky proteins or lipid units. Moreover, most studies were limited to the usage of mono- and disaccharides. The molecular level description of these carbohydrate assemblies is often missing, hampered by the lack of suitable analytical techniques. With the development of synthetic techniques that allow for the quick access to longer oligosaccharides, new glycomaterials, requiring less functionalization, can be envisioned.[53] Moreover, the development of new analytical techniques could improve the molecular characterization of these materials, producing information on key interactions that stabilize these assemblies.

1.3. Characterization of nanostructures

One of the biggest challenges in supramolecular chemistry is the characterization of the resulting assembly in its native environment. Structural analysis is crucial to identify non-covalent interactions promoting the

assembly. However, most available techniques are not suitable for the characterization of carbohydrate samples, due to their flexibility, lack of chromophores, and poor tendency to crystallize.

Here, I review the available methods commonly used for the study of nanomaterials and their applications to the study of carbohydrate materials.

1.3.1. Size and morphology analysis

The size and size distribution of nanomaterials can be determined via various scattering techniques or direct imaging of the nanostructures.

1.3.1.1. Scattering techniques

Dynamic light scattering (DLS) is the most popular and economical method for analyzing the size and size distribution of transparent dispersed systems. For liquid samples, the movement of particles under Brownian motion is detected as a fluctuation of the scattering signal (**Figure 1-5A**). The signal is quantified by frequency analysis or correlation spectroscopy and translated into the intensity-weighted hydrodynamic radius (d(*H*)) using the *Stokes-Einstein* equation (**Figure 1-5B**).[54]

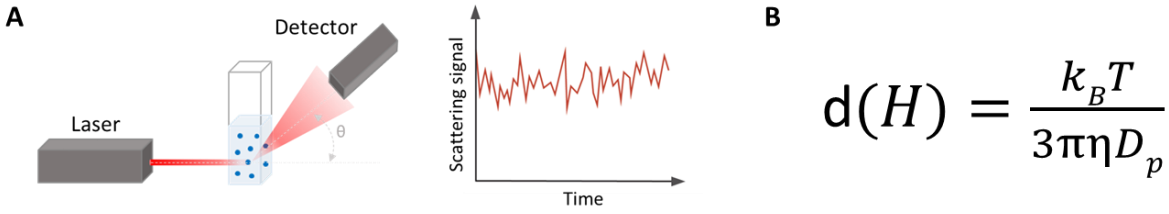

Figure 1-5. (A) Schematic representation of the principle of DLS. (B) The hydrodynamic radius (d(*H*)) derived from *Stokes-Einstein* equation; where k_B is the Boltzmann's constant, *T* is temperature, *η* is the dynamic viscosity of the fluid, and *Dp* is the particle diffusion coefficient.

For comparison with the microscopic observation, the intensity-weighted radius, proportional to r^6 where *r* is the radius of the particle, can be converted into the number-weighted radius, proportional to *r*, causing amplification of noise or artefacts. False measurements due to multiple scattering effects could generate significant errors in light scattering experiments.

Small angle scattering can be complementary to the light scattering technique. Neutron and X-ray scattering provide information on detailed structure and size of small-scale objects due to the small wavelength of the probing radiation. Small angle X-ray scattering (SAXS), scattered by monochromatic X-rays, and small angle neutron scattering (SANS), scattered by neutrons, offer higher resolution, for example 0.154 nm for Cu-K_α radiation and 0.5 nm for thermal neutrons. The methods are accurate and mostly non-destructive, however, beam sensitive organic materials can be damaged by irradiation.

1.3.1.2. Microscopy techniques

Imaging with different kinds of microscopy provides the physical size of solid samples. Electron microscopy (EM) enables higher resolution than optical microscopy by using an electron source and electromagnetic lenses under vacuum. Here some classical microscopy methods are exemplified for the visualization of CNCs (**Figure 1-6**).

In transmission electron microscopy (TEM), the incident electron beam passes through a thin specimen and generates 2D projected images. The sample is distinguished from the background due to interactions with incident electrons. The thicker or higher mass region appears darker on a bright-field image due to electron absorption or scattering (**Figure 1-6A**). Crystalline samples additionally provide diffraction contrast based on Bragg's scattering. Imaging of biomolecules highly depends on mass-thickness contrast, yet a negative staining with heavy metals (e.g. uranyl acetate), is often required for sharp contrast and protection of the samples from the strong electron beam (**Figure 1-6B**). A better way to study biological samples in their native state is Cryo-EM (**Figure 1-6C**). The specimens prepared in vitreous ice allow imaging of individual molecules and macromolecular assemblies. By combining a tilt-series of 2D images, a 3D image is computationally reconstructed, termed electron tomography (**Figure 1-6D**).

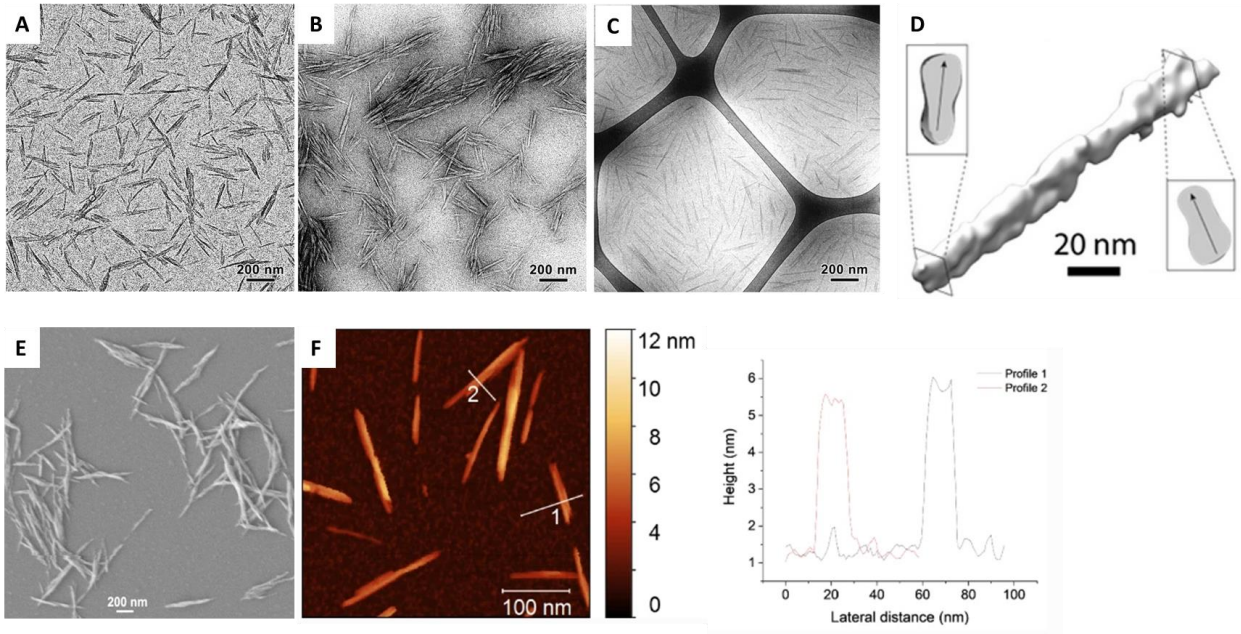

Figure 1-6. Microscopy analysis of cellulose nanocrystals (CNC). Conventional TEM images without staining (A) and with negative staining (B). A Cryo-TEM image (C) and electron tomography (D). A SEM image (E) and an AFM image (F) with cross-sectional z-dimension analysis. Adapted with permission from Kaushik *et al*.[55] Copyright (2015) for A,B, and C, Majoinen *et al.*[56] Copyright (2014) American Chemical Society for D, Anzlovar *et al.*[57] Copyright (2020) Springer Nature for E, and Chen et al.[58] Copyright (2021) Springer Nature for F.

Scanning electron microscopy (SEM) produces images by scanning the surface with a focused electron beam (**Figure 1-6E**). SEM collects the signal responsible for the secondary electrons (SEs) and/or backscattered electrons (BSE). SEs are emitted from inelastic collisions with electrons in the k-orbital of the samples providing superior topographic contrast, while a BSE mode with elastically scattered electrons is useful for compositional contrast. Organic compounds require coating with electronically conductive materials such as gold and palladium. Cryo-SEM and environmental SEM (ESEM) offer alternatives to avoid artefacts generated during the drying process.

Atomic force microscopy (AFM) is a type of scanning probe microscopy (SPM) with a very high vertical resolution at 0.1 nm (**Figure 1-6F**). A small physical probe interacts with the sample surface generating 3D topographic images and force-distance curves. A small tip with different size and shape is attached at the end of a cantilever characterized by a spring constant *k*. The deflection of the cantilever is monitored as piezoelectric displacement. AFM is widely used for different types of samples, conductive or non-conductive, without post-treatment under various environments such as air, vacuum, and liquid.

1.3.2. Structure analysis

The structural transition of a molecule can be monitored via fourier-transform infrared (FTIR) spectroscopy and circular dichroism (CD). These methods are simple and quick to gain insights on structural rearrangements.

FTIR detects functional groups within organic compounds using absorption or emission of an infrared radiation. As the frequency of the absorbed (or emitted) IR radiation is affected by the environment, this technique is used to investigate the formation of aggregates and molecular folding/binding.

CD measures the different absorption of left- and right-handed light. It is widely employed to investigate secondary structure transitions of peptides and nucleic acids in the far-UV region. Since most carbohydrates lack a chromophore portion absorbing in the far-UV region, CD was implemented in the short-wavelength region below 200 nm using a vacuum ultraviolet (VUV) spectroscopy.[59] The intrinsic difficulty in CD measurement of carbohydrates was partially overcome with specific interactions between chiral carbohydrates and dye molecules (**Figure 1-7**).[60] Complexation with aromatic dyes such as Congo red and/or substitution with aromatic moieties enabled the detection of helicity of carbohydrates in the far-UV or visible light region.[61]

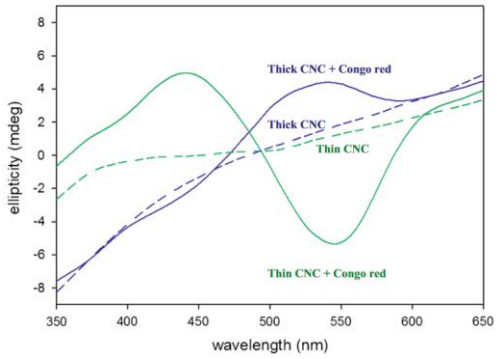

Figure 1-7. Circular dichrodism spectra of isotropic CNCs with (solid line) and without (dotted line) Congo red. Adapted with permission from Conley et al.[61] Copyright (2017).

Structural information with atomic resolution can be obtained with nuclear magnetic resonance (NMR) spectroscopy and diffraction techniques. Molecular orientation and dynamics can be studied via two-dimensional correlation spectroscopy or comparison between liquid- and solid-state NMR spectra. However, the use of NMR is often limited due to the polydispersity of extracted carbohydrates and the quantity of samples that can be produced synthetically. The introduction of NMR active nuclei like ^{13}C or ^{19}F permits to increase NMR sensitivity and to simplify NMR spectra suffering from severe signal overlapping.[62]

X-ray crystallography provides the unit-cell and space group of a crystalline sample. Powder X-ray diffraction (XRD) offers the separation distance d, by changing the incidence angle θ, between 0 and 90 degrees in accordance with Bragg's law. The peak position, intensity, and broadness determine the crystal size, crystallinity, and polydispersity, respectively. As a bulk technique, the orientation of crystals highly alter relative intensities depending on their preferred orientation.[63] The crystallographic database for monosaccharides is rich. However, the number of data drops drastically as the chain elongates, with only few crystal structures available for linear and cyclic oligosaccharides. Moreover, the lack of reference XRD patterns for carbohydrates hampers structure prediction and analysis, requiring complementary experimental methods.

Microcrystal electron diffraction (MicroED) was developed in 2013, and permitted to unveil the 3D structure of pathologically important proteins with a resolution of few angstroms.[64] Diffraction patterns from a small selected scan area (few hundreds nm scale) are obtained with a Cryo-TEM in diffraction mode. Through continuous rotation of sample holders with a specific increment angle between frames, three-dimensional data are collected (up to 140 degrees). MicroED became extremely popular for structural determination since it directly reveals the molecular organization of the self-assembled structure in its native state, reducing tedious crystallization trials that can alter the supramolecular organization. MicroED could offer a suitable alternative to X-ray crystallography to solve the structure of carbohydrate crystals, enabling rapid and less destructive analysis with smaller quantities of samples and much smaller crystals due to the

stronger interaction of electrons with the sample. Still, to date, MicroED is rarely employed to study oligosaccharides due to their sensitivity to the electron beam.[64]

1.3.3. Mechanical property analysis

In addition to imaging, AFM allows for electrochemical and mechanical property analysis. Stiffness and adhesion can be easily measured in bulk systems. Additionally, measurements of nanoscale contact and single molecular interactions in the pN scale can be performed. The force between the tip and surface is described by the Lennard-Jones potential. When the AFM probe is far from the surface, the photodiode sensor deflection (PSD) shows no interaction (baseline signal). The cantilever starts to be deflected from a contact point. After reaching the maximum load point, the tip is retracted. The signal is recorded as a PSD-scanner displacement curve and transformed into a force-distance curve (F-D curve) (**Figure 1-8**). After the calibration of the cantilever spring constant and sensitivity, the approach curve offers the stiffness and the indentation distance. From the retraction curve, the adhesion force and energy dissipation can be obtained.

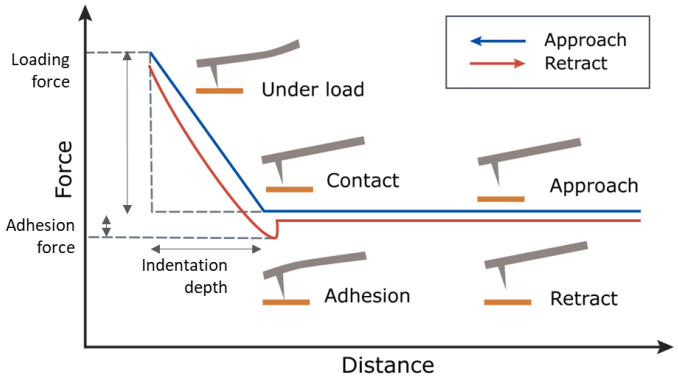

Figure 1-8. Illustration of AFM force spectroscopy. Force versus distance curve after calibration and conversion. The retraction part of the curve is shifted for illustration.

1.4. Aims of this thesis

The general aim of this thesis was to generate supramolecular carbohydrate materials as models to elucidate the rules that govern carbohydrate-carbohydrate and carbohydrate-peptide interactions.

More in detail, the first aim of the thesis was to study supramolecular assemblies of well-defined synthetic oligosaccharides to establish structure-property correlations and understand the interactions that trigger supramolecular aggregation. For these purposes:

i. A set of oligosaccharides needs to be designed and systematically studied.
ii. Proper sample preparation methods should be chosen and optimized to trigger the formation of supramolecular carbohydrate assemblies.

iii. Supramolecular structures need to be analyzed with different analytical techniques to elucidate which interactions are responsible for the assembly.
iv. New analytical methods need to be implemented to the study of carbohydrate materials.
v. Physical and mechanical properties need to be evaluated and correlated to the assembly structure to establish definitive structure-property correlations.

The second aim of this thesis was to understand the role of carbohydrates in the formation of composite materials with other biomolecules (i.e. peptides). Bacterial biofilm, a nanocomposite of polysaccharides and proteins, was selected as a model system to understand its formation and the interactions taking place between the individual components. To this end:

i. Representative sequences of amyloidogenic peptides and carbohydrates present in bacteria biofilms need to be selected.
ii. An assay to generate and analyze artificial biofilm models needs to be developed.
iii. The artificial biofilm needs to be prepared in the presence of different oligosaccharides and the results analyzed.
iv. The mechanical properties of the artificial biofilms need to be measured and correlated to the chemical structure of the oligosaccharide components.

2. Oligosaccharides self-assemble and show intrinsic optical properties

This chapter has been modified in part from the following article:

Y. Yu,* **S. Gim**,* D. Kim, Z. A. Arnon, E. Gazit, P. H. Seeberger, M. Delbianco, Oligosaccharides Self-Assemble and Show Intrinsic Optical Properties. *J. Am. Chem. Soc.* **2019**, 141(12), 4833-4838.

‡Equal contribution

2.1. Introduction

Carbohydrate-based materials have gained attention as a substrate for biomaterial applications due to their biological relevance and tendency to form supramolecular networks. However, the use of polysaccharide materials is limited by poor quality control and reproducibility, owing to the polydispersity of chain length and modifications. Short and well-defined oligosaccharides prepared by chemical synthesis can serve as an alternative to natural polysaccharides. Nevertheless, manual synthesis of oligosaccharides is time-consuming and requires special expertise. Automated Glycan Assembly (AGA) enables rapid access to oligo- and polysaccharides,[65] as long as 151-mer,[66] starting from simple and often commercially available building blocks. Such synthetic oligomers could offer a new avenue to generate materials with defined chemical compositions, overcoming the problems of reproducibility of extracted polysaccharides.

Synthetically prepared oligosaccharides that aggregate into defined nano- and microstructures offer a platform to study carbohydrate materials and identify key inter- and intramolecular interactions responsible for the formation of a material. Like the aggregation of nucleic acids and peptides is highly dependent on their chemical structures and molecular organizations,[67] the structural diversities in carbohydrates, such as length and substitution, are expected to divert their supramolecular assemblies.

It has been reported that several intermediates formed during cellulose deprotection are causing aggregation.[68] Similarly, we faced solubility issues during the deprotection of compound **10** (**Figure 2-1A**).[69] This semi-protected hexasaccharide showed poor solubility in most organic solvents, preventing the formation of the target fully deprotected oligosaccharide, **11**. A TEM measurement of a solution of **10** revealed the formation of nano-aggregates in solution, likely hampering the chemical reaction (**Figure 2-1B**). We hypothesized that aggregation was stabilized by intermolecular hydrogen bonding between the numerous hydroxyl groups and π-π interactions between benzyl ether modifications. Inspired by compound **10**, six oligosaccharides with different length, glycosidic linkage, and protective patterns were systematically designed and synthesized to explore their self-assembly behavior (**Figure 2-2A**). The syntheses were performed by Dr. Y. Yu. The self-assembly behavior was observed with different microscopic techniques such as TEM, SEM, and AFM. The photophysical properties were examined with UV-Vis and fluorescence spectroscopy and confocal microscopy.

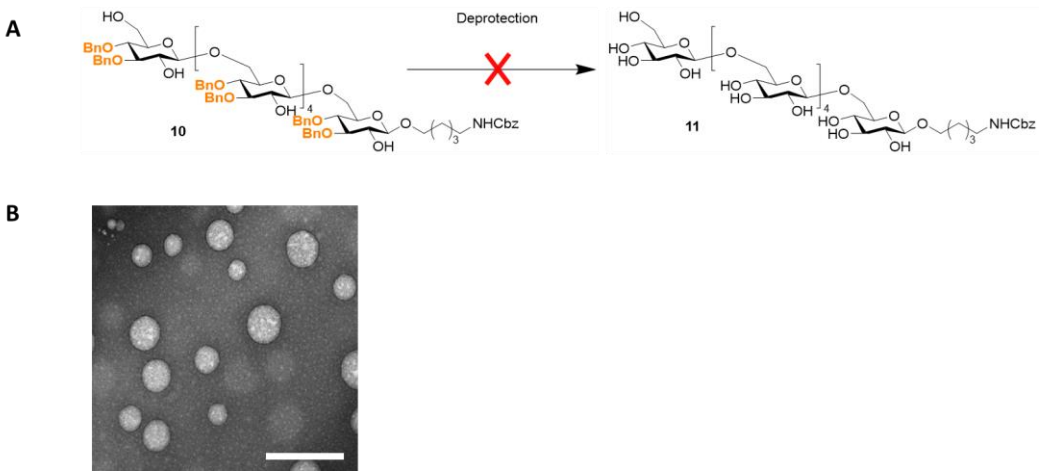

Figure 2-1. (A) Attempted debenzylation of **10**. (B) TEM image of nanoparticles formed by **10** in water (scale bar: 1 µm).

2.2. Results

2.2.1. Self-assembly methods

Three different methods (*e.g.* dialysis (**D**), solvent-switch (**S**), and film forming (**F**)) were selected to trigger the formation of supramolecular structures (**Figure 2-2B**). For each method a careful screening of conditions, including solvents and concentration, was performed. Five solvents (*e.g.* hexafluoroisopropanol (**HFIP**), dimethylacetamide (**DMAc**), acetone (**Ace**), isopropanol (***i*PrOH**), and water were explored.

The sample names indicate the sugar oligomer (*e.g.* **13**) and the assembly method (*e.g.* **D**, **S**, or **F**). For example, **13**(**S**) means compound **13** prepared by solvent switch method (**S**). When not mentioned, the standard concentration is 0.1 mg mL^{-1} and 2.0 mg mL^{-1} for dialysis method and solvent switch method, respectively. DMAc was employed as standard for the dialysis method (**D**) and HFIP was used as standard for the solvent-switch (**S**) and film forming method (**F**). Deviations from the standard condition including a different solvent (e.g. **Ace**), sample concentration (*e.g.* **low** or **high**), or the content of organic solvent (*e.g.* **20%**) are appended to the sample name. Details of sample preparation are described in the experimental section, **2.4.2**.

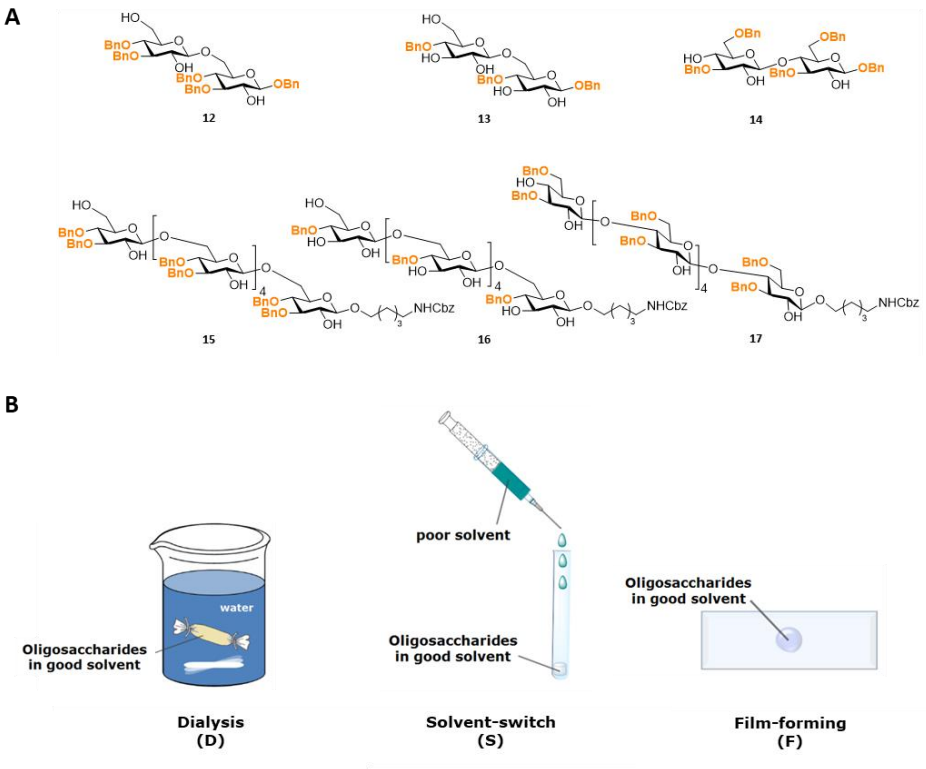

Figure 2-2. (A) Chemical structures of synthetic oligosaccharides analyzed in this study. (B) Cartoon representation of sample preparation methods used to trigger the formation of supramolecular assemblies.

2.2.2. Screening of oligosaccharide self-assembly

2.2.2.1. Dialysis method

For the dialysis method, DMAc was selected as a good solvent due to its ability to dissolve partially benzylated oligosaccharides. All six oligosaccharides dissolved in a DMAc/water mixture and dialyzed against water aggregated into spherical nanoparticles with diameters of 40-60 nm (**Figure 2-3**). These particles existed in solution as confirmed by Cryo-SEM of **13(D)** (**Figure 2-4**) and DLS measurements (**Figure 2-3**).

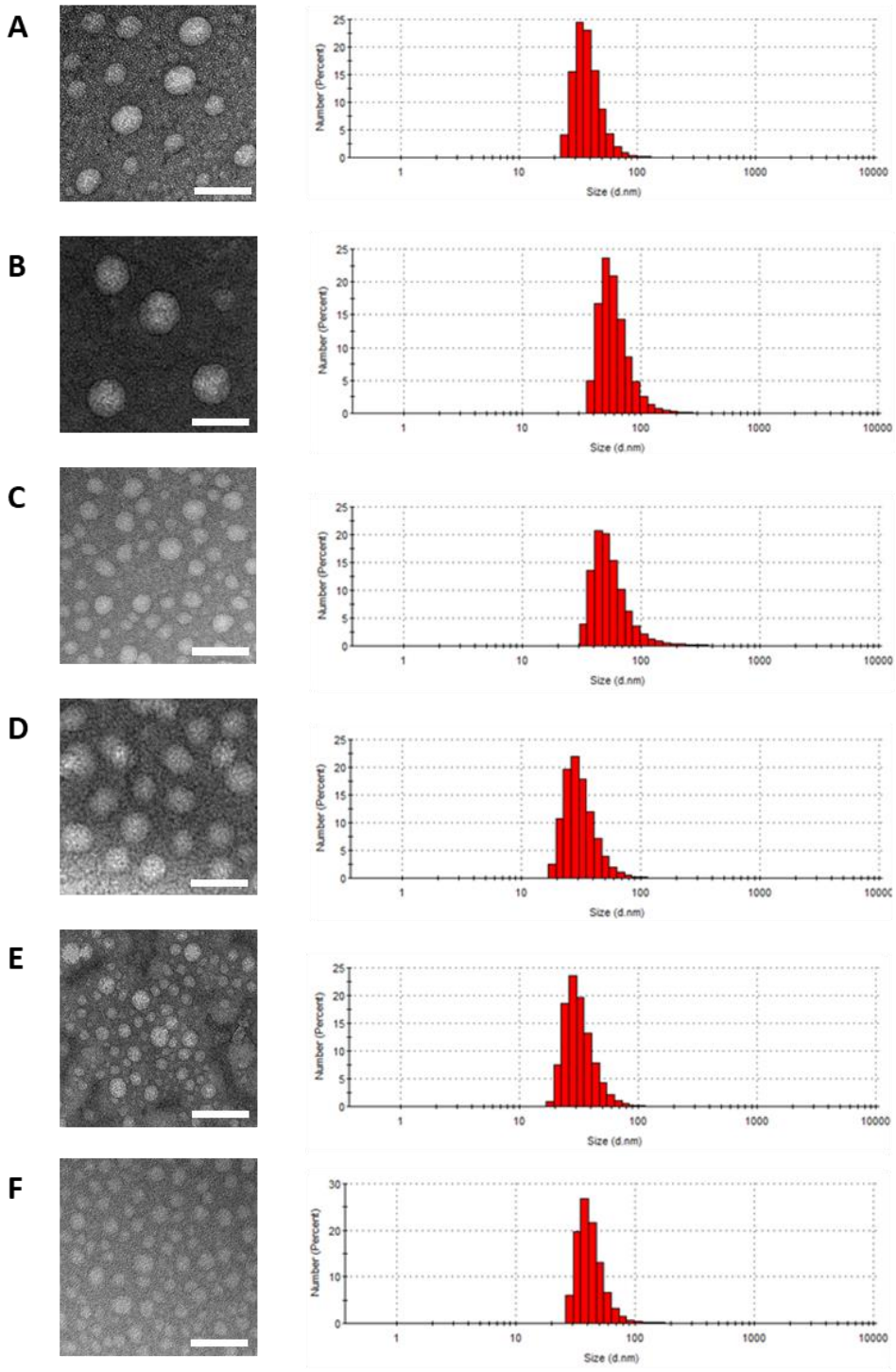

Figure 2-3. TEM images (left, scale bars: 100 nm) and DLS analysis (right) of samples prepared by dialysis method. (A) **12(D)**, (B) **13(D)**, (C) **14(D)**, (D) **15(D)***, (E) **16(D)**, and (F) **17(D)***. If not mentioned, the standard concentration is 0.1 mg mL^{-1}. *0.01 mg mL^{-1} due to poor solubility of starting material.

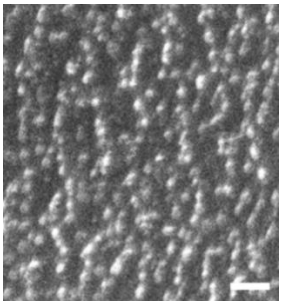

Figure 2-4. Cryo-SEM image of **13(D)** confirming the presence of the particle in solution (scale bar: 200 nm).

2.2.2.2. Solvent-switch method

Direct injection of water into a glycan solution in HFIP (i.e. solvent switch method) resulted in faster mixing, higher oligosaccharide concentration and altered self-assembly behavior (**Figure 2-5**). Needle-like structures were found for **13(S)** (5-10 µm length, 10-50 nm height and 100-500 nm width, **Figure 2-5B** and **2-6**) and a spheroidal architecture (1-2 µm diameter) for the hexamer analogue, **16** (**Figure 2-5E**). **12(S)** assembled into a mixture of rods and toroid structures (**Figure 2-5A**), while **15(S)** formed clusters of nanoparticles (**Figure 2-5D**). Differences in oligosaccharide structure such as linkage positions and modification patterns fundamentally affected the material morphology, as **14(S)** (**Figure 2-5C**) and **17(S-DMAc)** (**Figure 2-5F**) aggregated randomly and did not form any ordered supramolecular structure. Compounds **14** and **17** are based on a fairly rigid β(1,4)-glycosydic linkage (secondary alcohol) and therefore can adopt a limited number of conformations in solution. The flexibility of the β(1,6)-linkage allows for higher conformational diversity,[70] permitting the formation of fundamentally different nanostructures.

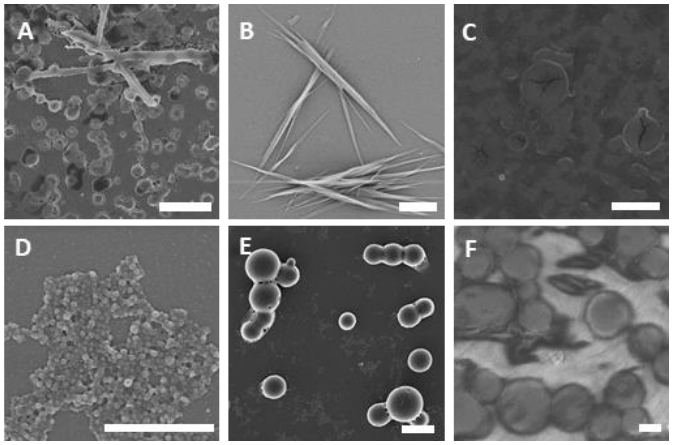

Figure 2-5. SEM images of samples prepared by the solvent-switch method. (A) **12(S-low)***, (B) **13(S)**, (C) **14(S)**, (D) **15(S-DMAc)**, (E) **16(S)**, and (F) **17(S-DMAc)** (scale bar: 2 µm). If not mentioned, the standard concentration for solvent switch method (**S**) is 2 mg mL-1. *0.1 mg mL-1 due to poor solubility of starting material.

2.2.3. A closer look at compound 13

The needle-like supramolecular structure formed by compound **13** was stable for one month at ambient conditions and resisted dilution and sonication (**Figure 2-6**). **13(S)** presents an ordered morphology as it showed intense birefringence under polarized light, typical of anisotropic materials (**Figure 2-7A**). Moreover, staining with Congo red,[71] a commonly-used dye to detect amyloid fibrils, gave intense gold-green birefringence (**Figure 2-7B**), supporting the highly-ordered morphology of the assembly.

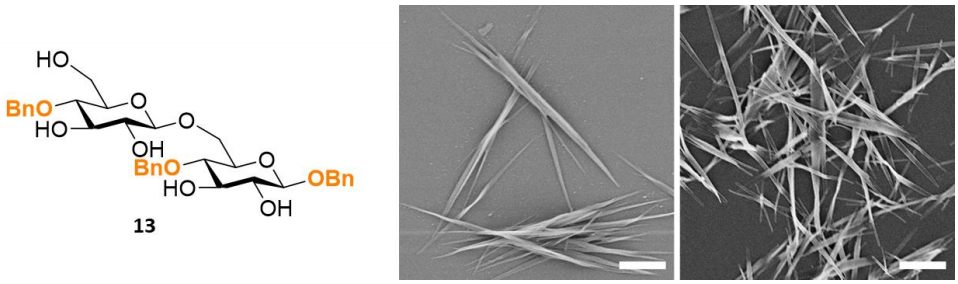

Figure 2-6. SEM images of **13(S)** at time 0 (left) and after one month upon dilution (right) (scale bars: 2 µm).

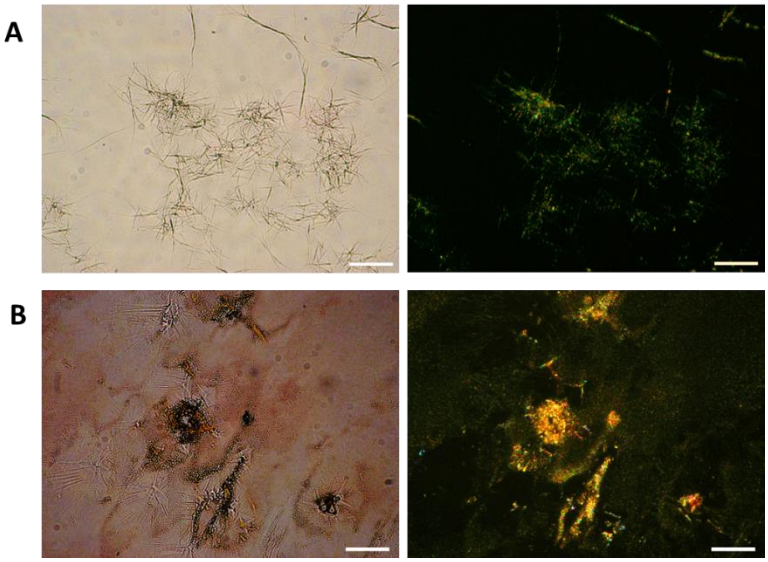

Figure 2-7. (A) Polarized microscopy images of **13(S)** with parallel (left) and crossed polarizer (right). (B) Congo red birefringence assay of **13(S)** with parallel (left) and crossed polarizer (right) (scale bars: 20 µm).

Dialysis using a higher concentration of **13** (2 mg mL^{-1}) led to the formation of nanofibers (**Figure 2-8A**), likely due to the further association of the spherical particles existing in the diluted solution. The solvent switch method generated longer needles when a lower concentration of compound **13** was employed (0.1 mg mL^{-1}) (**Figure 2-8B**). A higher HFIP content (20%) did not change the geometry of the supramolecular structures (**Figure 2-8C**). In this case, the selective solvation properties of HFIP, in a HFIP–H_2O system,[72] resulted in a similar local HFIP concentration, limiting aggregation diversity. A similar elongated morphology

was obtained when isopropyl alcohol was used instead of HFIP (**Figure 2-8D**) and a gel-like microwire material was obtained in acetone (**Figure 2-8F**). The diversity observed was ascribed to the different conformations adopted by **13**, when solvated by different solvents. In particular, the well-known ability of HFIP to cluster the hydrophobic regions of peptides and affect their folding (HFIP-induced enhancement of the hydrophobic effect)[72-73] could be responsible for the dramatic differences of the generated nanostructures.

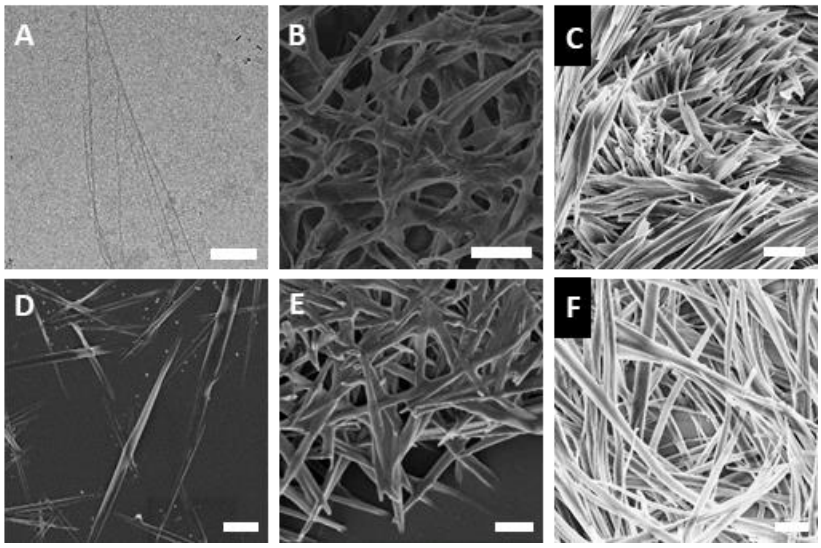

Figure 2-8. Screening of assembly conditions for the assembly of **13**. (A) TEM image (scale bar: 500 nm) for **13(D-high)** (2 mg mL^{-1}). (B-F) SEM images (scale bars: 2 µm) for (B) **13(S-low)** (0.1 mg mL^{-1}), (C) **13(S-20%)**, (D) **13(S-*i*PrOH-20%)**, (E) **13(S-DMAc)**, and (F**) 13(S-Ace-20%)**. If not mentioned, the standard concentration for solvent switch method (S) is 2 mg mL^{-1} and the content of organic solvent is 2%.

The self-assembly of **13(S)** was captured in real-time using bright-field microscopy by injecting a freshly-prepared solution into a cell counting slide (**Figure 2-9**). Needle-like structures diffuse from the HFIP droplets containing the oligosaccharide into the surrounding water. The contact between the needles and a second HFIP droplet (**Figure 2-9**, time 06:52) disrupts the droplet to release the oligosaccharide and results in further needle growth. Surprisingly, glycan-containing HFIP droplets are intensely fluorescent. This phenomenon could be the result of the formation of supramolecular chromophores within the material, as previously observed for self-assembled peptides, nucleic acids, and amino acids.[74] The presence of aromatic residues, multiple bond conjugation, and/or charge delocalization through a dense hydrogen-bonding network are generally responsible for this behavior.[74c]

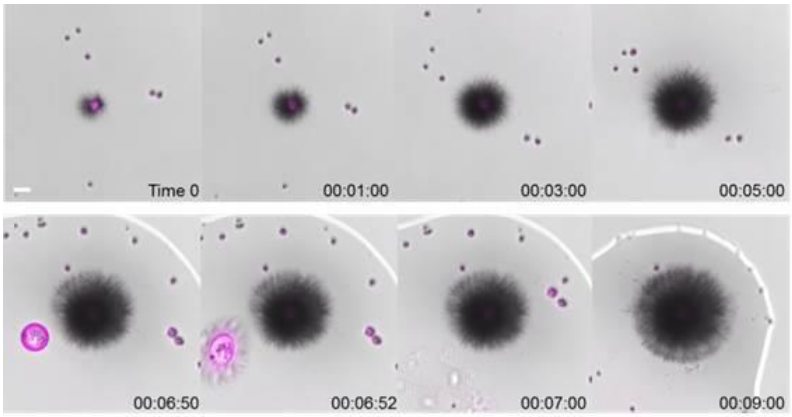

Figure 2-9. Real-time merged bright-field (scale of gray) and fluorescence (magenta) images illustrate the self-assembly process for **13(S)**. Excitation wavelength at 405 nm and detection range 410-676 nm (scale bar: 20 µm).

2.2.4. Fluorescence studies

During the assembling process, I noticed that the sugar-containing droplet showed some residual fluorescence, whereas the fibrils showed negligible emission (**Figure 2-9**). In order to better understand this unusual optical behavior, different assemblies of compound **13** were prepared. Two different methods, film-forming (**F**) and solvent-switch (**S**), were examined. Confocal microscopy analysis of the resulting morphologies revealed that thin films prepared by direct evaporation of a glycan solution in HFIP on a glass slide (**13(F)**) emit strongly in four different channels (**Figure 2-10A**) upon visible light irradiation. In contrast, aggregates obtained *via* the solvent switch method are only weakly emissive (**Figure 2-10B**). This observation agrees with the supramolecular chromophore hypothesis,[75] since emission intensity is strong in organic solvents, where a dense H-bonding network is favored, and quenching occurs when the H-bonding pattern is disrupted by water. The morphology of these materials was further probed with XRD (**Figure 2-10,** right). **13(S)** exhibited sharp peaks, as typical for crystalline structures; in contrast, **13(F)** showed broad peaks indicating amorphous aggregation. This confirmed the drastic change in morphology upon interaction with water (**13(S)**). The film obtained from the other five compounds showed similar optical properties (**Figure 2-11**).

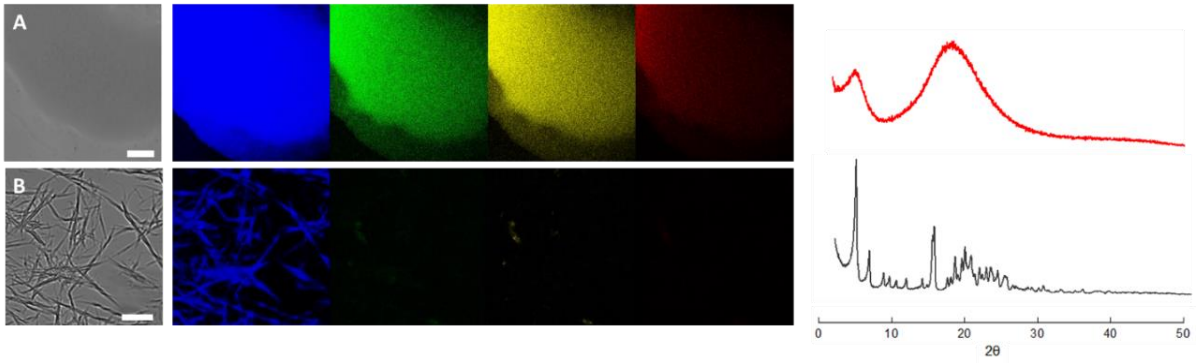

Figure 2-10. Confocal microscopy images (left) of **13** prepared by HFIP film-forming **F** (A, scale bars: 100 µm), solvent-switch **S** (B, scale bars: 10 µm) in four different channels (blue(ex/em): 405/451 nm, green: 488/529 nm, yellow: 561/597 nm, and red: 633/709 nm) and XRD profiles (right) of **13(F)** (red) and **13(S)** (black).

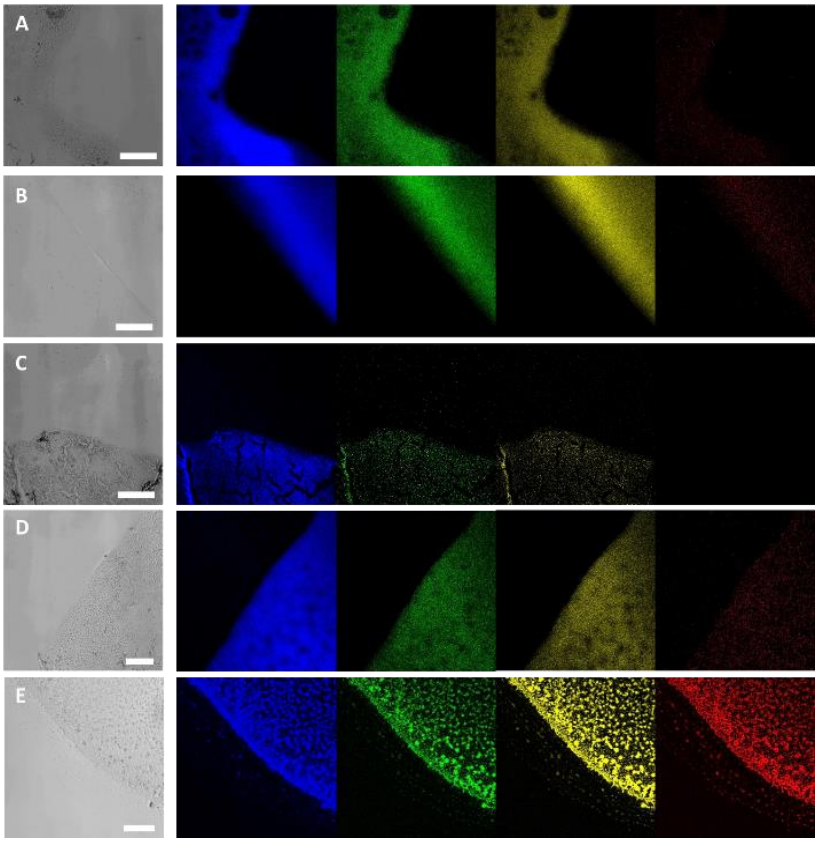

Figure 2-11. Confocal microscopy images of (A) **12(F)**, (B) **14(F)**, (C) **15(F)**, (D) **16(F)**, and (E) **17(F)** in four different channels (blue(ex/em): 405/451 nm, green: 488/529 nm, yellow: 561/597 nm, and red: 633/709 nm). (scale bars: 100 µm)

To identify the origin of this phenomenon, compounds **18**-**22** were prepared (**Figure 2-12**). Compound **18** was synthesized to probe the importance of aromatic groups for the emissive behavior. This amphiphilic, partially methylated analogue allows for the formation of a dense hydrogen bonding network, in the absence of aromatic groups. Upon film formation, **18(F)** showed a similar optical behavior, confirming that the optical properties are not merely a result of π-π stacking. Compounds **19-21** are fully functionalized, blocking the formation of a dense hydrogen bonding network within the material. Different substituents (Bn *vs* Me *vs* Ac) were tested. Surprisingly, confocal microscopy analysis showed emissive behavior for **19(F)** and **20(F)**. I suspect that such compounds, even in the absence of a strong hydrogen bonding network, maintain a self-organization tendency. On the other hand, the films obtained from the per-acetylated analogue **21**, as well as from the fully deprotected compound **22**, showed no emission. XRD analysis of all the materials suggested a correlation between the broad XRD profile and the emissive behavior. Similarly, the appearance of sharp peaks in the XRD profiles, indicating high crystallinity, is associated with emission quenching.

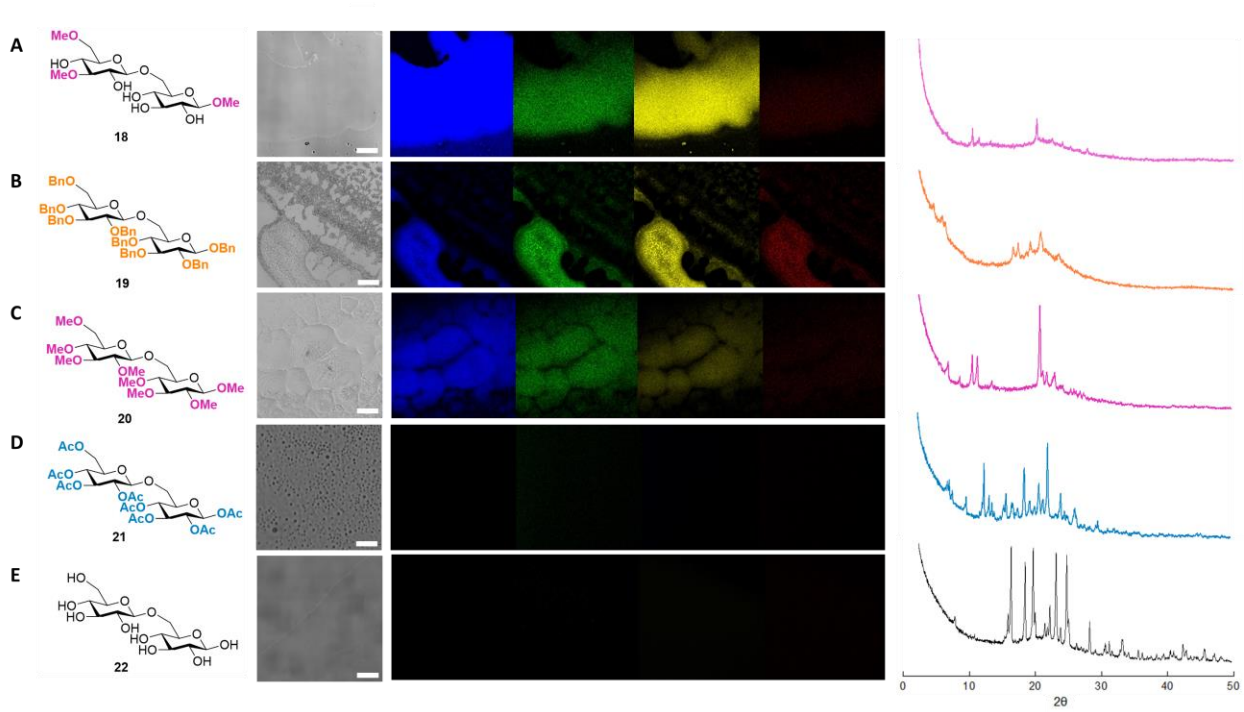

Figure 2-12. Chemical structures (left), confocal microscopy images (center), and XRD profiles (right) of (A) **18(F)**, (B) **19(F)**, (C) **20(F)**, (D) **21(F)**, and (E) **22 (F-water)**. Confocal microscopy was measured in four different channels (blue(ex/em): 405/451 nm, green: 488/529 nm, yellow: 561/597 nm, and red: 633/709 nm) (scale bars: 100 µm).

Further photophysical characterization showed a broad absorption band for compound **13(F),** associated with the formation of new self-assembled entities upon film formation (**Figure 2-13**). The broadening of the absorption spectrum is not observed for compound **13** in solution, nor for the low emissive, crystalline

sample **13(S)** (**Figure 2-13A**)**.** Excitation spectra (**Figure 2-13B**) confirmed that the emissive species are linked to this spectral region (350 – 500 nm). The emission quantum yield was calculated for **13(F)** ($\Phi_{(\lambda ex = 360\ nm)}$ = 0.85 ± 0.01 %). Unlike commonly-used dyes, where the emission peak position is independent of the excitation wavelength, the emission spectrum of **13(F)** is drastically affected by the excitation wavelength (**Figure 2-13C**). A broad fluorescence emission profile was observed with maxima shifting from 410 to 490 nm as the excitation was changed from 340 to 410 nm. This red edge excitation shift (REES) is a common phenomenon observed in graphene oxide,[74d] ionic liquids,[74e] and highly ordered assemblies,[74a] suggesting potential applications of self-assembling oligosaccharides for optical devices, semiconductors, and nanotechnology.[8d, 74a-c]

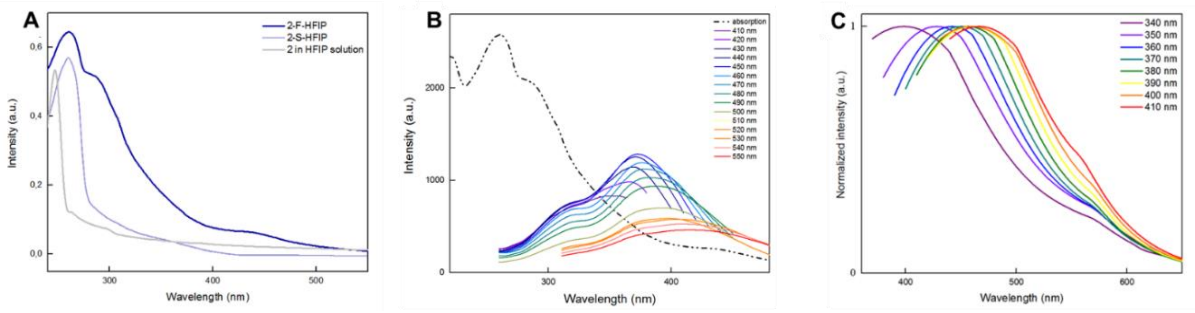

Figure 2-13. (A) Absorption spectra of **13(F)**, **13(S)** (recorded for the solid samples)**,** and compound **13** in HFIP solution. (B) Excitation spectra of **13(F)** at emission wavelengths between 410 and 550 nm at intervals of 10 nm. The black dotted line is the absorption spectrum. (C) Normalized emission spectra of **13(F)** at excitation wavelengths of 340, 350, 360, 370, 380, 390, 400, 410, 420, and 430 nm, showing the red shifting of the emission maxima. Spectra acquired at RT.

2.3. Conclusion

In conclusion, I successfully generated supramolecular structures from synthetic well-defined oligosaccharides, and demonstrated that fine-tuning of the oligosaccharide structure has a tremendous effect on the material morphology. The six disaccharide and hexasaccharide analogues with different glycosidic linkages and protective group patterns form similar nanospheres when the assembly is performed by the slow dialysis method, whereas distinctive microstructures are obtained upon fast solvent switch method. These compounds show unique optical properties, such as broad emission profiles and red edge excitation shift. Further studies to modulate the fluorescent properties of such materials are currently underway, with potential applications for optical devices and nanotechnology. These findings suggest that synthetic oligosaccharides are viable substrates for the fundamental study of the forces that guide the polysaccharide aggregation in nature. For example, tuning glycomaterial properties through the synthesis of well-defined structures will be relevant for drug delivery systems, where carbohydrate-carbohydrate interactions play a significant role in cellular uptake.

2.4. Experimental section

2.4.1. Synthetic methods

The synthesis was performed by Dr. Y. Yang. The detailed methods can be found in the published work.[76]

2.4.2. Oligosaccharide self-assembly

a) Dialysis method (D): The oligosaccharide was dissolved in 1 mL of DMAc and sonicated for 10 min. The mixture was diluted with 1 mL of ultrapure water in order to avert the dissolution of the dialysis tube and sonicated for an additional 10 min. The final solutions with concentration of 0.01, 0.1 and 2 mg mL^{-1} were prepared by extensive dialysis (3 days) with 500 Da and 1 kDa dialysis tubes, for dimers and hexamers, respectively. If not mentioned, the standard concentration for the dialysis method (**D**) is 0.1 mg mL^{-1}. Lower concentration, 0.01 mg mL^{-1}, was employed for compounds **15** and **17** due to poor solubility of the starting material.

Table 2-1. Summary of the samples prepared by the dialysis method (**D**).

Sample	Compound	Preparation method	Organic Solvent	Concentration (mg mL^{-1})
12(D)	12	Dialysis	DMAc	0.1
13(D)	13			0.1
13(D-high)				2.0
14(D)	14			0.1
15(D)	15			0.01*
16(D)	16			0.1
17(D)	17			0.01*

*0.01 mg mL^{-1} due to poor solubility of the starting material in DMAc.

b) Solvent-switch method (S): Stock solutions of the oligosaccharide (5, 10 and 100 mg mL^{-1}) in HFIP, isopropyl alcohol, acetone and DMAc were prepared. Ultrapure water was added to give a final concentration of 0.1, 2 and 20 mg mL^{-1}. If not mentioned, the standard solvent is HFIP with the standard concentration of 2 mg mL^{-1}.

Table 2-2. Summary of the samples prepared by the solvent-switch method (**S**).

Sample	Compound	Preparation method	Solvent	Organic solvent content (%)	Concentration (mg mL^{-1})
12(S)	12	Solvent-switch	HFIP	2	2.0
13(S)	13				
13(S-low)					0.1
13(S-20%)				20	2.0
13(S-*i*PrOH-20%)			*i*PrOH	20	
13(S-Ace-20%)			Acetone	20	
13(S-Ace-20%-high)					20.0
13(S-DMAc)			DMAc	2	2.0
14(S)	14		HFIP		
15(S-DMAc)	15		DMAc		
16(S)	16		HFIP		
17(S-DMAc)	17		DMAc		

c) Film-forming method (F): The oligosaccharide was dissolved in the solvent (10 mg mL^{-1}) and dried on the glass slide.

Table 2-3. Summary of the samples prepared by the film-forming method (**F**).

Sample	Compound	Preparation method	Solvent	Concentration (mg mL^{-1})
12(F)	12	Film-forming	HFIP	10.0
13(F)	13			
14(F)	14			
15(F)	15			
16(F)	16			
17(F)	17			
18(F)	18			

19(F)	19			
20(F)	20			
21(F)	21			
22(F-water)	22		water	

3. Supramolecular assembly and chirality of synthetic carbohydrate materials

This chapter has been modified in part from the following articles:

S. Gim, G. Fittolani, Y. Nishiyama, P. H. Seeberger, Y. Ogawa, M. Delbianco, Supramolecular assembly and chirality of synthetic carbohydrate materials. *Angew. Chem. Int. Ed.,* **2020**, 132(50), 22766-22772.
S. Gim, G. Fittolani, Y. Yu, Y. Zhu, P. H. Seeberger, Y. Ogawa, M. Delbianco, Targeted chemical modifications identify key features of carbohydrate assemblies and generate tailored carbohydrate materials. *Chem. Eur. J.*, **2021**, 27(52), 13139-13143.

3.1. Introduction

Having discovered that simple synthetic oligosaccharides can self-assemble in different morphologies (chapter 2),[76] I hypothesized that these systems could offer a new bottom-up approach to understand and exploit carbohydrate materials. Assemblies of other biomolecules, such as peptides and nucleic acids, have been studied extensively, often relying on synthetic analogues.[2b, 77] These synthetic compounds simplified the analysis and identified specific interactions responsible for the assembly of the natural counterpart.[78] For example, di-phenylalanine (**FF**) (**Figure 3-1**) was identified as minimal repeating unit of the amyloid fibrils involved in the Alzheimer's disease progression.[79] This system permitted to unveil mechanistic processes of amyloid formation and to design novel inhibitors.[80] Due to its ability to self-assemble in several geometries, this simple dipeptide found hundreds of applications in nanotechnology.[81] Similarly, I planned to use a simple oligosaccharide as model to shine light on the aggregation of polysaccharide materials.

Despite the tendency of polysaccharides to form materials with outstanding mechanical and photophysical properties,[23a, 82] only few examples of synthetic carbohydrate-based assemblies were reported.[83] The hydrophilic nature of simple monosaccharides has been mainly exploited to decorate supramolecular systems[3c] or to generate glycoamphiphiles forming low molecular weight gelators.[84] Still, the structural role of the carbohydrate part remained mostly overlooked.

Recently, it became clear that carbohydrates could guide and stabilize the formation of supramolecular structures, because of their ability to form directional interactions.[85] Still, understanding their mode of aggregation and types of intermolecular interactions remains a challenge. Model systems are essential to capture molecular details responsible for the formation of carbohydrate materials and to develop reliable analytical methods.[86] In addition, systematic site-specific modifications could prompt the identification of key features of the supramolecular organization, such as particular H-bonds[87] and carbohydrate-aromatic interactions,[88] and could generate novel geometries.

I have identified disaccharide **13-D** (referred as **13** in chapter 2, **Figure 3-1**) as an ideal model to study molecular self-assembling in polysaccharides. This compound offers several advantages to develop analytical methods that can be translated to the study of natural carbohydrate materials. **13-D** i) is easy to

synthesize, ii) can form tunable supramolecular structures, contains aromatic functionalities that iii) stabilize the self-assembly and iv) make it less susceptible to electron beam irradiation allowing for electron microscopy (EM) analysis.[89]

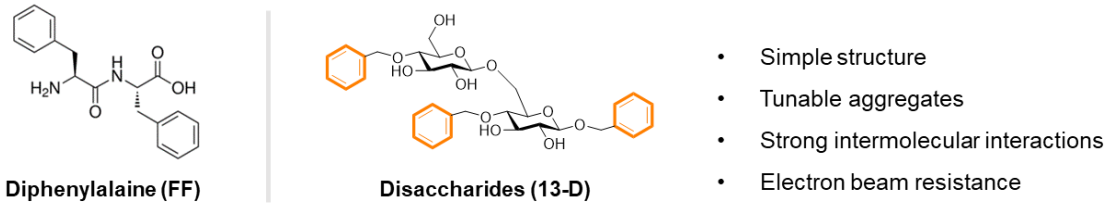

Figure 3-1. Chemical structure of diphenyl alanine **FF** (left). Chemical structure and features of the D-glucose disaccharide **13-D** (right).

Microcrystal electron diffraction (MicroED) gained popularity for structural determination in self-assembled systems since it directly reveals the molecular organization in the native state, avoiding tedious crystallization trials that can alter the supramolecular organization.[64, 90] Nanoscale structural heterogeneities of molecular solids can be characterized due to the small electron probe size.[91] To date, MicroED has been employed rarely to study simple oligosaccharides due to their sensitivity to the electron beam. **13-D** is an ideal substrate to develop MicroED, since the benzyl groups present in the molecule render it more resistant to prolonged irradiation.[89] MicroED, optimized for carbohydrate samples, was employed to reveal key interactions that drive the self-assembly, suggesting insights into the mechanism of formation.

Seven analogous of **13-D** were designed and examined to modulate specific intermolecular interactions based on the molecular packing model obtained from microED. The synthesis was performed by G. Fittolani, Dr. Y. Yu, and Dr. Y. Zhu. The microcrystal electron diffraction and tomography analysis were carried out by Dr. Y. Ogawa (Cermav).

3.2. Results

3.2.1. Assembly methods

Two different methods (*e.g.* solvent-switch (**S**) and film-rehydration (**FR**)) were selected to trigger the formation of supramolecular structures (**Figure 3-2**). HFIP was employed as a good organic solvent for both the methods. The sample names indicate the disaccharide (*e.g.* **13-D**) and the assembly method (*e.g.* **S** or **FR**). For example, **13-D(S)** means compound **13-D** prepared by solvent switch method (**S**). The content of organic solvent (*e.g.* **10%**) can be appended to the sample name. If not mentioned, the standard HFIP content is 2%. Details for the sample preparation are described in the experimental section, **3.4.2**.

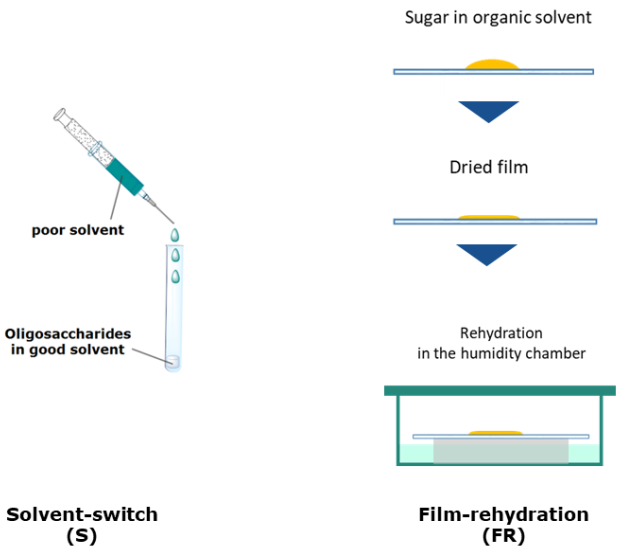

Figure 3-2. Cartoon representation of the sample preparation methods used in this study.

3.2.2. Structural analysis of compound 13-D

XRD analysis indicated the high crystallinity of the assembly (**Figure 3-3**). The splitting of the two anomeric carbon signals in solid-state nuclear magnetic resonance (ssNMR) (**Figure 3-4**, C_1, highlighted with the red box) indicated the presence of two differently oriented sets of **13-D** in a single unit cell. MicroED analysis on **13-D(S)** crystals was performed at cryogenic temperature. Electron diffraction patterns obtained from the non-twisted part provided spot diffraction patterns with a resolution of about 1.2 Å, indicating its single crystal nature and high crystallinity (**Figure 3-5A**). The structure was determined based on a tilt series MicroED analysis as an orthorhombic unit cell with *a* = 5.2 Å, *b* = 20 Å, *c* = 37 Å (**Figure 3-5** and **3-6C**). The reflection positions calculated based on the ED analysis are in general agreement with those in the powder X-ray diffraction profile (**Figure 3-3**). The calculated reflection positions are lower angle shifted due to a slight overestimation of unit cell dimensions by the ED analysis, as previously demonstrated for native cellulose crystals.[92] The unit cell contains four **13-D** molecules, giving a density of 1.06 g/cm^3. The tentative molecular packing model in *bc* and *ac* projections (**Figure 3-6C**) show a short *a*-axis indicating that **13-D** molecules assume an overall flat conformation and stack along the *a*-axis (**Figure 3-6B**). The glucose ring planes are oriented roughly in the *bc* plane. The aromatic rings assemble in close proximity to each other. The interactions between the aromatic rings are mostly C-H···π type edge-to-face interactions. No face-to-face π-π stacking is present in the packing model, as the molecular spacing in the stacking direction (5.2 Å, *a*-axis), is larger than the maximum acceptable distance for π-π stacking formation (3.8 Å).[93] The carbohydrate moieties are not in close contact with each other. The relatively low density of the crystal implies that water molecules may be involved in the crystalline lattice. The distances between hydroxyl groups of adjacent molecules allow forming water-bridged hydrogen bonds with a single water molecule

between the hydroxyl groups. Further refinement will permit to explicitly determine the presence of water as well as the hydrogen bonding network in the crystal structure.

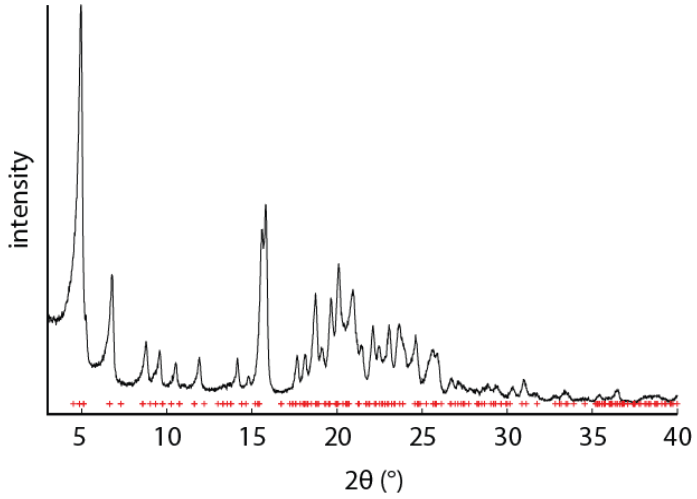

Figure 3-3. Powder X-ray diffraction pattern (black line) and reflection positions calculated based on the MicroED unit cell (red cross) for **13-D(S)**.

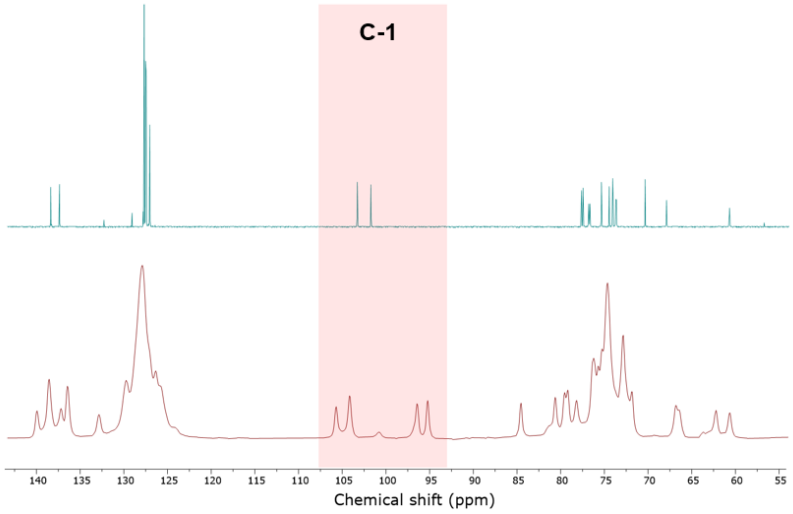

Figure 3-4. NMR analysis of compound **13-D** in solution ($CDCl_3$, top) and in solid state **13-D(S)** (bottom). C-1 anomeric peaks are highlighted with a red square.

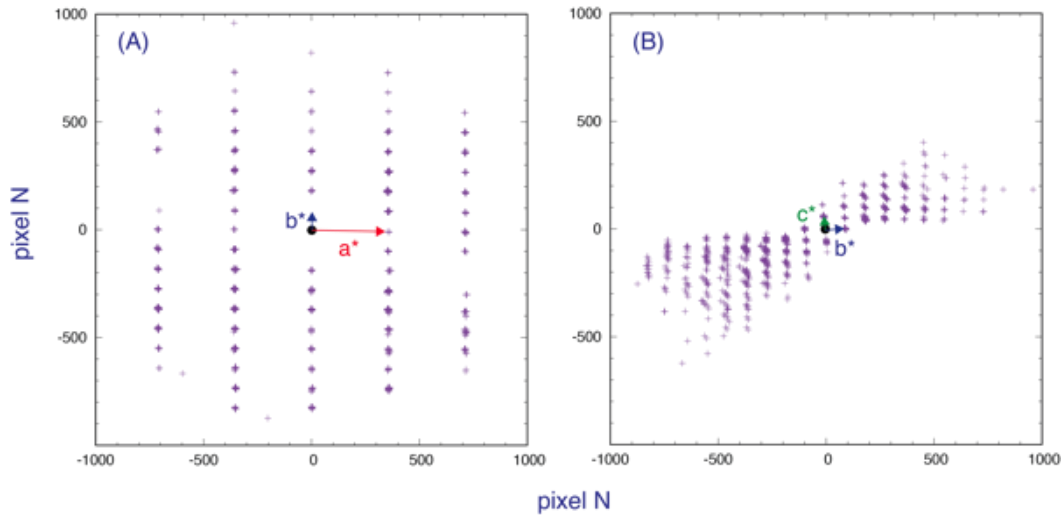

Figure 3-5. Reciprocal lattice reconstructed from the tilt-series microED patterns of **13-D(S)** in (A) a*b* projection and (B) b*c* projection.

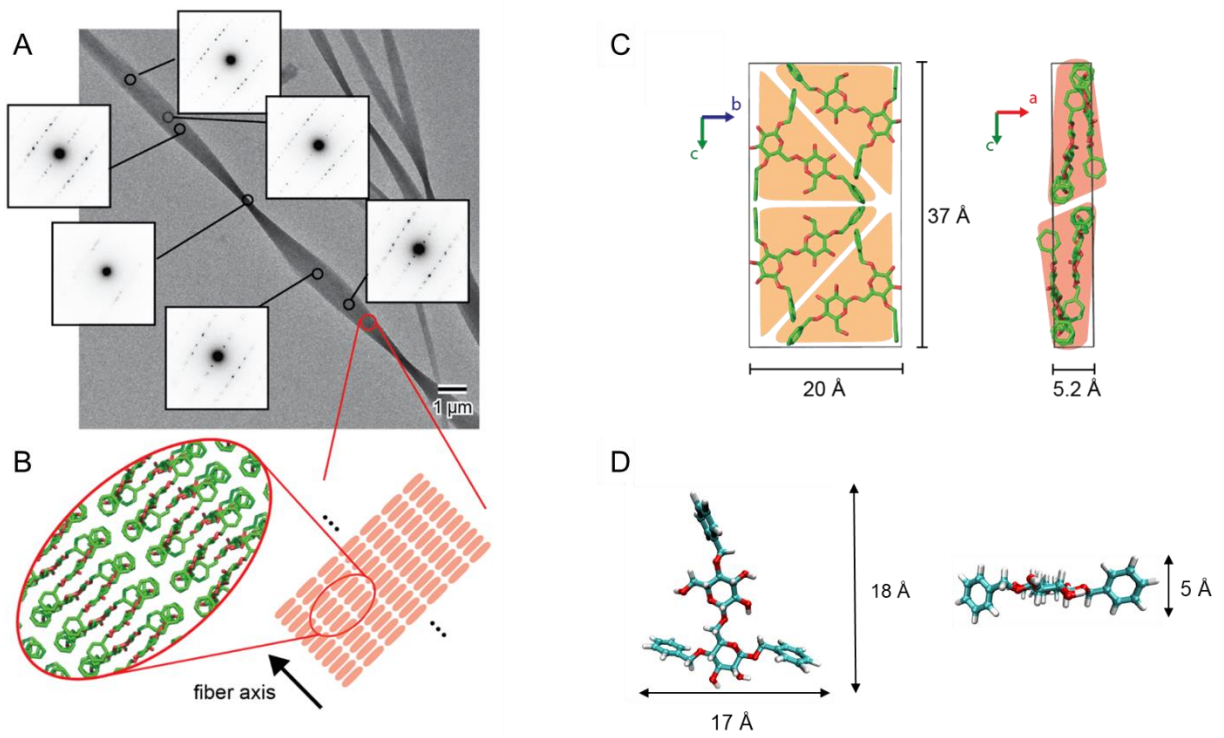

Figure 3-6. (A) MicroED analysis of self-assembled **13-D(S)** with twist geometry followed by sequential electron diffractions. (B) Schematic image of molecular packing manner in the fibrillar **13-D(S)** crystal. (C) Tentative molecular packing model of **13-D(S)** in the unit cell determined from tilt-series MicroED experiments. Hydrogens are removed for clarity. (D) Energy minimized computational model of **13-D**. The initial conformation of the structure was constructed with tleap. The topology was converted to gromacs format using the glycam2gmx.pl script and solvated with 2100 water molecules (TIP5P[94]) using gromacs tools.[95]

In addition to crystallographic information, MicroED can provide structural insight into larger scale supramolecular structures, such as a twist. Ready correlation of local molecular organization with supramolecular assembly could revolutionize the description of supramolecular systems based on small molecules, but has been hardly exploited.[96] The **13-D(S)** crystals were subjected to a sequential electron microdiffraction experiment with an electron probe size of about 100 nm. Each ED pattern obtained along the fiber axis corresponds to a different lattice projection (**Figure 3-6A**), revealing left-handed twists along their fiber axes. In all ED patterns, the *a**-axis is oriented along the fiber axis of the crystal, indicating that the stacking of flat molecular sheets happens parallel to the fiber axis (**Figure 3-6B**). The crystal twists along the stacking direction, implying that this supramolecular twist is likely to originate from a slight rotation between the stacked molecules. The apparent half twist pitch (180 degree rotation) is about 5 μm in most crystallites, resulting in a rotation per unit cell of about 0.02 degree. While crystal twists were observed previously for natural carbohydrate crystals such as cellulose and chitin, the mechanism of twisting of carbohydrate crystals is still elusive.[97] These results suggest that well-defined synthetic systems could shine light on the twisting mechanism of natural systems as well as on the relationship between molecular chirality and supramolecular structures.

3.2.3. Tuning supramolecular helicity

3.2.3.1. Modulation of environmental conditions

The system was tunable and different morphologies were observed when the self-assembly was performed at different temperatures (**Figure 3-7**). At high temperature (75 °C), **13-D** developed into large flat fibers (width in the μm range). Those fibers became shorter and thinner (width < 0.5 μm) with a narrow distribution as the assembly temperature was decreased (**Figure 3-8**). Circular dichroism (CD) revealed a minimum at 234 nm for the twisted fibers. No signal between 200 and 400 nm was detected for the flat fibers (**Figure 3-9**). Electron and X-ray diffraction analysis showed the same pattern for the three samples, confirming identical crystalline structure, yet different fibril dimensions (**Figure 3-7C** and **3-7D**).

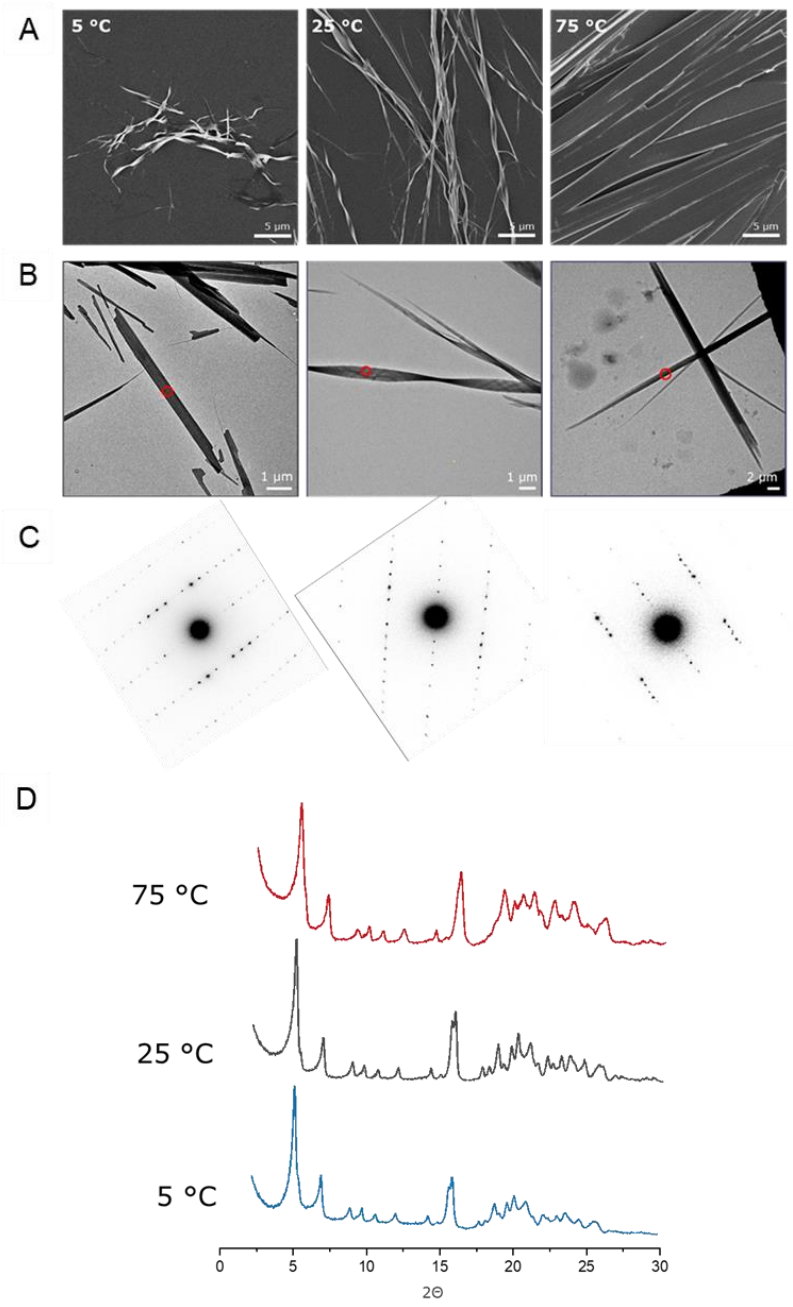

Figure 3-7. SEM (A) and TEM (B) images, electron diffraction patterns (C, from a red circled area in B) and XRD diffraction patterns (D) of **13-D(S)**, prepared at different temperature (left: 5 °C, middle: 25 °C, and right: 75 °C). The results indicate that the three compounds have the same crystal structures, but different fibril dimensions.

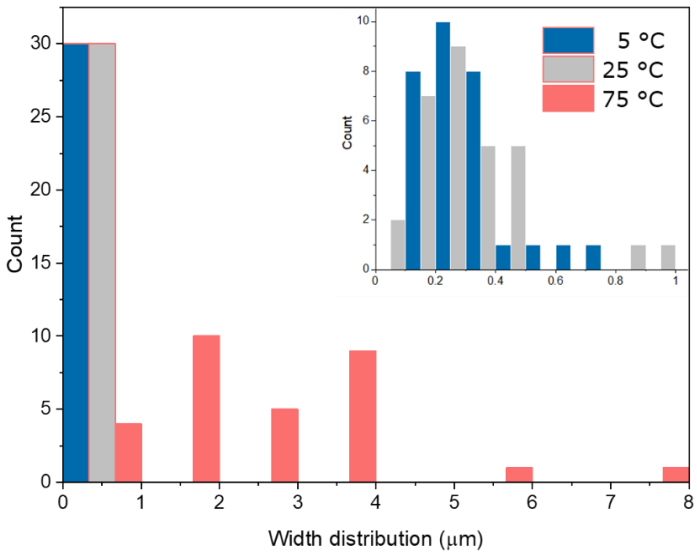

Figure 3-8. Width distribution of **13-D(S)** prepared at different temperatures (inset: enlarged diagrams for 5 °C and 25 °C).

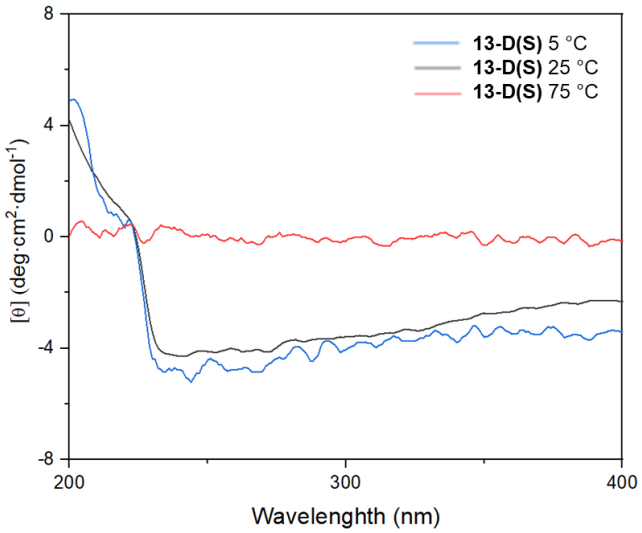

Figure 3-9. CD spectra of **13-D(S)** prepared at different temperatures.

The fiber length and the helical pitch were controlled by adjusting the content of organic solvent (**Figure 3-10**). Longer fibers with larger pitches were observed with higher amounts of HFIP (up to 10% v/v). The higher HFIP content resulted in slower aggregation rates. A further increase in HFIP content (20% v/v) prevented the formation of fibril structures. Disruption of the helical fibers and transition to the monomer state were monitored by CD upon sequential addition of HFIP to **13-D(S)** (**Figure 3-11**).

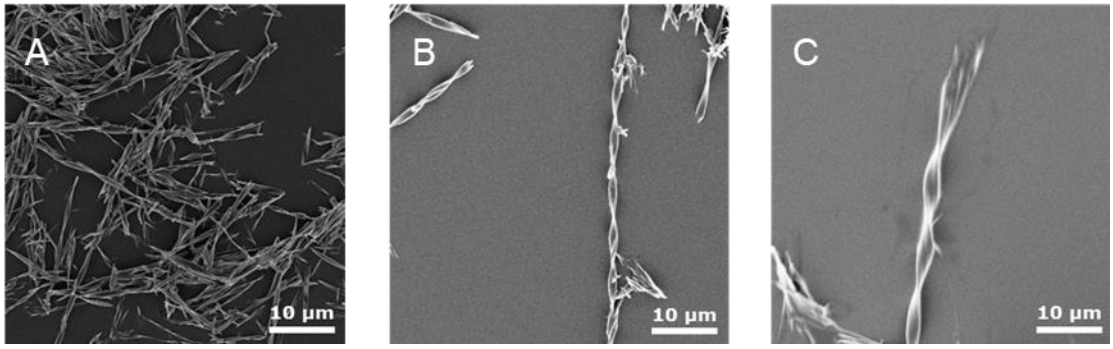

Figure 3-10. SEM images of **13-D(S)** prepared with different ratios of HFIP to water. (A) **13-D(S)**, (B) **13-D(S-5%)**, and (C) **13-D(S-10%)**.

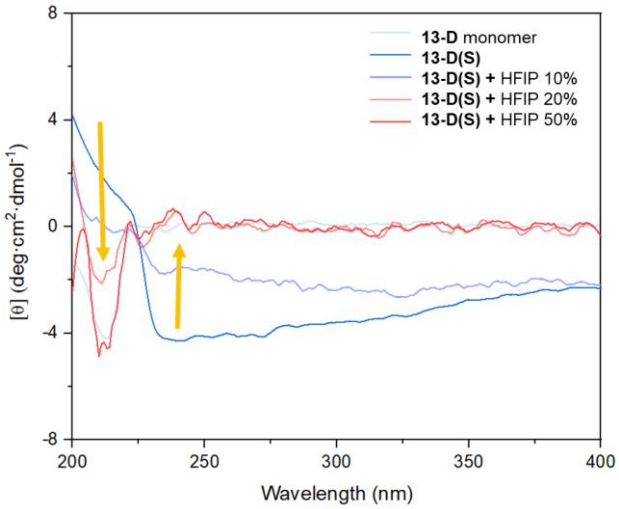

Figure 3-11. CD spectra shift from **13-D(S)** to **13-D** monomers (300µM in HFIP) with sequential addition of HFIP.

3.2.3.2. Modulation of molecular chirality

The helicity of the fibers offers an additional tool to tune the properties of self-assembled materials.[98] In particular, heterochiral peptide-based systems offer many advantages such as increased stiffness of the self-assembled fibers,[99] increased stability towards enzymatic degradation,[100] and access to new morphologies.[101] Inspired by the work on heterochiral peptide-based systems, the enantiomeric disaccharide (**13-L**) was synthesized starting from L-glucose. Upon solvent switch, **13-L(S)** formed the enantiomeric helical fibers (right handed), confirming the direct correlation between oligosaccharide chirality and fiber helicity (**Figure 3-12**). The racemic mixture **13-DL(S)** aggregated in a completely new and flat geometry, where no chiral features were observed, in a highly organized manner (**Figure 3-12** and **3-13**). The CD spectra recorded for **13-D** and **13-L** monomers showed a peak at 212 nm, with opposite signs for the two enantiomers (**Figure 3-14A**). Their aggregation exhibited the highest absorption at 234 nm, yet no signal was observed for the co-assembly of **13-D** and **13-L**, suggesting absence of supramolecular chirality.

XRD confirmed that both enantiomers, **13-D(S)** and **13-L(S)**, have identical crystallinity, whereas the racemic mixture packs in a different manner (**Figure 3-14B**), as previously observed for heterochiral peptides assemblies.[101] Alteration of the 1:1 ratio between **13-D** and **13-L** creates irregularity in the structure, likely composed of flat structures and helical fibers (**Figure 3-15**). AFM analysis of the flat aggregates (**13-DL(S)**) suggests that the two enantiomers may construct a layer-by-layer supramolecular assembly (**Figure 3-16**). The height of the sheets varies from a few hundreds nanometer to several micrometers, with the single layer measuring 1.5 nm, which is comparable to one dimension of the disaccharide (**Figure 3-6D**). This may indicate that the disaccharides in the racemic mixture align laterally forming a single layer, as previously observed for heterochiral peptide assemblies.[102]

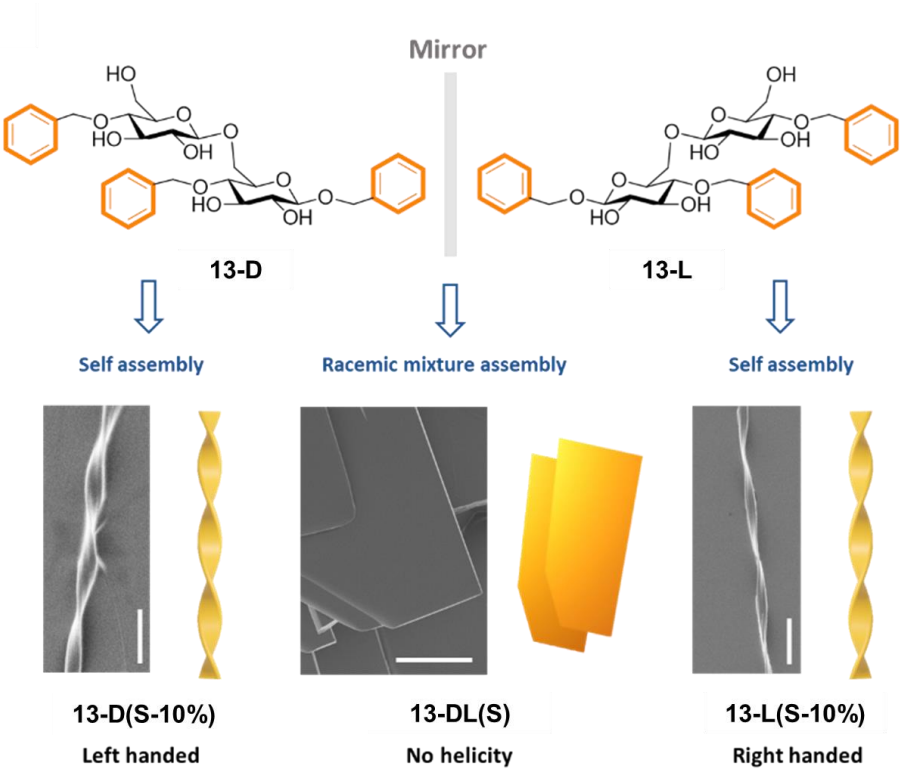

Figure 3-12. Chemical structures of the **13-D** and **13-L** enantiomers and SEM images of their supramolecular assembly (Scale bars: 10 µm).

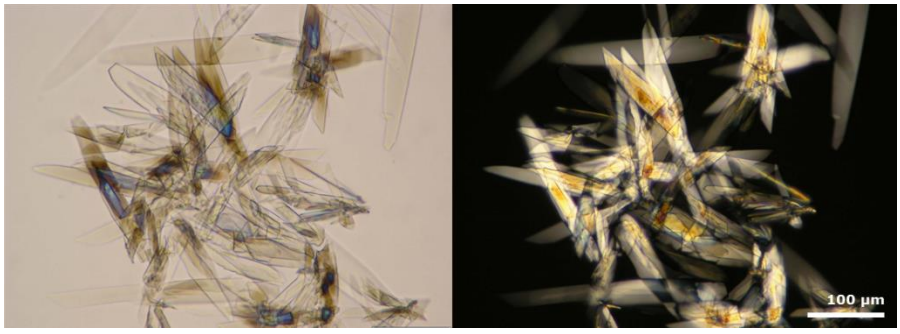

Figure 3-13. POM images of **13-DL(S)** taken between parallel (left) and crossed (right) polarizers.

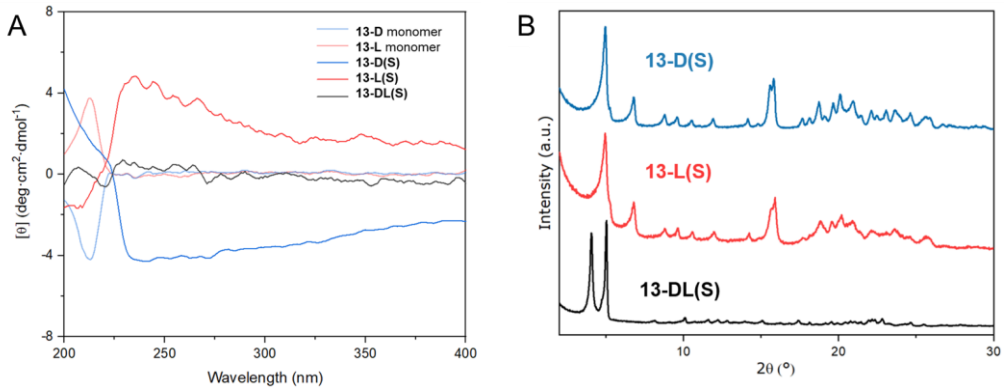

Figure 3-14. (A) CD spectra of the disaccharides (**13-D** and **13-L** monomers) and their aggregates (**13-D(S)**, **13-L(S)**, and **13-DL(S)**). (B) XRD patterns for **13-D(S)** (blue), **13-L(S)** (red), and 13-**DL(S)** (black).

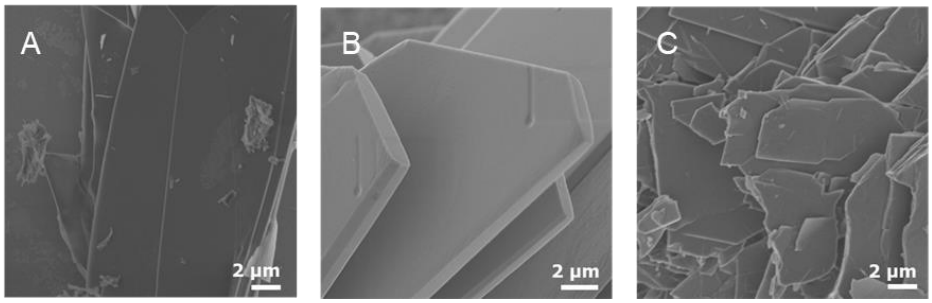

Figure 3-15. SEM images of **13-DL(S)** prepared with different **13-D**:**13-L** ratios. (A) 2:1, (B) 1:1, and (C) 1:2.

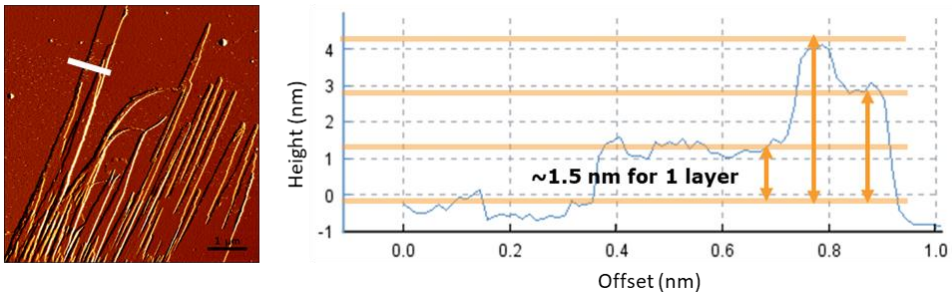

Figure 3-16. AFM image and cross-sectional analysis of **13-DL(S)**.

3.2.4. Self-assembly on a 2D surface

The possibility of performing self-assembly directly on a 2D surface is attractive, as it can generate films with controlled morphologies.[103] Such designer surfaces have found applications[104] in catalysis[105], as semiconducting materials[106], as chemical sensors [107], and as optical devices [108]. Additionally, monitoring the assembly on a two dimensional surface could give insights into the assembly mechanism due to the slower nucleation and crystallization rate at the interface.[109] A continuous film was generated upon drop casting of a HFIP solution of **13-D**. The 2D self-assembly was repeated, incubating the drop-casted film in a humidity chamber with saturated vapor (**Figure 3-2**, right). Dewetting of thin film using an anti-solvent is

a common procedure to generate particular morphologies on surfaces and relies on the spontaneous surface diffusion and organization of the material.[110] The assembly progression was monitored with polarized optical microscopy (POM). Three samples were prepared from solutions of **13-D**, **13-L** and the racemic mixture **13-DL**. The drop-casted films are amorphous, resulting in black background when observed between crossed polarizers (**Figure 3-17D** and **3-18A**). Upon hydration (3 h), the films obtained from **13-D** and **13-L** developed spherulites composed of a nucleation center and multiple lamellas growing from the core (**Figure 3-17E**, **3-17F**, and **3-18B**). The cross-sectional images clearly showed the transition from amorphous to a crystalline structure and the directional alignment of fibers (**Figure 3-18**). The crystallization process produced the classical maltese cross pattern. Different parts of the film show slightly different patterns, likely due to small differences in local concentration. The core showed complete separation of each spherulite (**Figure 3-17E**), whereas the boundary shows densely connected spherulites (**Figure 3-17F**). The racemic mixture **13-DL** does not form any defined structure. The XRD profile of **13-D** film at t = 0 confirms its amorphous nature; sharp peaks develop upon hydration, indicating crystallization (**Figure 3-18C**).

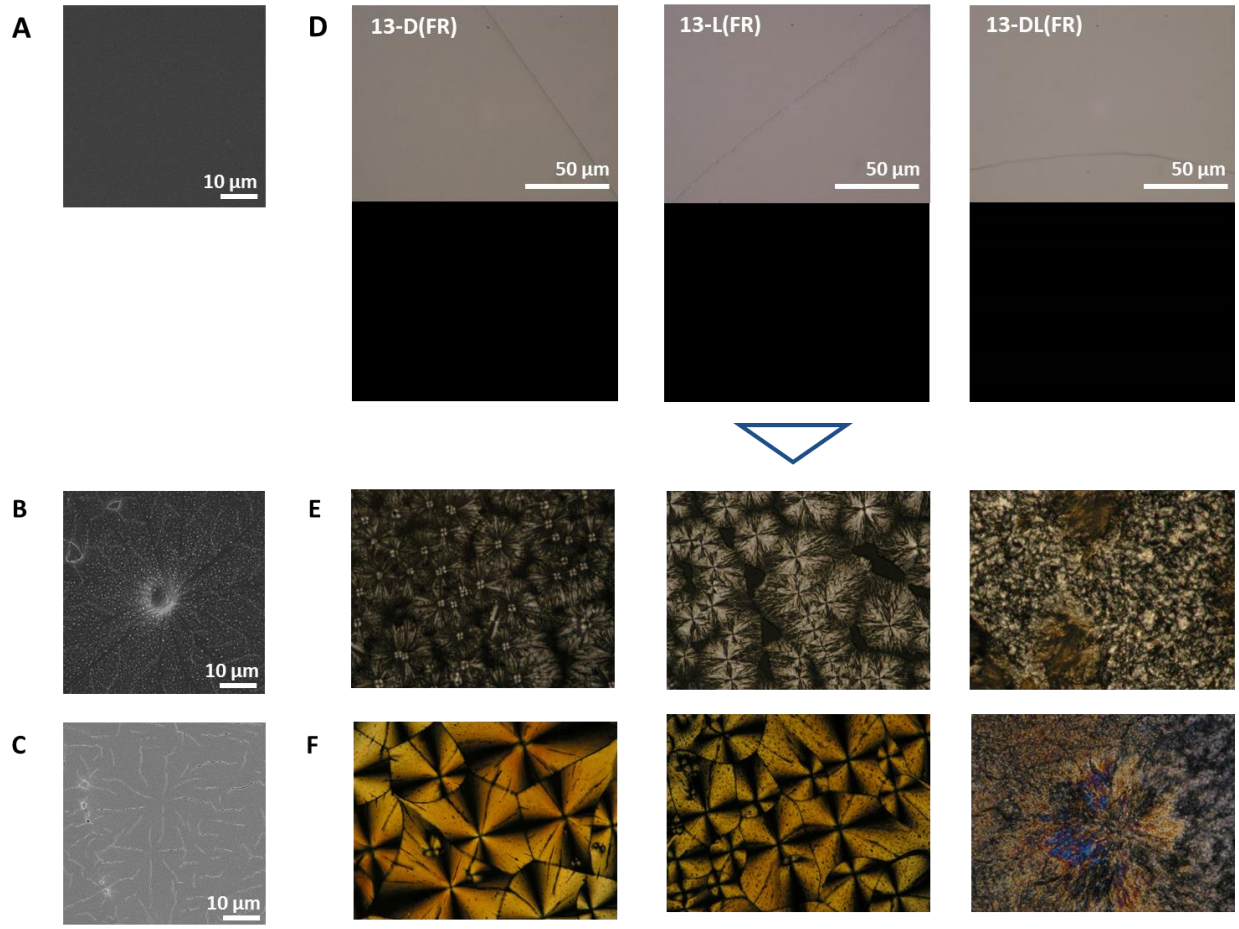

Figure 3-17. SEM images of **13-D(FR)** (t = 0, A) and **13-D(FR)** (t = 3 h, B: center/C: boundary). POM images of **13-D(FR)**, **13-L(FR)**, and **13-DL(FR)** at time 0 (D) and after 3 h (center (E) and boundary (F) of the film). **13-D(FR)** and **13-L(FR)** show identical patterns.

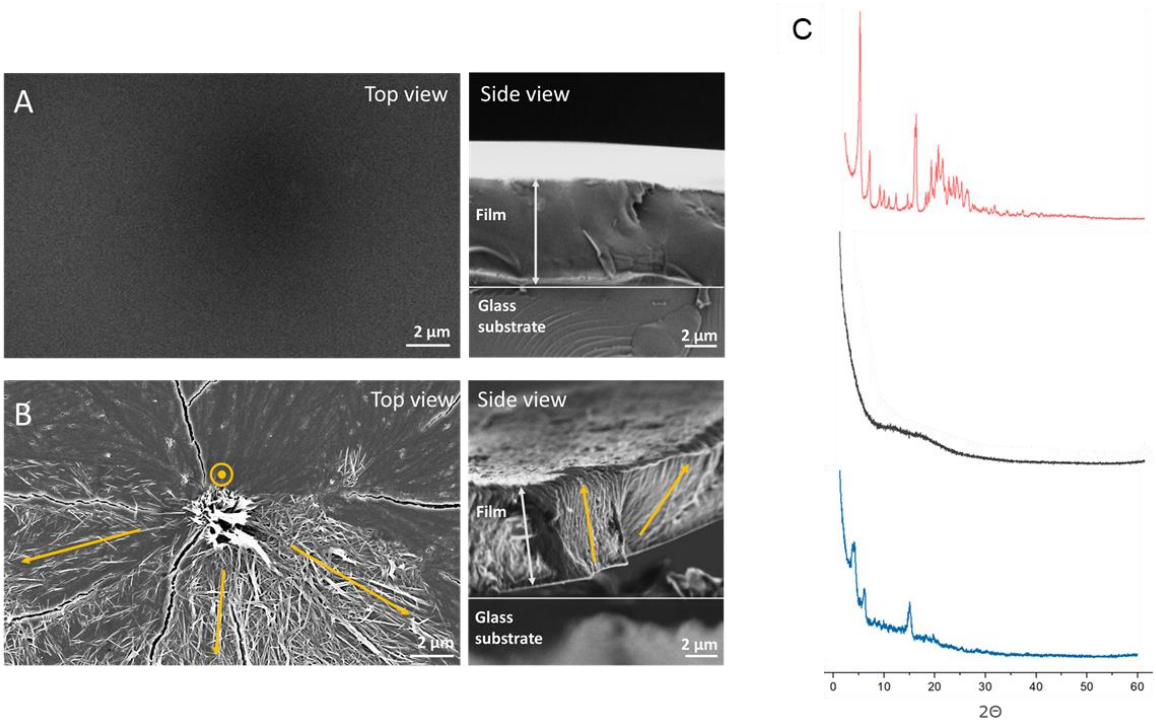

Figure 3-18. SEM cross-sectional images of **13-D(FR)** before (A) and after (B) hydration. (C) XRD profiles of **13-D(S)** (red), **13-D(FR)** (t = 0, black) and **13-D(FR)** (t = 3 h, blue). The sample was directly prepared on the XRD sample holder, zero diffraction silicon. The **13-D(FR)** (t = 0) is amorphous, showing a low intensity broad peak between 5° and 25°. Upon rehydration **13-D(FR)** (t = 3 h) develops sharp peaks, identical to the peaks observed for the sample obtained upon solvent switch (**13-D(S)**).

The nucleation process can be monitored in real time, offering the opportunity to explore crystallization kinetics (**Figure 3-19**). Upon hydration, the amorphous film starts to nucleate, developing highly organized spherulites showing the classical maltese cross (when observed between cross polarizers). The interaction of the molecules in the film with the water vapor (hydrophobic interaction) triggers a structural reorganization and promotes the assembly of **13-D** into a fibrous structure. The fibers grow radially from the nucleation core, giving rise to highly organized morphologies, until they encounter an adjacent spherulite. Additional nucleation is observed during the crystallization process (**Figure 3-19**, white circles). The radius of the spherulites doubles every 10 minutes. The transition from amorphous to crystallized state is completed within 3 h. During this transition, the mechanical properties of the film are drastically affected, as shown by the nanoindentation experiments (**Figure 3-20**). The stiffness of the **13-D(FR)** film increased after exposure to water vapor. The amorphous film has a Young's modulus of 2.047 ± 0.060 GPa. After vapor-induced crystallization, the film shows a 3-fold increased stiffness, 6.072 ± 1.429 GPa.

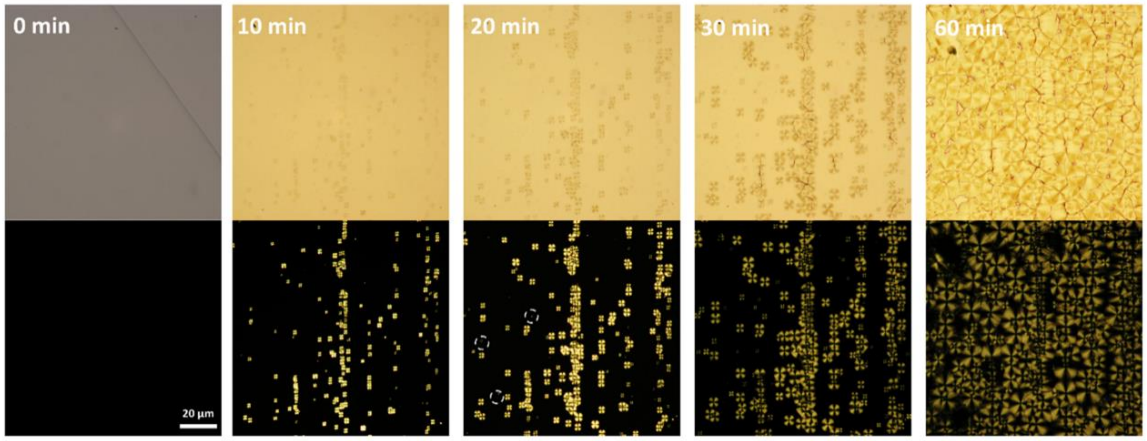

Figure 3-19. POM images of **13-D(FR)** at 0, 10, 20, 30, and 60 minutes observed between parallel (top) and crossed (bottom) polarizers. White circles represent additional nucleation observed after 20 minutes.

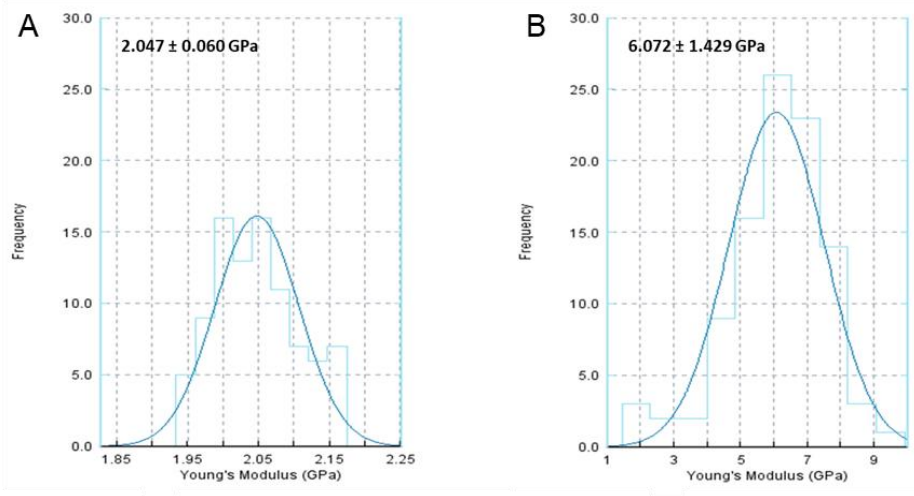

Figure 3-20. Young's modulus measured for **13-D(FR)** at t = 0 (no hydration, A) and at t = 3 h (B) at a constant force of 800 nN.

3.2.5. Single site modification

Based on the tentative molecular packing obtained from MicroED (chapter 3.2.2.), the intermolecular interactions responsible for the formation of the supramolecular fibers of **13-D** are C-H···π type edge-to-face interactions between the aromatic rings and water-bridged hydrogen bonds between adjacent hydroxyl groups (**Figure 3-21B**, highlighted with green and blue circles). In order to validate the proposed crystal organization and explore the flexibility of the system, we designed seven analogues of compound **13-D** (**Figure 3-21**). Each modification aimed to disrupt a particular interaction, and therefore to highlight the

importance of the replaced functionality for the assembly process. Compounds **23**, **24**, and **25** possess the same benzyl (Bn) group pattern as **13-D** and are modified at the hydroxyl groups of the glucose unit at the non-reducing end. In compound **23**, the hydroxyl group at the C-6 position is alkylated with a carboxymethyl group. This moiety introduces a negative charge in the structure and could be exploited for conjugation. Additionally, the carboxylic acid should be still available for H-bonding, albeit with an increased steric bulk.[111] **24** and **25** are the C-6 and C-3 deoxyfluorinated analogues, respectively. Deoxyfluorination was designed to selectively disrupt particular H-bonds.[112] Additionally, the substitution of an OH group for a F atom should increase lipophilicity and affect the dipole of the molecule.[113] Compound **26** has a slightly different Bn pattern and compound **27** bears a pentafluorobenzyl (PFB) group at the anomeric position. Both modifications were designed to explore how the orientation and electronics of the Bn groups affect the supramolecular assembly. In particular, the PFB group does not engage in C-H···π edge-to-face stacking, because the electron-rich *para*-F does not interact with electron-rich phenyl rings.[114] Compounds **28** and **29** are more heavily modified to explore the flexibility of the system.

3.2.5.1. Self-assembly of analogous of 13-D

Upon solvent switch, **23** and **24** formed insoluble fiber-like structures (**Figure 3-21C** and **3-21D**), whereas **25**-**29** remained soluble. These results suggest that the assembly process tolerates modifications at the C-6 position (**Figure 3-21B**, highlighted with dotted circles). Compared to the assembly of **13-D**, **23** developed into longer and thicker fibers without helicity, while fibrils from **24** were shorter, thinner, and highly twisted. The assembly outcome was drastically different for the monofluorinated compounds **24** and **25** (**Figure 3-21D** and **3-21E**), demonstrating the importance of the 3-OH for the supramolecular assembly (**Figure 3-21B**, highlighted with a green circle). For the latter, colloidal particles rather than fibers were observed with cryogenic SEM measurement (**Figure 3-28D**). Alteration in the Bn pattern prevented the formation of any defined structure (**Figure 3-21F**, **G**, **H**, and **I**), indicating that the C-H···π type edge-to-face interactions are crucial (**Figure 3-21B**, highlighted with blue circles).

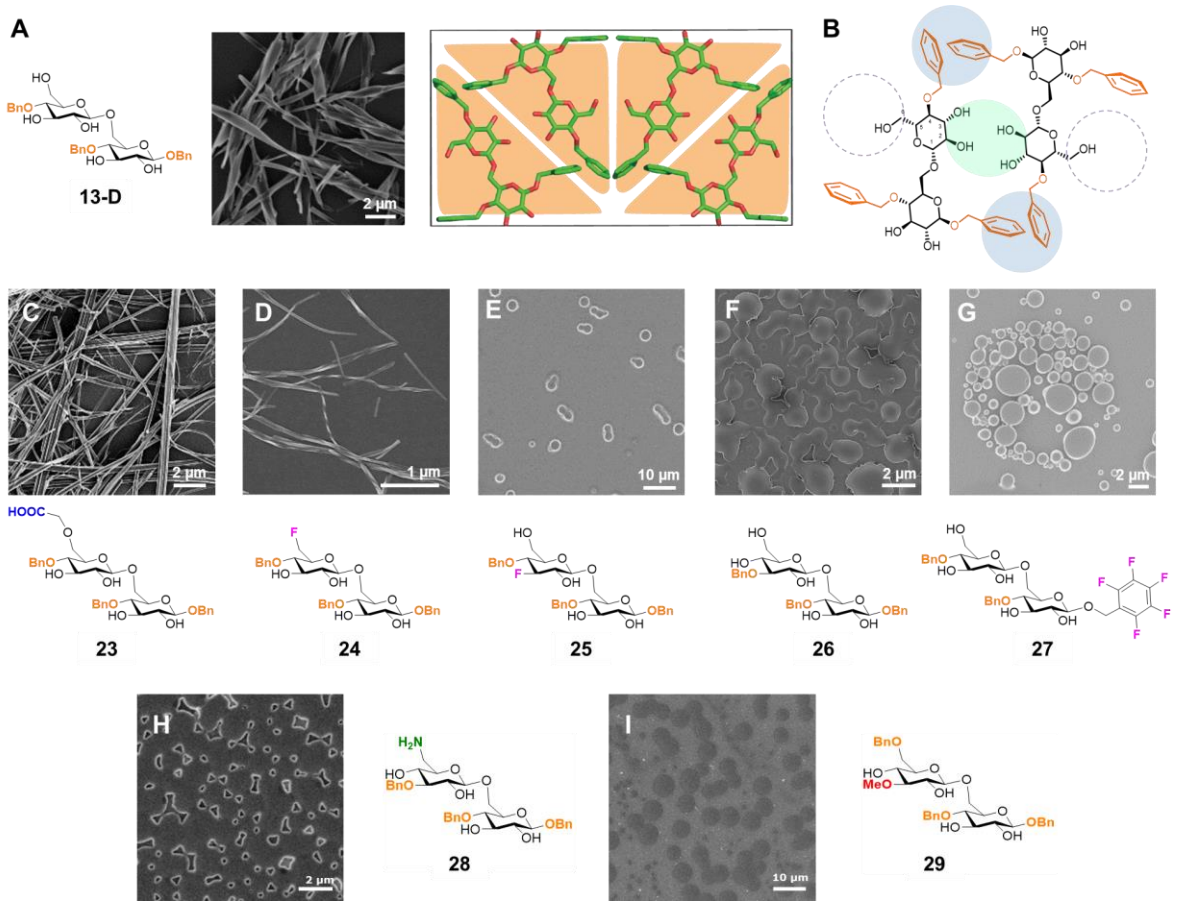

Figure 3-21. (A) Chemical structure of **13-D**, SEM image of its assembly and tentative molecular packing model of **13-D** in the unit cell. (B) Schematic representation of the unit cell to highlight the site of modifications. Chemical structures and SEM images of their assemblies for **23** (C), **24** (D), **25** (E), **26** (F), **27** (G), **28** (H), and **29** (I).

This first screening identified **23** and **24** as the only compounds able to maintain the fiber-like structure. Thus, I focused on their self-assembly processes and crystalline structures. I previously captured the real-time assembly of **13-D**, showing that the fibers generated from highly concentrated HFIP droplets containing the oligosaccharide, upon addition of water (chapter 2, **Figure 2-9**). The same phenomenon was observed for **24** (**Figure 3-22B**), whereas precipitation of **23** followed much slower kinetics and could not be monitored in real time. Therefore, crystallization of **23** was followed with polarized optical microscopy on a surface, revealing that the formation of highly organized crystalline fibers, with length of hundreds of µm, was completed after a week (**Figure 3-22C**). The powder XRD and microED patterns of **24** were similar to **13-D** (**Figure 3-23**). Still, the fibers from **24** retained a higher level of flexibility in the lateral plane, suggesting that lateral aggregation was stabilized by hydrogen bonds involving the hydroxyl group at the C-6 position.

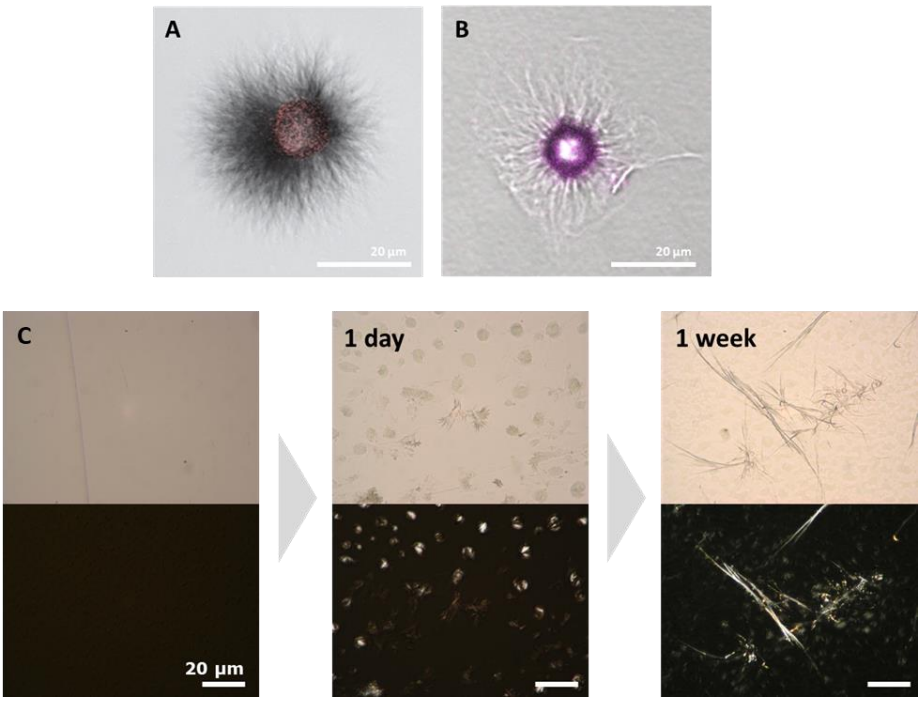

Figure 3-22. Confocal microscopy images of the fiber formation of **13-D(S)** (A) and **24(S)** (B) obtained upon solvent switch method. The fibers are generated radially from a droplet of oligosaccharide in HFIP upon addition of water. The images were captured after 10 minutes of addition of water. (C) Polarized optical microscopy images of the fiber formation of **23** obtained upon film-rehydration. The assembly of **23** is much slower than for **13-D** and **24**, therefore it was not possible to observe the transition in real time.

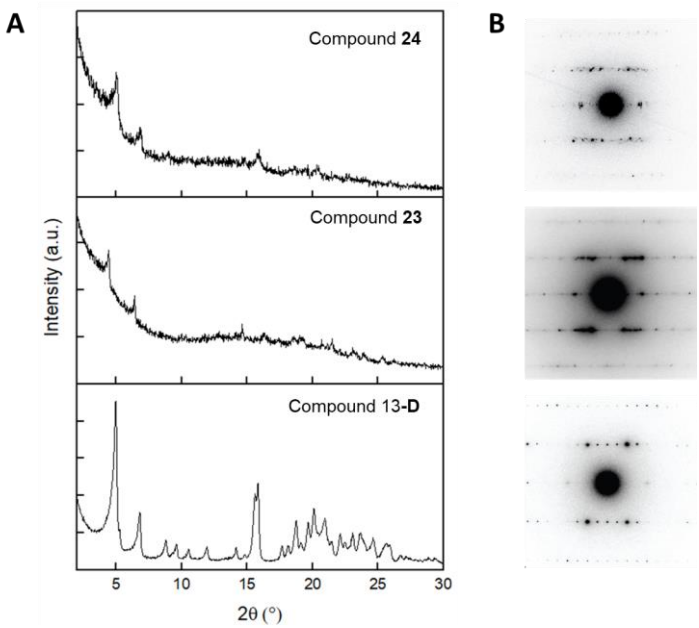

Figure 3-23. Powder X-ray diffraction (A) and microcrystal electron diffraction (B) patterns of **13-D(S)** (bottom), **23(S)** (middle), and **24(S)** (top).

The assembly of **23** was tested at different pH to study the influence of the protonation state of the carboxylmethyl moiety in the self-assembly process. Fiber-like structures were obtained regardless of the pH; yet, showing a faster growth rate and a larger amount of precipitation at lower pH (**Figure 3-24**). While tube-like fibrils made of multiple crystallites were dominant at pH 3 and pH 7, lamella type aggregates without void in the core were prevalent at pH 11. Tomography analysis revealed that the tube-like fibrils were composed of multiple crystallites with holes at the middle, sometimes connected with thin lamella-like crystals. The structure differs from a typical tube structure with a well-defined hole, often found in inorganic systems,[115] but adopts a dome-like arrangement. The component crystallites with a width of c.a. 100 nm tightly assemble into a larger fiber with several internal tunnel-like holes (**Figure 3-25A**, green arrows). The component aligns almost perfectly parallel along the fiber axis, while crystallites do not merge with each other to form a bigger single crystallite. In these tube structures, the crystal growth of individual crystallites is restricted in the lateral directions compared to the case of single-crystal fibers, resulting in holes in the middle of the structure.

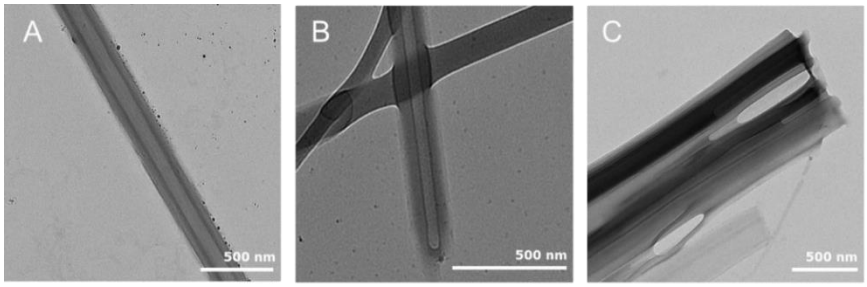

Figure 3-24. TEM images of self-assembly of **23(S)** at pH 3 (A), 7(B), and 11 (C).

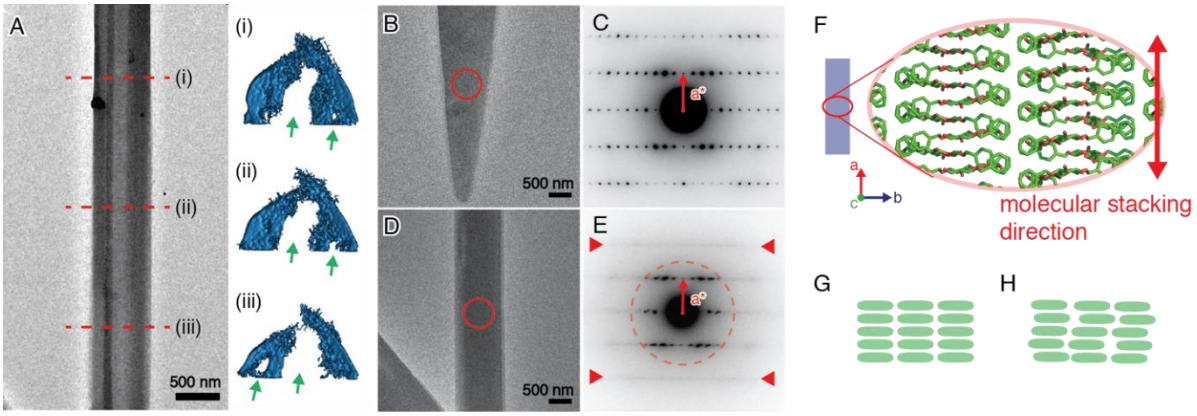

Figure 3-25. TEM image of the assembly of **23** at pH 3 with electron tomographic cross sections at different positions along its fiber axis (A). Green arrows indicate internal holes in the assembly. TEM images of the assembly of **23** at pH 3 (B, D) and electron diffraction patterns obtained from the circled areas in panel B (C) and in panel D (E), respectively. In panel E, spot-like reflections are observed only within the circled area up to the resolution of only about 3 Å. Red arrow heads indicate the streak lines. Schematic illustration of the molecular packing manner in the fibrous assembly, adapted from the packing model of the assembly of **13-D** (F).[86b] Schematic illustrations of molecular packing of **23** with (G) and without (H) long-range structural order in the lateral plane of the fibrous assembly. The microcrystal electron diffraction and tomography analysis were carried out by Dr. Y. Ogawa (Cermav).

Some single-crystal fibers provide high-resolution ED patterns (**Figure 3-25C**, the resolution can reach higher than 1 Å), indicating the crystalline organization of the molecules in the fibers (**Figure 3-25G**). The diffraction pattern is identical to that from the assembly of **13-D**. Thus, **13-D** and **23** share very similar unit cell dimensions and molecular packing. Many fibers, especially those with tube-like morphology, are polycrystalline, as ED patterns from such fibers contain more than one crystallographic projection (**Figure 3-25E**). This indicates that the component crystallites have different crystallographic orientations in the lateral plane of the fiber. Spot-like reflections appear only in the inner part of the diffraction diagram (**Figure 3-25E**, red dashed circled area) and rapidly disappear upon electron radiation. The loss of spots in the higher angle indicates the lack of strict long-range structural order. In the outer side, streaks are visible along the direction transverse to the *a** vector. Considering the molecular packing model (**Figure 3-25F**) where the *a*-axis (fiber axis) corresponds to the molecular stacking direction, the presence of the streak implies that the periodicity along the stacking direction is preserved. On the other hand, disorder should be present in the molecular organization in the lateral plane of the fiber (**Figure 3-25H**). This observation supports the hypothesis that molecular packing in the lateral plane is stabilized by the C-6 hydroxyl group involved in H-bonds. The higher presence of disordered domains might be induced by steric hindrance resulting from the bulky carboxymethyl groups or by additional water molecules solvating the carboxylic moiety.

3.2.5.2. Co-assembly with 13-D

To further explore the flexibility of this system, I performed the co-assembly between **13-D** and the other modified analogues (1:1 ratio by mass).[116] While most of the compounds were self-sorted or resulted in random aggregation, the co-assembly with C-6 substituted samples resulted in fiber formation (**Figure 3-26**). The assembly proceeded with slower aggregation rates, forming chiral fibers with enhanced helicity (**Figure 3-26A, B**, and **F**). Twisted ribbon-like structures were obtained from the co-assembly of **13-D** and **23** (**Figure 3-26A**); these aggregates have similar dimensions to the flat fibers obtained from **23** alone. The co-assembly of **13-D** and **24** generated long and highly twisted left-handed fibers with a regular pitch (**Figure 3-26B**). We speculated that co-assembly generates “defects” during crystallization, responsible for the increased twist. In addition, the decreased rate of crystallization could influence the tendency to twist.[117]

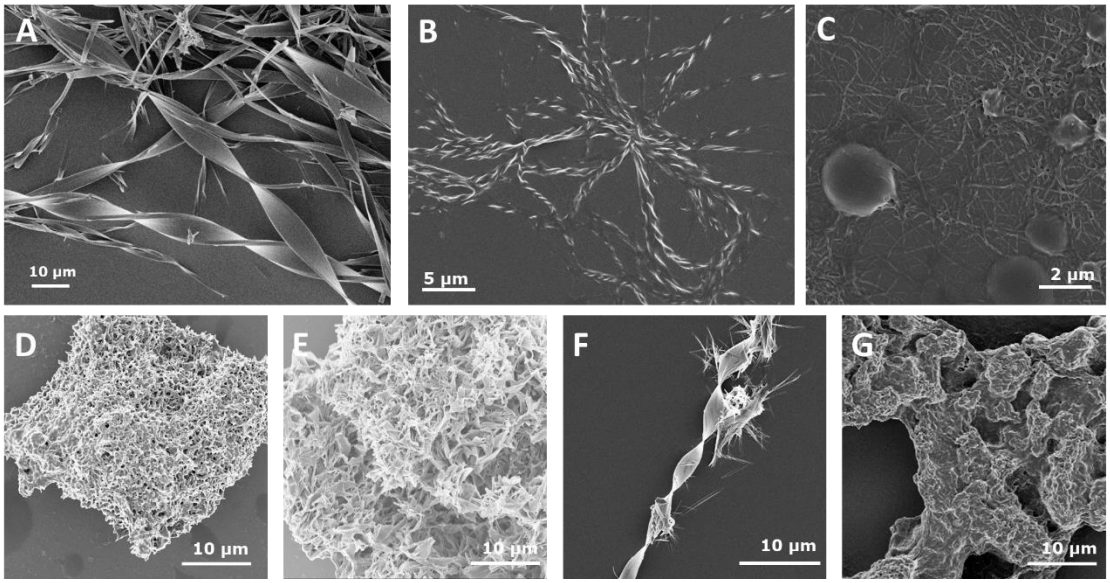

Figure 3-26. SEM images of the co-assembly between **13-D** and **23** (A), **24** (B), **25** (C), **26** (D), **27** (E), **28** (F), and **29** (G) in 1:1 mass ratio.

Surprisingly, no crystallization was observed upon co-assembly of **13-D** and **25**, resulting in an interconnected colloidal network (**Figure 3-26C**, **3-27A**, and **3-28A**). This result prompted me to screen different mass ratios, revealing that, in the presence of a higher amount of **25**, colloidal particles could be generated. The colloidal solutions were stable for over 6 months. The 1:2 mass ratio generated highly homogeneous and stable spherical particles that could retain the spherical shape even upon drying (**Figure 3-27B**); in contrast, higher amounts of **25** decreased the particle stability, that merged upon drying (**Figure 3-27C**).

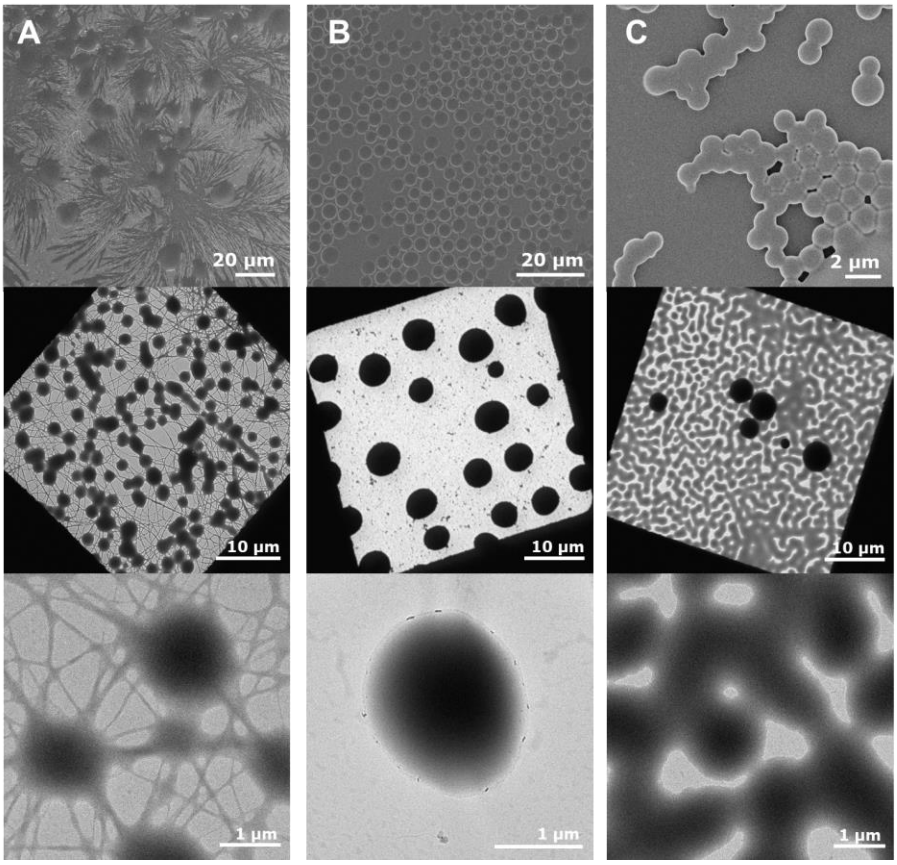

Figure 3-27. SEM (top) and TEM (middle and bottom) images of the co-assembly between **13-D** and **25** in 1:1 (A), 1:2 (B), and 1:4 (C) mass ratio.

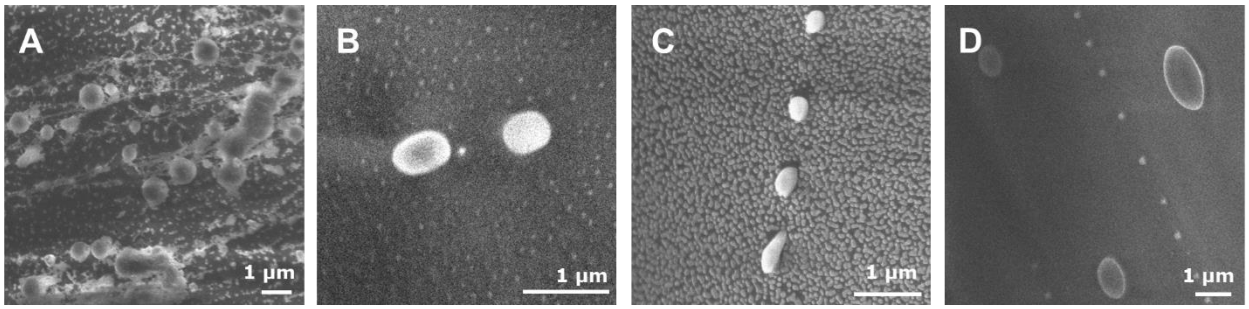

Figure 3-28. CyroSEM images of the co-assembly between **13-D** and **25** in 1:1 (A), 1:2 (B), and 1:4 (C) mass ratio, and the self-assembly of **25** (D).

3.3. Conclusion

In summary, I have established a model system to study carbohydrate materials based on a simple disaccharide. The strong intermolecular interactions and electron beam resistance of disaccharide **13-D** enabled the development of assays to study carbohydrate materials at the molecular level. A MicroED analysis based on a tilt-series ED acquisition was, for the first time, applied to an oligosaccharide system, permitting the reconstruction of the crystal unit of the assembled materials in their native state. This method

is key to the structural analysis of crystalline carbohydrate systems. Since most oligo- and polysaccharides crystallize into nano- to micrometer-sized crystallites, MicroED, optimized for electron sensitive materials, will be an important tool to understand the structural and conformational diversity of carbohydrates. Moreover, the local crystal organization can be correlated to the larger supramolecular architecture, offering insights into self-assembly.

The supramolecular fibers show a distinct helicity that can be correlated to the molecular level chirality, offering a new mode to tune the supramolecular structure. For instance, pitch and helicity can be modulated adjusting the assembly conditions or the chemical composition of the self-assembling solution. Helical structures (left or right handed) as well as flat lamellas can be obtained on demand. Similar synthetic approaches will help to correlate polysaccharide chirality and their assembly. To the best of our knowledge, this is the first observation of oligosaccharide molecular chirality governing supramolecular chirality.

Self-assembly can be performed in solution or on 2D surfaces, resulting in highly tunable and versatile materials. Two-dimensional spherulites can be generated from simple disaccharides under mild conditions to produce carbohydrate surfaces with tunable physical and mechanical properties.

Targeted chemical modifications permitted to identify key features responsible for the supramolecular assembly of compound **13-D**. Substitutions at the hydroxyl group at C-6 position are tolerated by the assembly process, offering an opportunity for further functionalization. In contrast, modifications at the aromatic groups or at the hydroxyl group at the C-3 position disrupted the assembly, as suggested by the molecular packing model. Co-assembly experiments supported the hypothesis that the introduction of irregularities during crystallization could tune the fiber helicity and pitch. Site-specific modifications of **13-D** generated novel geometries including hollow tubular structures, spherical colloidal particles, as well as highly twisted fibers/ribbons.

Electron tomography and electron diffraction enabled the characterization of the self-assembled structures with molecular level resolution. While these techniques are relatively underused for structural characterization of carbohydrates, apart from some examples in nanocellulose science[118], we demonstrated that ED-methods are powerful tools for investigating the correlation between molecular structure and nanoscale architecture of carbohydrates. The high-resolution view of the self-assembled structures offered by ED is hardly achievable with other methods.

3.4. Experimental section

3.4.1. Synthetic methods

The syntheses were performed by colleagues, G. Fittolani (**13-D**, **13-L**, **23**, **24**, **25**, **27**), Dr. Y. Yu (**24**, **26**, **29**), and Dr. Y. Zhu (**23**, **28**). The detailed methods can be found in the published work.[86b, 119]

3.4.2. Oligosaccharide self-assembly

a) Solvent-switch method (S): Stock solutions of the disaccharides (20, 40 and 100 mg mL^{-1}) in HFIP were diluted with water to reach a final concentration of 2 mg mL^{-1} with different ratio of water and HFIP. The temperature was controlled with an oil bath. When not mentioned, the conditions are 2 % HFIP in water (v/v) at room temperature. The samples were incubated for 3 days without agitation before the measurement.

Table 3-1. Summary of the samples prepared by the solvent-switch method (**S**).

Sample	Compound	HFIP content (%)	Temperature	Supramolecular morphology	Dimensions (Width/Length) (μm)
13-D (S)	**13-D**	2	75°C	Lamellae	0.5 ~ 10 / 100 ~ 800
			RT	Left handed helical fibers	0.01 ~ 1.0 / 10 ~ 50
			5°C		0.01 ~ 0.7 / 5 ~ 25
13-D (S-5%)		5	RT		0.01 ~ 2.0 / 10 ~ 100
13-D (S-10 %)		10			0.01 ~ 5.0 / 10 ~ 200
13-L (S)	**13-L**	2		Right handed Helical fibers	0.01 ~ 2.0 / 5 ~ 40
13-L (S-5 %)		5			0.01 ~ 5.0 / 10 ~ 100
13-L (S-10 %)		10			0.1 ~ 5.0 / 10 ~ 200
13-DL(S)	**13-D**:**13-L** = 1:1	2		Lamellae	15 ~ 20 / 100 ~ 200
	13-D:**13-L** = 1:2				0.1 ~ 20 / 2 ~ 50
	13-D:**13-L** = 2:1				0.1 ~ 15 / 1 ~ 50
23(S)	**23**			Flat fibers	0.01~ 1.0 / 5 ~ 200
24(S)	**24**			Left handed helical fibers	0.01 ~ 0.1 / 0.1 ~ 5
25(S)	**25**			Colloidal spheres	0.01 ~ 5
26(S)	**26**			Random aggregation	-
27 (S)	**27**				
28(S)	**28**				
29(S)	**29**				

b) Film-rehydration method (FR): 2 µL of the disaccharide solution in HFIP (1, 10 and 100 mg mL^{-1}) were drop casted and dried on the substrate for 12 h. The dried film was transferred into a humidity chamber and observed at different time scales. When not mentioned, the concentration is 100 mg mL^{-1}.

Table 3-2. Summary of the samples prepared by the film-rehydration method (**FR**).

Sample	Compound	Concentration (mg mL^{-1})	Temperature
13-D(FR-1)	**13-D**	1	RT
13-D(FR-10)		10	
13-D(FR)		100	
13-L(FR)	**13-L**		
13-DL(FR)	**13-D**:**13-L** = 1:1		
23(FR)	**23**	100	

4. A model system to study carbohydrate-peptide interactions in bacterial biofilms

4.1. Introduction

In chapter 3, I showed that the co-assembly of different disaccharides altered their aggregation tendencies promoting different aggregation pathways. In Nature, multiple biomolecules interact with each other building complex hierarchical structures to endow specific structures and functions.[120] Yet, in most cases, these mechanisms remain elusive and difficult to reproduce.[121] Interesting examples of these natural assemblies are bacterial biofilms, nanocomposites of protein fibers and polysaccharides (**Figure 4-1A**).[122] Freely floating bacteria can attach to a surface of living and nonliving organisms and generate colonies embedded in extracellular matrices, termed biofilms.[123] For *E. coli* and *Salmonella*, two main components are constructing the bacterial communities: amyloidogenic proteins, known as curli fibers, and cellulose (**Figure 4-2A**).[124] In this chapter, I present a synthetic model to study the formation of bacterial biofilms and identify key features of the cellulose-protein interaction.

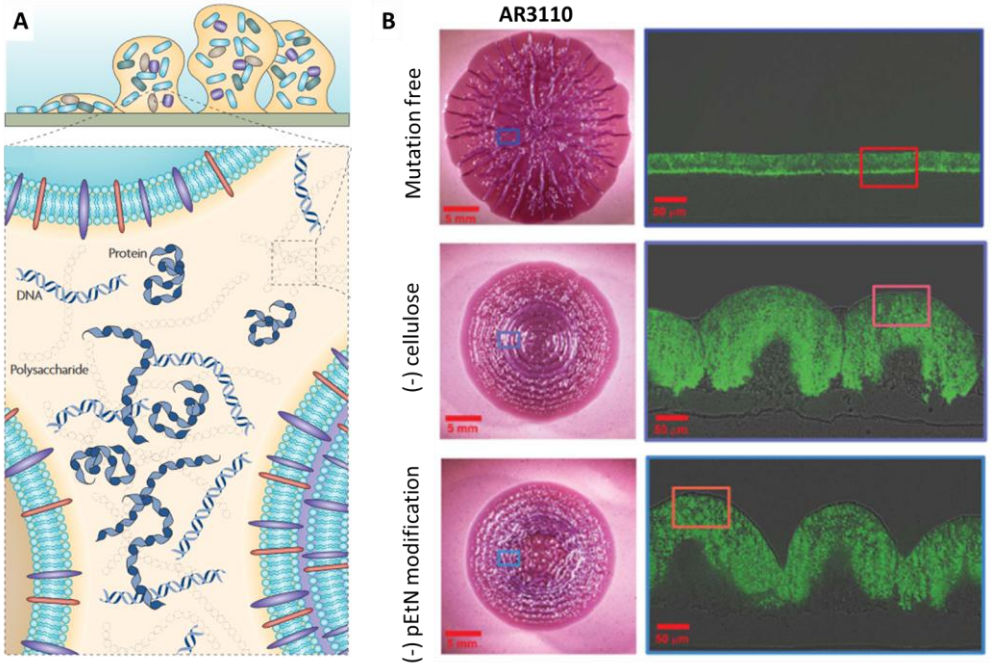

Figure 4-1. (A) Cartoon representation of bacterial biofilm and the major matrix components. (B) The microscopic matrix architecture of strain AR3110. Macrocolonies of *E. coli* strain AR3110 were stained either with Congo red (left, in a red color) and thioflavin S (right in a green color). Adapted with the permission from Flemming et al.[125] Copyright (2010) Springers Nature and Thongsomboon et al.[38] Copyright Copyright (2018) AAAS.

Cellulose is generally presented on the outer part of the bacterial biofilm, protecting cells from desiccation and environmental stresses.[126] In 2018, it was reported that *E. Coli* strain UTI89 are producing chemically modified cellulose, phosphoethanolamine (pEtN) cellulose, as part of their protective biofilm.[38] Genetic engineering approaches have been employed to investigate structural and functional roles of pEtN cellulose, suggesting its role in transforming the biofilm morphology and offering glue-like properties (**Figure 4-1B**). In the presence of pEtN cellulose, the macrocolony biofilm has a wrinkled phenotype along a radial direction with the cells weaved in intricate basket-like structures (**Figure 4-1B top**). Mutations to block the production of cellulose or the functionalization with pEtN resulted in ring-shape biofilms with a less densely connected network (**Figure 4-1B middle and bottom**).

This first example of naturally modified cellulose suggests that pEtN cellulose could become an important material for applications in tissue engineering and packing materials. Still, several aspects of this promising naturally modified material are still to be elucidated; the role of the modification, the pattern of modification, the interaction between curli fibrils and pEtN cellulose, and the tunability of the biofilm properties. Solid-state nuclear magnetic resonance (NMR) analysis revealed that the ratio of curli-to-pEtN cellulose varies in different *E. coli* strains.[127] A preliminary structural characterization of pEtN cellulose suggests that half of the glucose units of cellulose are substituted with the pEtN moiety at the C-6 hydroxyl group. More systematic studies are hampered by the complexity and heterogeneity of natural biofilms, requiring extremely challenging purification steps to isolate pure compounds required for structural characterization.

Here, I present a model system based on well-defined synthetic peptides and oligosaccharides to expand the knowledge on bacteria biofilm composites. **R5**, the most amyloidogenic subunit of the CsgA curli protein (**Figure 4-2B**), was chosen as a representative structure of the protein component.[128] Non-modified and pEtN-modified cellulose hexasaccharides with different amount and pattern of substitutions were synthesized with Automated Glycan Assembly (AGA) (**Figure 4-2C**). I used these components to generate artificial biofilms as a model to understand the effect of pEtN cellulose on amyloid fibrils formation, their morphology and their mechanical properties. The synthesis was carried out by T. Tyrikos-Ergas and J. Huang.

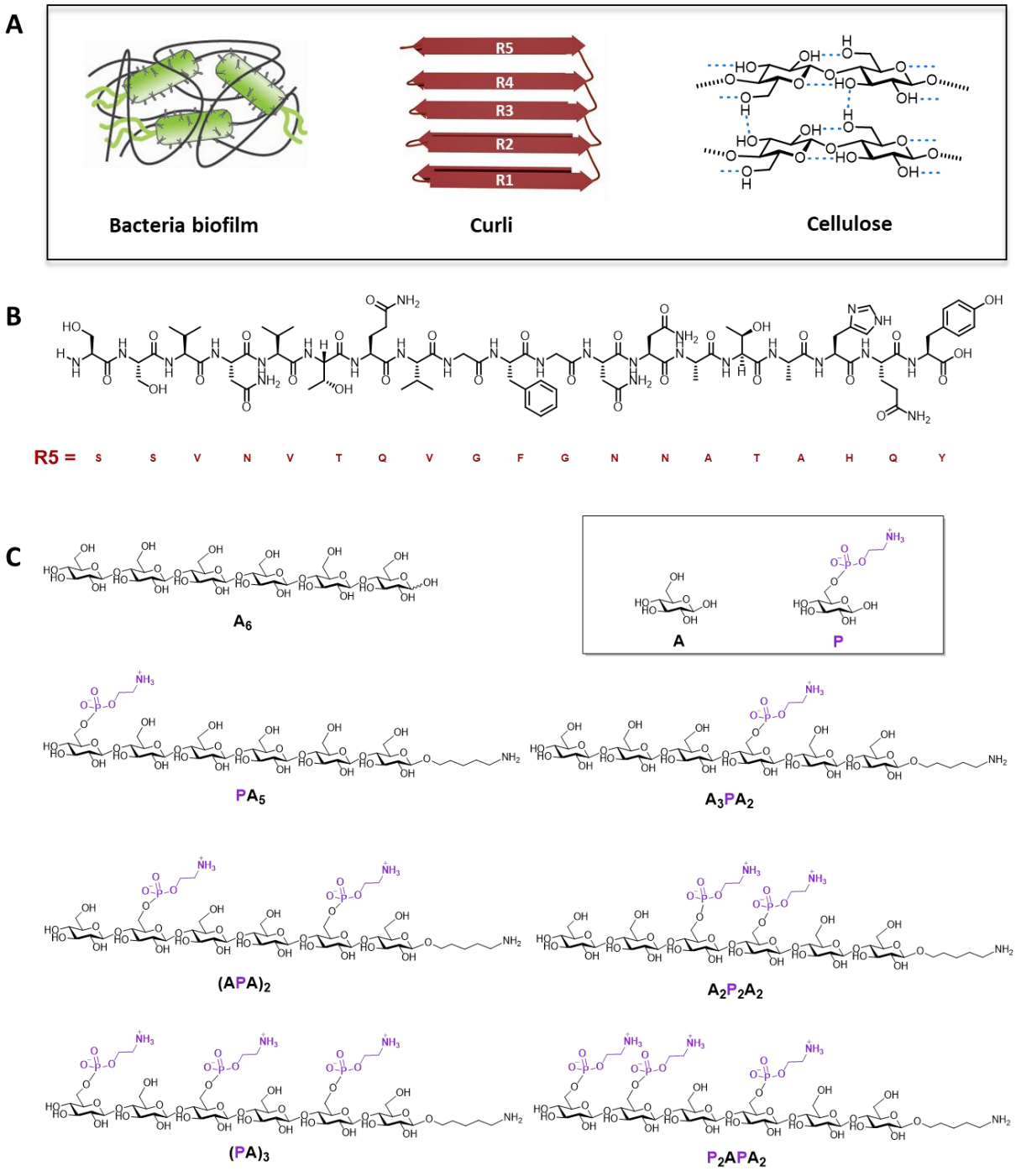

Figure 4-2. (A) Cartoon representation of bacterial biofilm and its major components, curli and cellulose. Synthetic representative sequence of the amyloidogenic peptide, **R5** (B) and hexasaccharides used in this study (C).

4.2. Results

4.2.1. Amyloid fibrils formation

Access to well-defined oligomers representative of the *E. coli* biofilm allowed me to assemble artificial matrices and explore the role of the carbohydrate component. Aiming to generate artificial curli fibers, **R5** was denatured upon addition of hexafluoroisopropanol (HFIP)[129] and the sample dried under nitrogen purging. Addition of water triggered a structural transition from alpha helix to the amyloidogenic beta-sheet conformation, confirmed by circular dichroism (CD) spectroscopy (**Figure 4-3**). The transition was completed within 20 minutes (**Figure 4-4A**). Microscopic analysis (AFM, TEM, and SEM, **Figure 4-5A**) was performed after one or five days incubation, showing the presence of ill-defined aggregates with no fibril-like structure, as reported previously.[130]

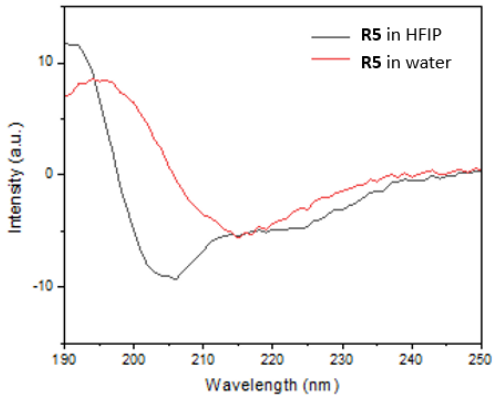

Figure 4-3. CD spectra of **R5** in HFIP (black) adopting an alpha-helical structure and in water (red) adopting a beta-sheet structure (25 µM, 23 °C).

I then repeated the same process in the presence of the selected oligosaccharide using a **R5**:oligosaccharide mass ratio of 6:1 that should best resemble the biofilm produced by the *E. coli* strain UTI89.[38] In all cases, the secondary structure transition to the beta-sheet conformation required longer times (**Figure 4-4(B-H)**). The presence of the beta-sheet motif was further confirmed by the ThT binding test (**Figure 4-6**).[131] Microscopy analysis showed that the **R5** sample containing the cellulose oligomer $\mathbf{A_6}$ assembled into thin fibrils (**Figure 4-5B (left)**, Day 1) that developed into a fibrous network within five days (**Figure 4-5B (right)**, Day 5). Interestingly, control experiments using the simple glucose monosaccharide did not result in fiber formation (**Figure 4-14** and **4-6**). Next, I examined the effect of the six pEtN-cellulose hexamers on the assembly of **R5**. CD analysis indicated the different pEtN content had an effect on the secondary structure transition rate, with the sample prepared in the presence of $\mathbf{(PA)_3}$ showing the slower transition (> 6 h) into the beta-sheet conformation (**Figure 4-4G**). All samples generated fibrils, yet with different growth rate and morphology (**Figure 4-4(C-H)** and **4-5(C-H)**). While the sample containing the three-substituted oligomers $\mathbf{(PA)_3}$ and $\mathbf{P_2APA_2}$ showed long and defined fibrils already at Day 1 (**Figure 4-**

5G·H (left)), the less substituted analogues showed shortened aggregates (**Figure 4-5(C-F) (left)**). Interestingly, the fibers observed for **R5** and **$(PA)_3$** showed the classical curled shape responsible for the name of the natural analogue.[132] At Day 5 all samples resulted in homogeneous fibrous networks (**Figure 4-5(C-H) (right)**). ThT binding studies showed a lower emission intensity for the samples containing cellulose with a crowded pEtN distribution (e.g. **P_2APA_2**) as compared to evenly distributed hexasaccharides (e.g. **$(PA)_3$**) (**Figure 4-6**). This result might indicate a lower amount of amyloid fibers in the samples containing unevenly substituted oligosaccharides. Controlled studies confirmed that the unnatural aminopentyl linker present at the reducing end of the pEtN-modified oligosaccharides (installed for synthetic reasons), has negligible effect on the aggregation tendency, as proven by the comparison between **A_6** and **A_6-NH_2** (**Figure 4-4B, 4-5B,** and **4-15**).

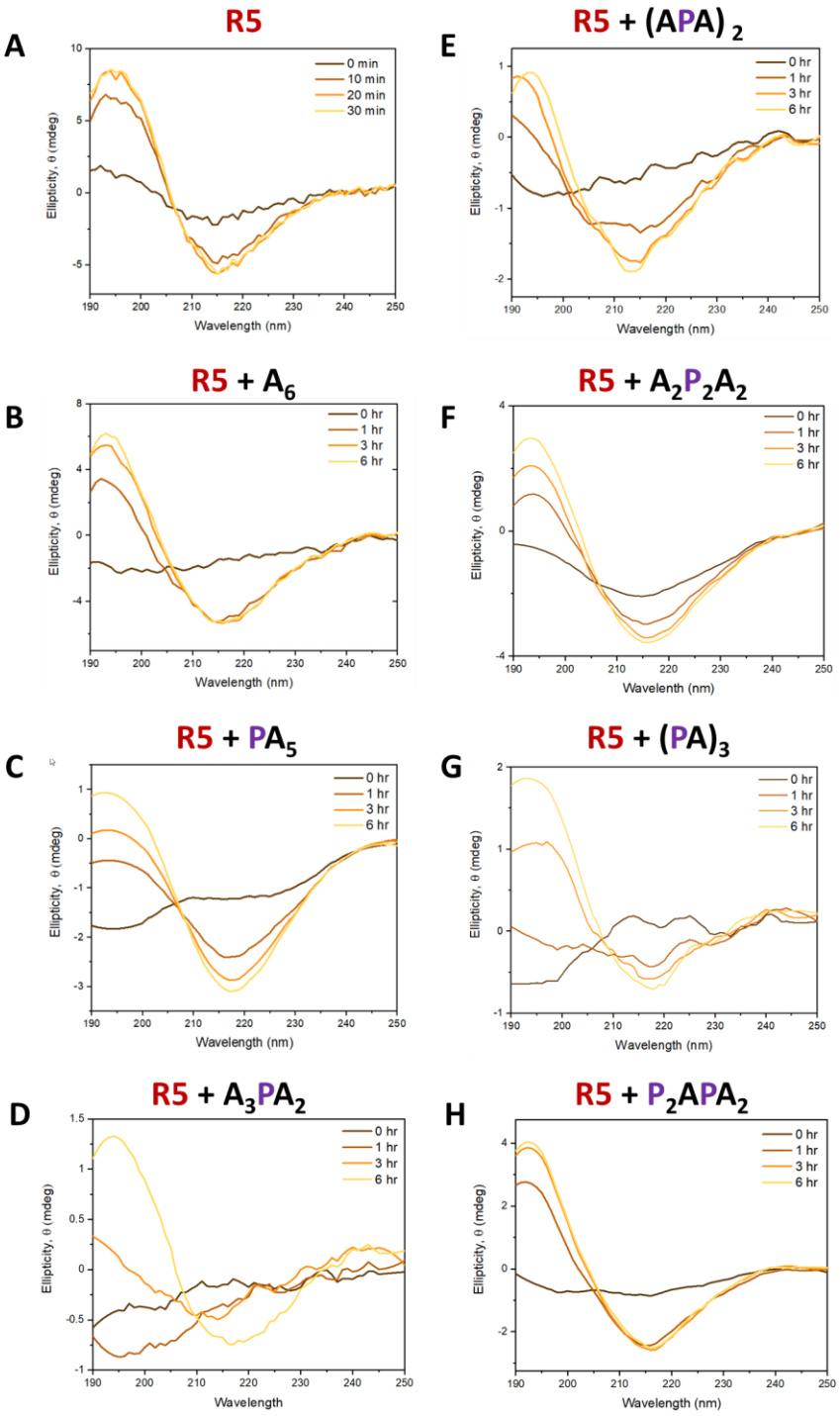

Figure 4-4. CD spectra of the peptide, **R5** showing the secondary structure transition to beta-sheet upon addition of water in the presence of different hexasaccharides (25 µM, 23 °C).

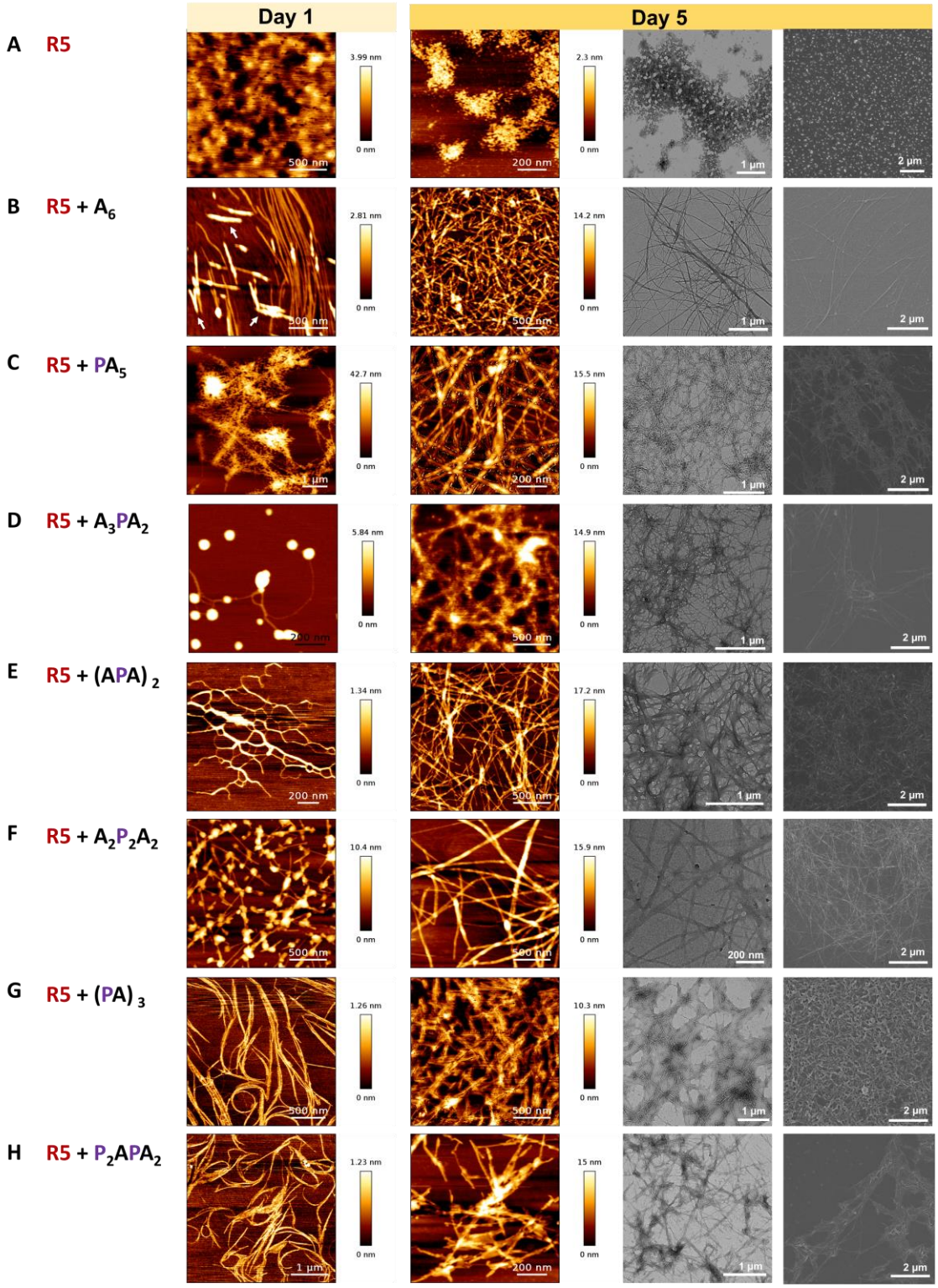

Figure 4-5. AFM (first and second column at Day 1 and Day 5, respectively), TEM (third column, Day 5), and SEM (fourth column, Day 5) images of the artificial amyloid fibrils generated from the aggregation of **R5** (A) and **R5** in the presence of different hexasaccharides (B-H). The parts of the sample highlighted with white arrows in Figure 4-5B (first column) indicate the aggregation of $\mathbf{A_6}$ alone.

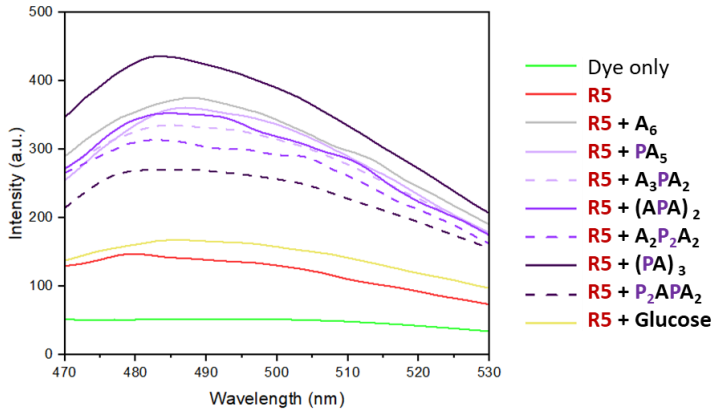

Figure 4-6. ThT emission spectra to test the presence of amyloid fibers in the **R5** samples incubated for 5 days with/without different hexasaccharides, showing maxima at around 482 nm.[133] Glucose is reported as control.

The modularity of our approach permitted us to explore different peptide:carbohydrate ratios to better mimic other bacteria strains. For example, the AR3110 strain produces a biofilm with a much higher content of pEtN cellulose (3:1 by mass).[127] No drastic differences were observed in the fiber morphology, however the fibrils obtained starting with a 3:1 ratio of **R5** and **$(PA)_3$** or **P_2APA_2** were embedded in a much larger amount of matrix (**Figure 4-7**). This observation suggests that the pEtN-modified cellulose forms the network that connects the fibers.

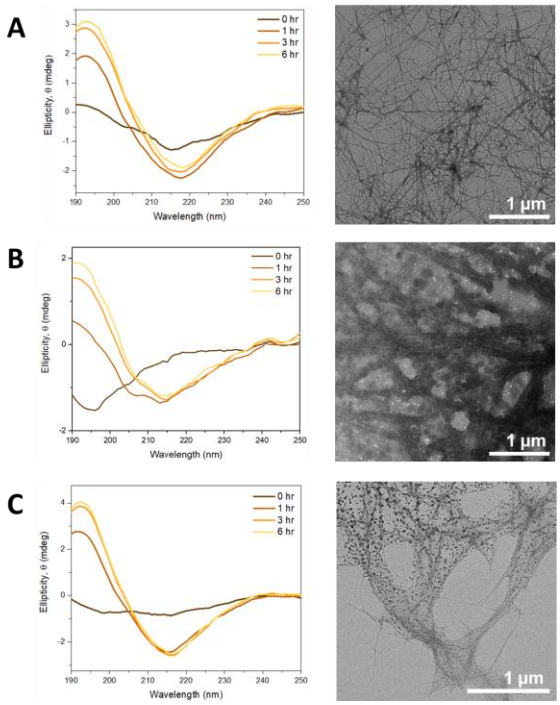

Figure 4-7. CD spectra (left) and TEM images (right) of the aggregation of **R5** in the presence of **A_6** (A), **$(PA)_3$** (B), and **P_2APA_2** (C) with a 3 to 1 ratio by mass at Day 5.

The fibres obtained from the **R5** sample in the presence of either $\mathbf{A_6}$ or the pEtN-analogues $\mathbf{(PA)_3}$ or $\mathbf{P_2APA_2}$ showed a similar z-height of around 0.8 nm (**Figure 4-8**), hinting that the fibrils are built on the same peptidic core. The sample containing **R5** and $\mathbf{A_6}$ showed "naked" fibers together with aggregates identified as self-sorted $\mathbf{A_6}$ clusters with a height of around 4 nm (**Figure 4-7B (left)** and **4-15C (left)**, indicated with white arrows and corresponding to **Figure 4-9**). In contrast, the fibers generated from the sample containing **R5** and $\mathbf{(PA)_3}$ or $\mathbf{P_2APA_2}$ were embedded in a fibrous matrix (**Figure 4-8B·C**, highlighted with white arrows). Non-stained TEM images confirmed the presence of a matrix surrounding the fibrils, making the fibers brighter than the surrounding (**Figure 4-5G·H**).[134]

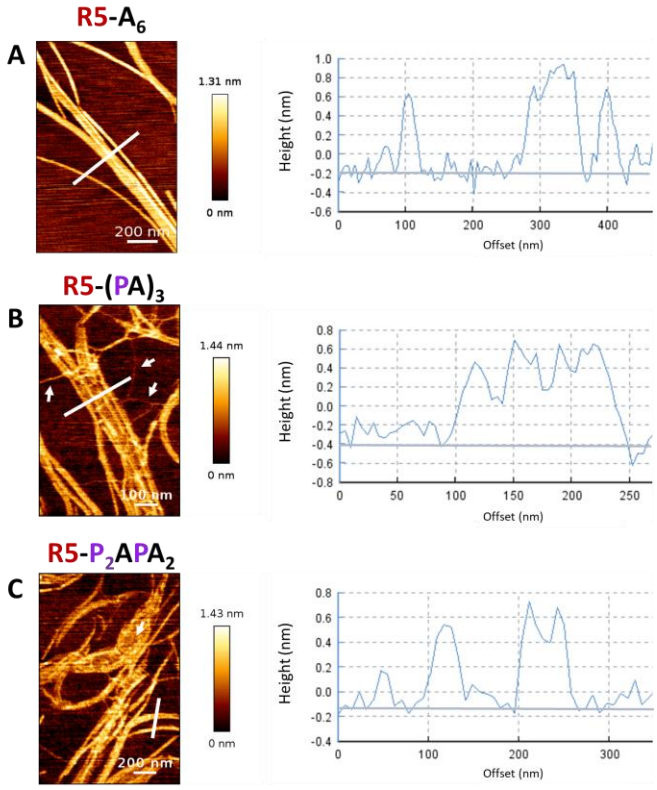

Figure 4-8. AFM Images (left) and cross-sectional analysis (right) of fibrils of **R5** with $\mathbf{A_6}$ (A) and $\mathbf{(PA)_3}$ (B) at Day 1, showing similar z-height dimensions. While the sample containing **R5** and $\mathbf{A_6}$ (A) showed bare fibers and clear background, the filaments obtained from the samples containing **R5** and $\mathbf{(PA)_3}$ (B) or $\mathbf{P_2APA_2}$ (C) were surrounded by a fibrous matrix (highlighted with white arrows).

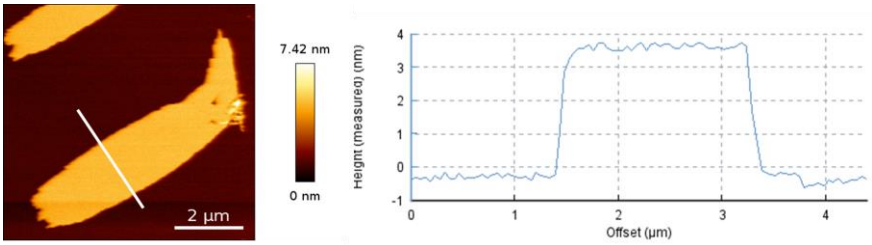

Figure 4-9. AFM Image and cross-sectional analysis of aggregates of $\mathbf{A_6}$ in the absence of **R5**.

4.2.2. Mechanical property analysis of the artificial biofilm

The artificial fibers were employed to generate artificial biofilms with a thickness of around 300 nm and explore their mechanical properties via AFM force-distance curve analysis (**Figure 4-10** and **4-16**, and **Table 4-1**). AFM nanoindentation indicated a stiffness of around 12 MPa for all matrices. This data supports the hypothesis that the peptide fibres are the major structural component of the artificial biofilm. The presence of the pEtN-modified oligosaccharides dramatically enhanced adhesion. The adhesion force for the sample containing **R5** and **$(PA)_3$** was around 130 nN, six times higher than the value obtained for the sample containing **R5** and **A_6**. No direct correlation between the number of pEtN groups and the adhesion was found. The highest values were measured for compounds with the pEtN moiety at the sugar non-reducing end (i.e. **$(PA)_3$ and PA_5**). In contrast, crowded distributions of pEtN substituents (e.g. **$A_2P_2A_2$**) resulted in much lower adhesion forces, underscoring the importance of the substitution pattern in determining the mechanical properties of the biofilm.

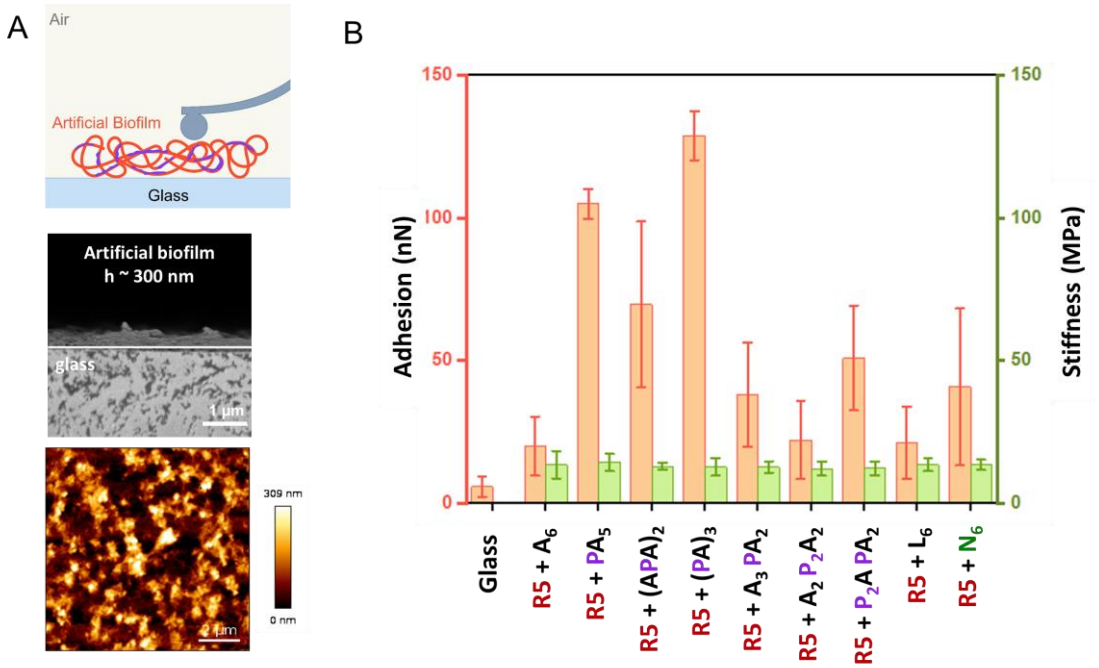

Figure 4-10. (A) Schematic illustration of the adhesion measurement (top). A cross-sectional SEM (middle) and AFM (bottom) image of the artificial biofilm of **R5** with **$(PA)_3$**. (B) Adhesion and stiffness measured for the artificial biofilms prepared from **R5** and different oligosaccharides.

4.2.3. Tuning the artificial biofilm with artificial oligosaccharides

The discovery of the naturally modified pEtN-cellulose opened up opportunities to generate tuneable materials on engineering of the carbohydrate components. It has been previously shown that carbohydrates can modulate the formation of neurotoxic amyloidogenic fibrils, with chitosan oligosaccharides inhibiting aggregation[135] and heparan sulfate oligomers promoting fiber formation[136]. To explore the possibility of tuning the morphologies and properties of bacterial biofilms, oligosaccharides not present in natural bacterial biofilms were screened (**Figure 4-11** and **4-12**). The same aggregation tendency was observed for the **R5** sample treated either with $\mathbf{A_6}$ or with its enantiomer $\mathbf{L_6}$ (**Figure 4-11A** and **4-12A**), excluding a chiral-driven interaction between the peptide and the carbohydrate components. A completely different outcome was obtained when **R5** was treated with the *N*-acetyl glucosamine hexasaccharide analogue $\mathbf{N_6}$. The much faster secondary structure transition, completed in less than 1 h (**Figure 4-11B**), generated short fibrils with length < 1 µm that further aggregated into supramolecular bundles (**Figure 4-12B**). The presence of the negatively charged sulfated hexasaccharide $\mathbf{(SA)_3}$ interrupted the **R5** transition into the beta-sheet conformation (**Figure 4-11C** and **4-17A**) and postponed the formation of fibrils (**Figure 4-12C**). The fibrils tended to be entangled and developed into bulky agglomerates (**Figure 4-17B** and **4-18B**), preventing the formation of a uniform film.

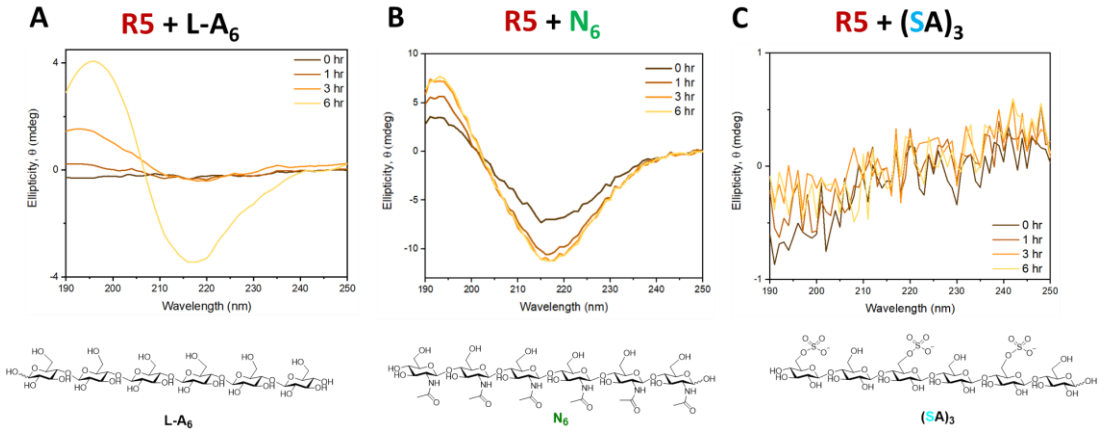

Figure 4-11. Chemical structure of oligosaccharides and CD spectra of the peptide, **R5** with/without different hexasaccharides showing the secondary structure transition of **R5** upon addition of water on the peptide (and oligosaccharides)/HFIP film.

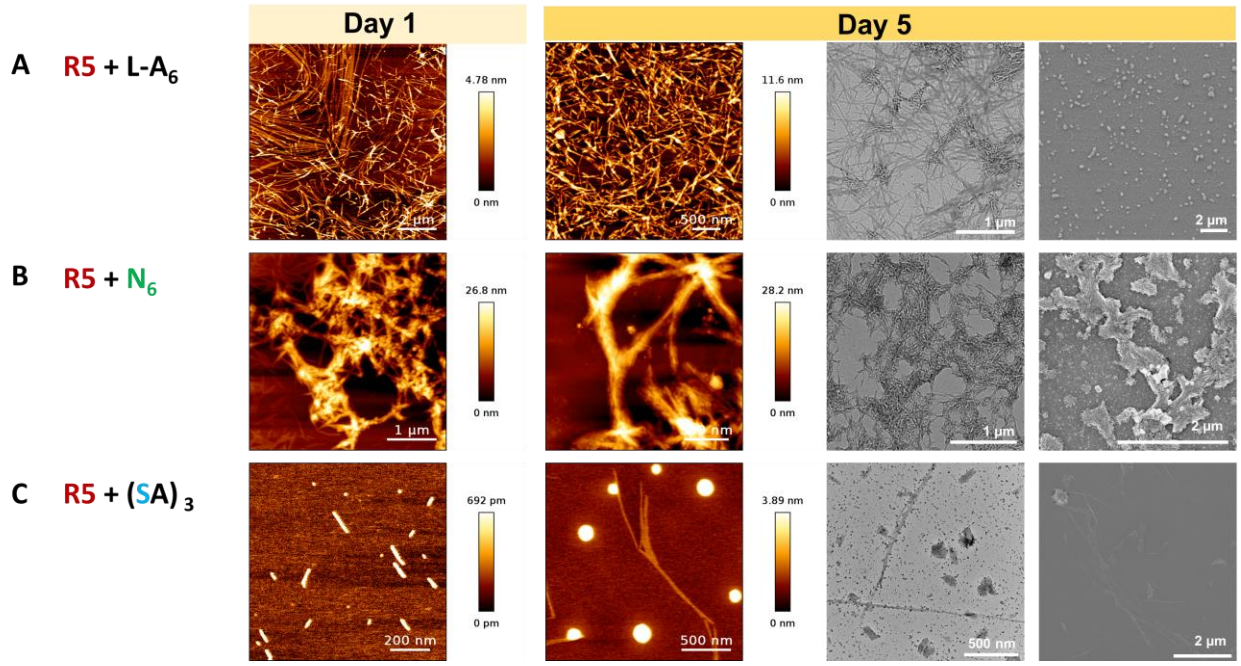

Figure 4-12. AFM (first and second column at Day 1 and Day 5, respectively), TEM (third column, Day 5), and SEM (fourth column, Day 5) images of the artificial amyloid fibrils generated from the aggregation of **R5** in the presence of different unnatural hexasaccharides.

4.3. Conclusion

A model system was designed to explore the role of carbohydrates in bacterial biofilms and the protein-carbohydrate interactions occurring during amyloid fibrils formation. Synthetic peptides and oligosaccharides were prepared to mimic the natural components of bacteria biofilms (i.e. curli fibers and pEtN-modified cellulose). The model system offers a complementary approach to genetic engineering, providing a much higher control on the chemical structure of the individual components. Precise control over the substitution amount and pattern lead to the alteration of fiber growth rate and aggregation tendency. The presence of oligosaccharides slowed down the secondary structure transition of the amyloidogenic peptide, **R5**, inducing the growth of fibrous structures. Different results were obtained from oligosaccharides with different pEtN substitution patterns. The artificial biofilms generated from synthetic oligosaccharides improved our understanding of the natural counterpart and offers an interesting alternative for the production of synthetic extracellular matrices for tissue engineering. The ability to inhibit amyloid formation of the sulfated hexasaccharide, **(SA)$_3$**, suggests the potential application of this compound as a drug candidate for the treatment of neurological diseases or as antibacterial agent.

4.4. Experimental section

4.4.1. Synthetic methods

The synthesis of the peptide and all the oligosaccharides was performed by T. Tyrikos-Ergas and J. Huang.

4.4.2. Sample preparation method

The fibril structures were generated following a modified procedure previously reported for the preparation of aggregate-free amyloid beta peptide of Alzheimer's disease (**Figure 4-13**).[137] Stock solutions of the peptide and the selected oligosaccharide were dissolved in hexafluoroisopropanol (HFIP) with the concentration of 200 μM (0.4 mg mL^{-1}) and 0.13 mg mL^{-1}, respectively. The peptide and oligosaccharides stock solutions were mixed with 2 to 1 (or 1 to 1) volume ratio to reach the final mass ratio of 6 to 1 (or 3 to 1), and sonicated. HFIP was removed under gentle nitrogen purging to generate a thin film. Water was added to the film to reach the final peptide concentration of 25 μM for imaging, CD, ThT binding test, and AFM force measurement. If not mentioned, the standard ratio between the peptide and oligosaccharides is 6 to 1 by mass.

Figure 4-13. Cartoon representation of the sample preparation method.

4.4.3. Mechanical property analysis methods via AFM

The AFM samples for the imaging of single protofilaments and matured fibrils were prepared on freshly cleaved mica. Qualitative imaging (QI) mode was applied for nanoindentation and adhesion force measurement with a silicon cantilever. For the analysis of the mechanical property, uniform films with a thickness of 300 nm were prepared on a pre-washed glass substrate. The nanoindentation was conducted with a silicon nitride cantilever at a constant force of 10 nN. The approaching force-distance curves were fit to the Hertz model and manipulated to obtain Young's modulus. For the adhesion measurement, a tipless cantilever was modified with a polystyrene bead (radius, 8 μm). 10 x 10 curves were obtained from one spot. At least ten spots per sample and three samples were tested for each oligosaccharides. The JPK data processing software was used to analyze all AFM data, including images and forces.

4.5. Supporting information

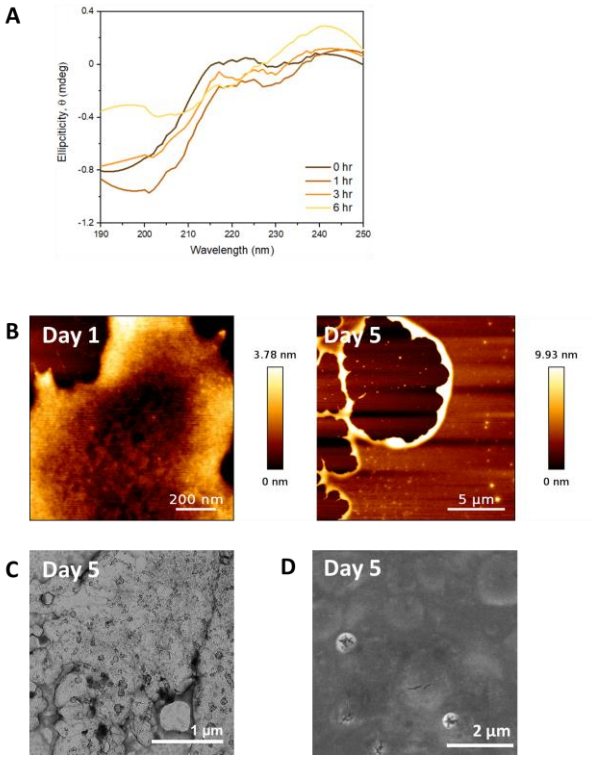

Figure 4-14. Structural transition of **R5** in the presence of glucose observed via (A) CD spectroscopy and (B) AFM, (C) TEM, and (D) SEM microscopy.

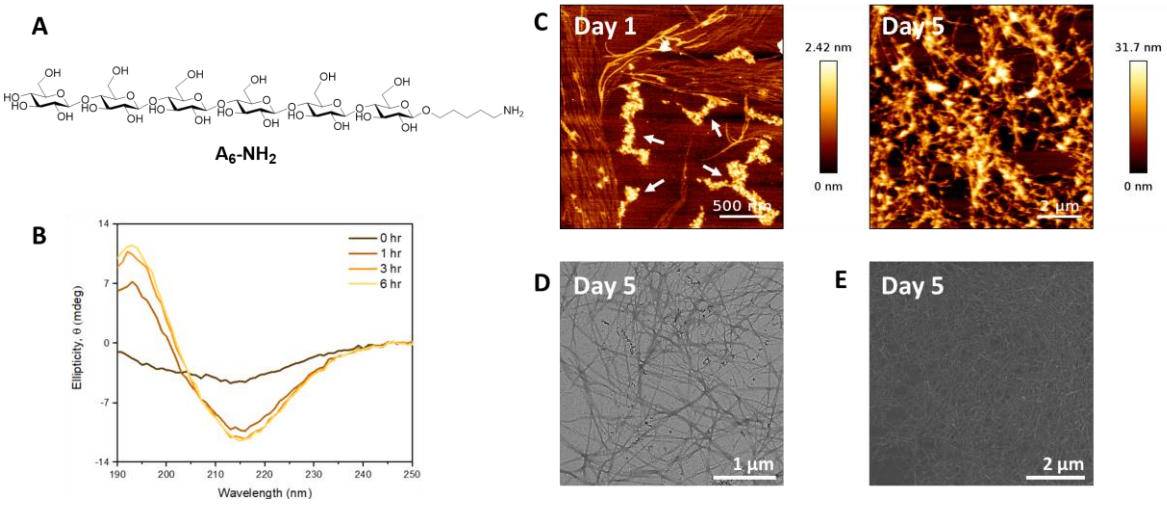

Figure 4-15. (A) Chemical structure of **A_6-NH_2**. Structural transition of **R5** in the presence of **A_6-NH_2** observed via (B) CD spectroscopy and (C) AFM, (D) TEM, and (E) SEM microscopy. The parts of the sample highlighted with white arrows in Figure 4-15C (left) indicate the aggregation of **A_6-NH_2**.

Table 4-1. Mean Young's modulus and adhesive forces and corresponding standard deviations (SD) for the artificial biofilms.

Sample	Stiffness (MPa)	Adhesion (nN)
Glass only	-	5.89 ± 3.59
R5 + A_6	13.46 ± 4.81	20.06 ± 10.37
R5 + PA_5	14.30 ± 3.01	105.0 ± 5.10
R5 + A_3PA_2	12.69 ± 1.99	38.13 ± 18.39
R5 + $(APA)_2$	12.83 ± 1.22	69.73 ± 29.11
R5 + $A_2P_2A_2$	12.09 ± 2.44	22.24 ± 13.71
R5 + $(PA)_3$	12.69 ± 3.11	128.9 ± 8.57
R5 + P_2APA_2	12.24 ± 2.41	50.95 ± 18.47
R5 + L-A_6	13.47 ± 2.26	21.28 ± 12.79
R5 + N_6	13.44 ± 1.79	40.80 ± 27.50

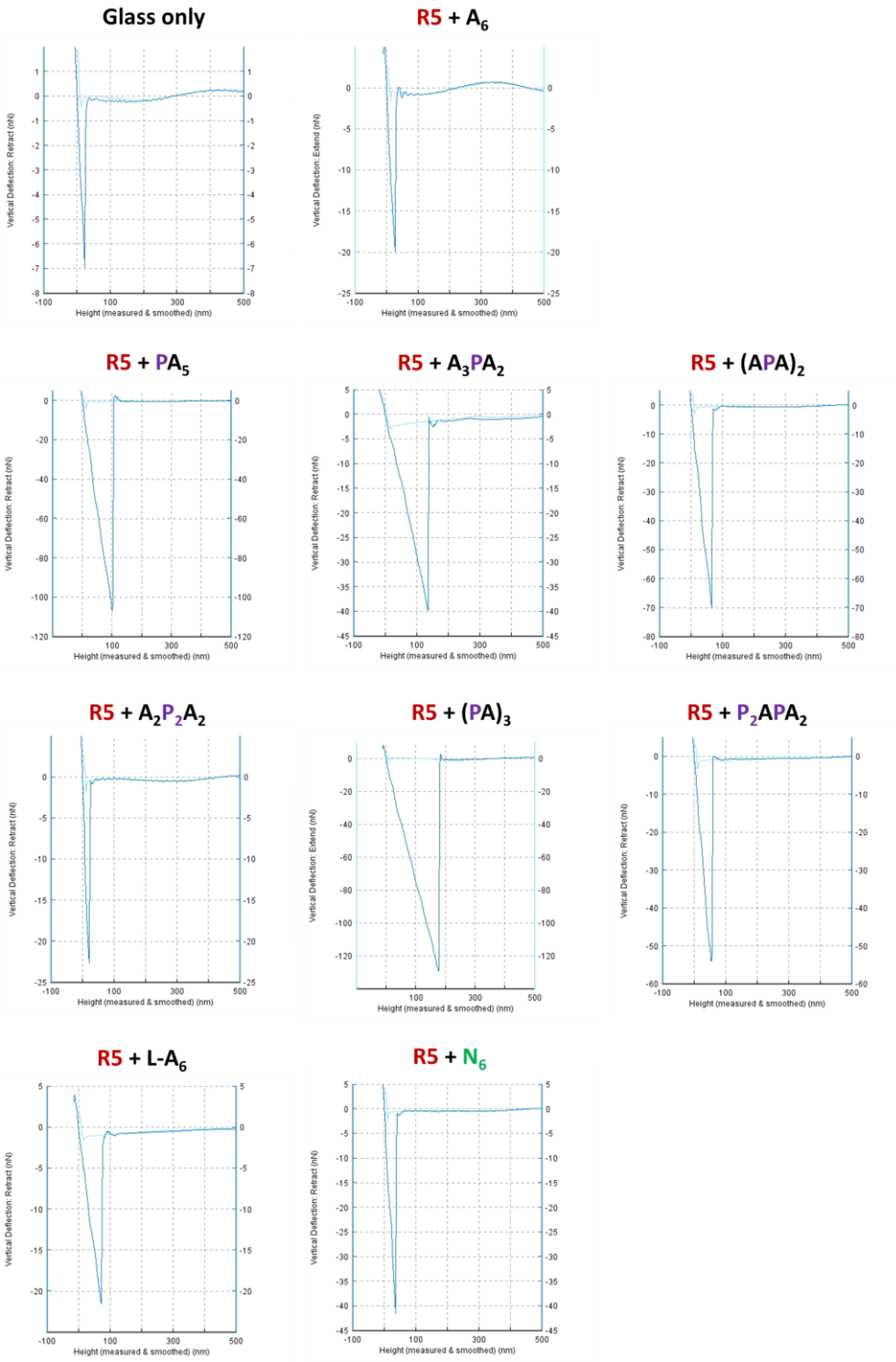

Figure 4-16. Representative force-distance curves to obtain the adhesion forces for the artificial biofilms.

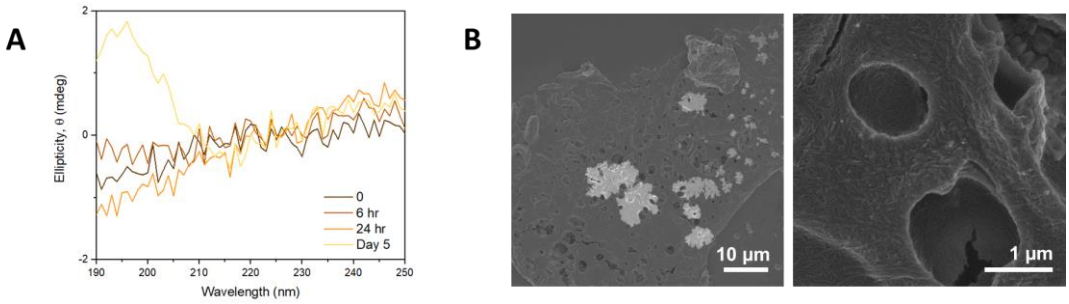

Figure 4-17. CD spectra (A) and SEM images (B) of **R5** in the presence of **$(SA)_3$** at Day 5. CD shows a much slower transition to the beta-sheet conformation and SEM shows the presence of bulky fibrous aggregates instead of a uniform and thin film.

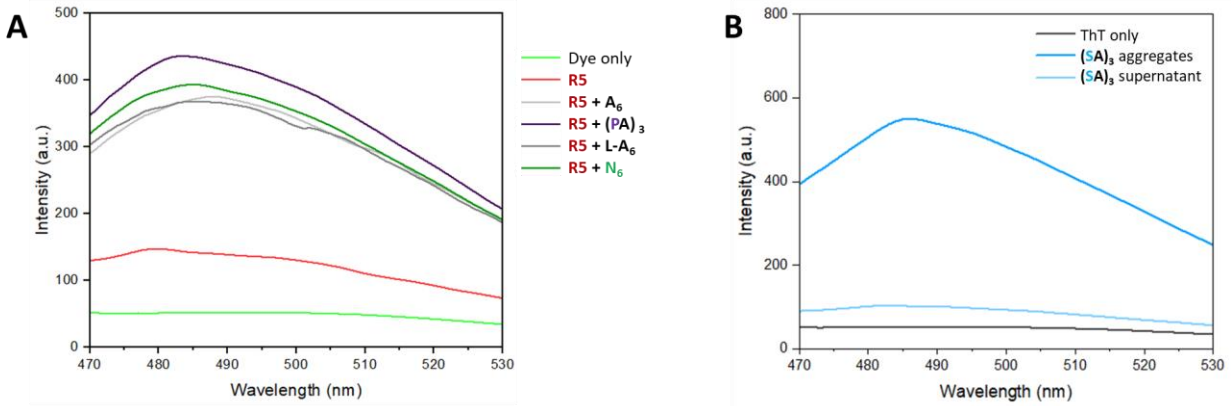

Figure 4-18. ThT emission spectra to test the presence of amyloid fibers in the **R5** samples incubated for 5 days with/without different hexasaccharides (A), showing maxima at around 482 nm.[133] The result from **$(SA)_3$** (B) showed large variations due to the presence of large aggregates (see Figure 4-17).

5. Conclusion and outlook

In this dissertation, synthetic oligosaccharides were identified as a model system to study carbohydrate supramolecular assemblies. Diverse architectures were generated, triggered by different self-assembly methods (**Figure 5-1**, left). Several analytical techniques, optimized for oligosaccharides, revealed the molecular packing and key interactions responsible for the aggregation: H-bonding as well as aromatic interactions stabilized the assembly. For the first time, a direct correlation between the molecular chirality and supramolecular chirality of carbohydrate assemblies was described. Co-assemblies of different disaccharides either disrupted the formation of well-defined structures or tuned the microstructures, permitting to generate hollow tubes or highly helical ribbons. Some disaccharides showed intrinsic optical properties, including a broad emission spectrum in the entire visible light range. I expect that these materials with unique morphologies and optical properties can find use in biomedical applications, like drug delivery and bioimaging. The analytical techniques, optimized within these theses, will permit the exploration of natural polysaccharides, allowing for structure-property correlations.

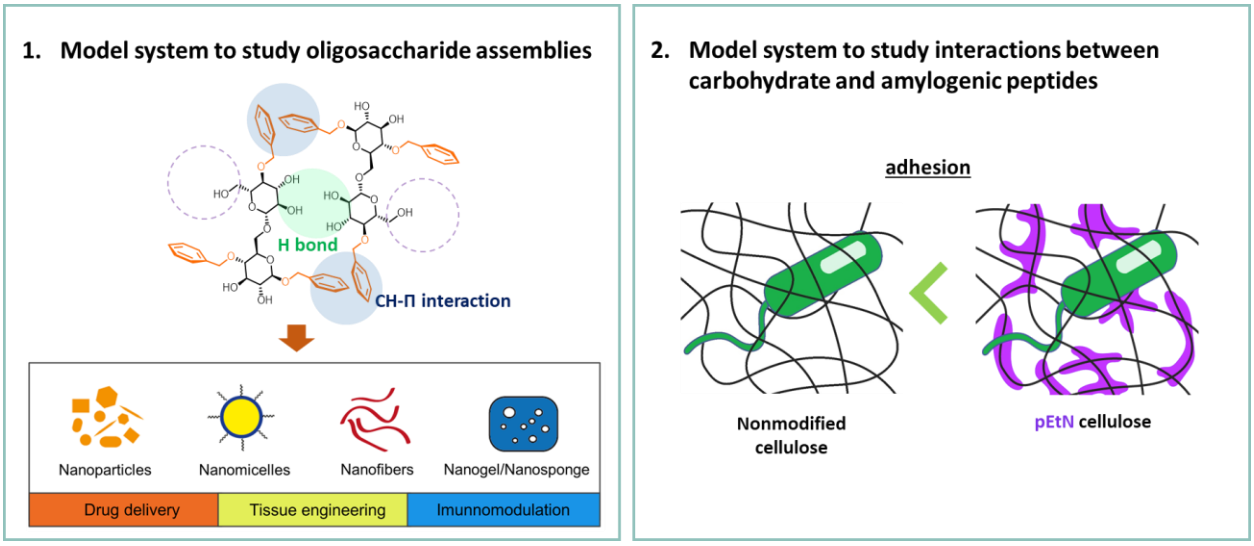

Figure 5-1. Summary of the dissertation.

Natural bacterial biofilms were described using synthetic peptides and oligosaccharides to unveil the interactions between these two biomolecules. Particular focus was given to how carbohydrates (i.e. pEtN-modified cellulose oligomers) altered the mechanical properties of bacterial biofilms (**Figure 5-1**, right). It was discovered that the growth rate of curli fibrils and the morphology of the peptide-oligosaccharide network are dependent on the oligosaccharide substitution. The evenly substituted cellulose analogous, **$(PA)_3$**, coated the long curli fibrils, endowing enhanced adhesive properties. Insights into the molecular level interactions are still missing. In order to study intermolecular interactions, NMR analysis and molecular modelling are currently being implemented (**Figure 5-2**).

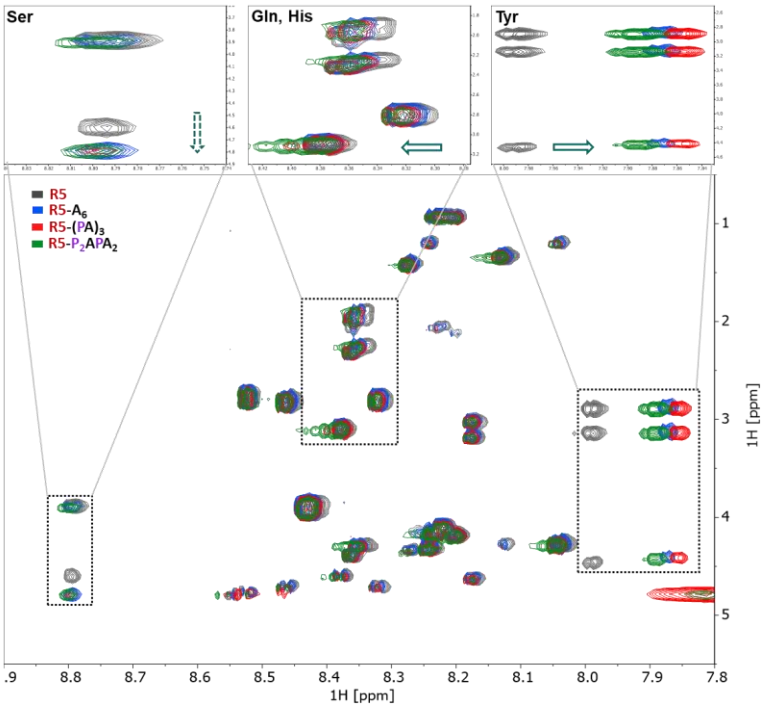

Figure 5-2. Overlay of a selected region of the ^{1}H-^{1}H TOCSY spectra for the samples containing **R5** alone (grey) and in the presence of $\mathbf{A_6}$ (blue), $\mathbf{(PA)_3}$ (red) and $\mathbf{P_2APA_2}$ (green). The four amide protons involved in the interaction are highlighted (top panels).

The simple model systems presented in the dissertation shined light over some aspects of carbohydrate-carbohydrate and carbohydrate-peptide interactions. Similar approaches can be envisioned to describe more complex systems where carbohydrates play crucial roles.

Natural carbohydrate materials (e.g. cellulose nanocrystals or nanofibers) are becoming an emerging class of materials with applications as emulsifiers, adhesives, devices, and biosensors.[138] Yet the molecular level characterization of these compounds is still missing due to lack of analytical techniques suitable to the study of carbohydrates. I showed that electron diffraction and tomography can generate valuable information on the aggregation of a model disaccharide system. A similar approach could be translated to natural carbohydrates to reveal important details of their molecular conformation and packing in a non-destructive way. For example, cellulose nanocrystals (CNCs) are generally extracted from natural sources following top-down approaches. These methods generate non-uniform materials with broad variation depending on the cellulose sources and cleavage methods, hampering their molecular level description. Recently, our group was able to produce cellulose nanocrystals starting from well-defined cellulose hexasaccharides following a bottom-up approach (**Figure 5-3A**). The optimized microED method showed in chapter 3 may enable the analysis of the crystalline structure of these oligosaccharide assemblies, promoting a better understanding of naturally sourced CNCs (**Figure 5-3B**·**C**). In the future, this technique

could be adapted to other polysaccharides, such as chitin, opening new possibilities for the characterization of carbohydrate materials.

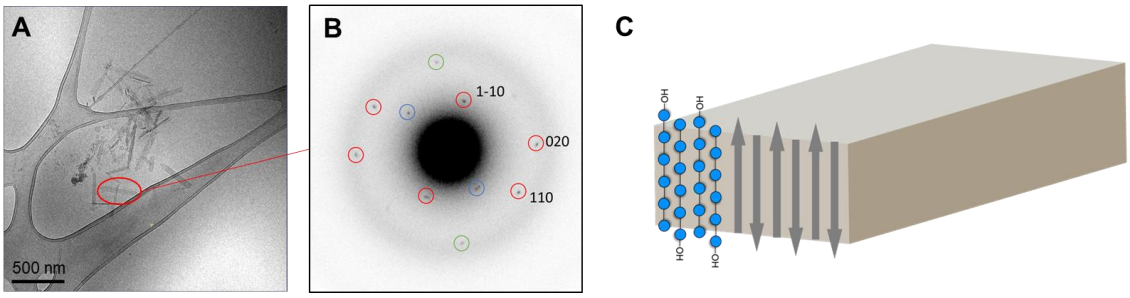

Figure 5-3. A TEM image (A) and electron diffraction pattern (B) of CNCs generated from cellulose hexasaccharides. (C) A tentative molecular description of the cellulose hexamers in the CNC. Each blue circle represents a glucose unit.

Synthetic peptides and oligosaccharides permitted the formation of tuneable matrices. Interestingly, the dimension and growth rate of the amyloid fibers could be regulated with different oligosaccharides not present in natural biofilms, such as chitin and sulfated hexasaccharides. Other types of oligosaccharides (e.g. positively charged chitosan or negatively charged alginate oligosaccharides) could be implemented to generate a toolbox of artificial matrices. The synthetic oligosaccharides could be applied to bacterial biofilms with living bacterial cells, enabling the production of tuneable biofilms with precise control on the composition and quantity of carbohydrates (**Figure 5-4**). This method could offer a valid alternative to genetic engineering approaches, to date, underdeveloped for carbohydrates.

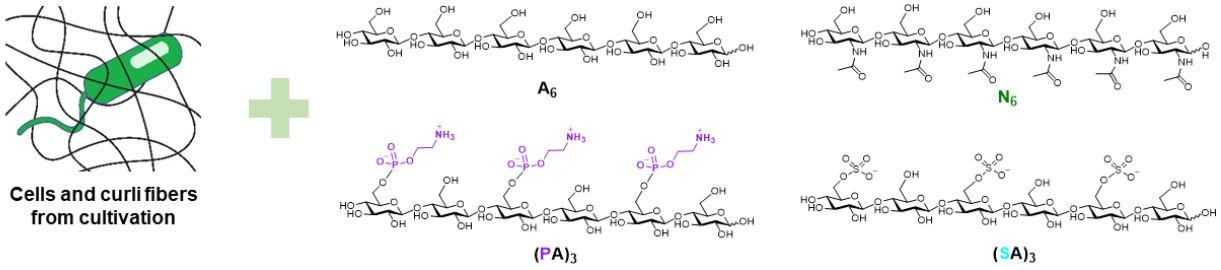

Figure 5-4. Schematic illustration of an approach to produce tunable biofilms using bacterial culture and synthetic oligosaccharides.

6. General methods

All chemicals used were reagent grade and used as supplied unless otherwise noted.

TEM images were obtained on carbon-coated copper grids with a Zeiss EM 912Ω instrument at 120 kV. Samples were prepared without staining or with 2% uranyl acetate solution and dried after removal of the excess staining solution. For SEM, samples were prepared on glass substrates and coated with Au/Pd. The SEM measurement was done with a Gemini SEM, LEO 1550 system with cold field emission gun operation at 3 kV. JEOL JSM 7500 F was used to obtain Cryo-SEM images with frozen and Pt-coated droplet samples. Atomic force microscopy investigation was performed with a Multimode Nanoscope IIIa, Bruker and JPK NanoWizard 4. Images were attained with a conventional tapping mode and flattened without further modification. Qualitative imaging (QI) mode was applied for nanoindentation with a silicon or silicon nitride cantilever. With JPK data processing software, Nanowizard 4, force-distance curves were fit to the Hertz model and manipulated to obtain Young's modulus. Fluorescence and bright filed images were acquired with a LEICA DMi8 Confocal Laser Microscope. Fluorescence spectra and fluorescence quantum yield were measured with a Jasco FP-8300 spectrofluorometer. Excitation was performed with a Xe lamp. Emission spectra for the quantum yield measurements were collected with excitation at 360 nm and detection from 350 to 900 nm with an integrating sphere setup. The emission quantum yield was calculated considering two regions: (1) 350-372 nm (excitation beam) and (2) 380-700 nm (sample fluorescence). Absorption spectra were collected with a SHIMADZU UV-vis spectrophotometer (UV-2600). Polarized optical microscope images were obtained with an Olympus BX41 (40X) system. For XRD measurements, a Bruker D8 Advanced X-ray diffractometer with Cu Kα radiation was used. Circular dichroism (CD) spectra were acquired with a Chrascan qCD spectrometer (Applied Photophysics Ltd. Leatherhead, UK) using a quartz cuvette (Helma GmbH & Co. KG, Mullheim, Germany) at RT with a band width of 1 nm. The samples were directly dried in the quartz cuvette. The thioflavin T (ThT) fluorescence was measured at room temperature using a SpectraMax M5 plate reader (Molecular Devices LLC., California, USA) with an excitation wavelength at 438 nm with a cut-off filter at 475 nm. The 5 day-matured samples were incubated with the ThT solution with the final concentration of 20 μM for 30 minutes and stirred 10 seconds right before the measurement.

For microED analysis, transmission electron microscopy was performed using a JEM-2100Plus (JEOL Ltd., Japan) equipped with a GATAN Rio16 CMOS camera, operated at an accelerating voltage at 200 kV. Drops of aqueous suspensions of crystallites were deposited on glow-discharged carbon-coated copper grids. All the measurements were carried out at a cryogenic temperature with an Elsa cryo-transfer holder (Gatan Inc., USA) to protect the electron sensitive **13-D(S)** crystals. All electron micrographs and electron diffraction patterns were recorded on a Gatan Rio 16 camera (Gatan Inc., USA). Low-dose bright-field imaging and microED measurements were achieved using the SerialEM program. The tilt-series experiments were performed with an increment angle of 0.1° and an overall rotation of about 40°. A selected area aperture with a diameter of 200 nm was inserted. A focused electron probe with a diameter of about

100 nm was used to follow the twist geometry of **13-D(S)** crystals. The camera length was calibrated using a powder ED pattern of evaporated aluminum. The microED patterns were analyzed using the Fiji program and in-house scripts. The tilt-series ED patterns were remapped in reciprocal space to determine the unit cell parameters. The image alignments and 3D reconstructions were done using IMOD software suit. The tomograms were visualized using 3dmod. The microED and electron tomography analysis is done by Dr. Y. Ogawa. The 3D cartoons of the ribbon in **Figure 3-10A** were made with Blender v2.82.

7. References

[1] G. M. Whitesides, B. Grzybowski, *Science* **2002**, *295*, 2418-2421.

[2] a) A. C. Mendes, E. T. Baran, R. L. Reis, H. S. Azevedo, *WIREs Nanomedicine and Nanobiotechnology* **2013**, *5*, 582-612; b) A. Levin, T. A. Hakala, L. Schnaider, G. J. Bernardes, E. Gazit, T. P. Knowles, *Nat. Rev. Chem.* **2020**, *4*, 615-634; c) E. De Santis, M. G. Ryadnov, *Chem. Soc. Rev.* **2015**, *44*, 8288-8300.

[3] a) J. Wang, K. Liu, R. Xing, X. Yan, *Chem. Soc. Rev.* **2016**, *45*, 5589-5604; b) M. Kwak, A. Herrmann, *Chem. Soc. Rev.* **2011**, *40*, 5745-5755; c) M. Delbianco, P. Bharate, S. Varela-Aramburu, P. H. Seeberger, *Chem. Rev.* **2016**, *116*, 1693-1752.

[4] A. S. Mahadevi, G. N. Sastry, *Chem. Rev.* **2016**, *116*, 2775-2825.

[5] J. D. Badjić, A. Nelson, S. J. Cantrill, W. B. Turnbull, J. F. Stoddart, *Acc. Chem. Res.* **2005**, *38*, 723-732.

[6] P. W. K. Rothemund, *Nature* **2006**, *440*, 297-302.

[7] A. D. Malay, N. Miyazaki, A. Biela, S. Chakraborti, K. Majsterkiewicz, I. Stupka, C. S. Kaplan, A. Kowalczyk, B. M. A. G. Piette, G. K. A. Hochberg, D. Wu, T. P. Wrobel, A. Fineberg, M. S. Kushwah, M. Kelemen, P. Vavpetič, P. Pelicon, P. Kukura, J. L. P. Benesch, K. Iwasaki, J. G. Heddle, *Nature* **2019**, *569*, 438-442.

[8] a) M. R. Ghadiri, J. R. Granja, R. A. Milligan, D. E. McRee, N. Khazanovich, *Nature* **1993**, *366*, 324; b) J. D. Hartgerink, E. Beniash, S. I. Stupp, *Science* **2001**, *294*, 1684-1688; c) S. Bera, S. Mondal, S. Rencus-Lazar, E. Gazit, *Acc. Chem. Res.* **2018**, *51*, 2187-2197; d) K. Tao, P. Makam, R. Aizen, E. Gazit, *Science* **2017**, *358*, eaam9756.

[9] a) P. W. K. Rothemund, *Nature* **2006**, *440*, 297; b) H. Dietz, S. M. Douglas, W. M. Shih, *Science* **2009**, *325*, 725-730; c) Y. Ke, L. L. Ong, W. M. Shih, P. Yin, *Science* **2012**, *338*, 1177-1183; d) M. R. Jones, N. C. Seeman, C. A. Mirkin, *Science* **2015**, *347*, 1260901.

[10] a) L. Adler-Abramovich, L. Vaks, O. Carny, D. Trudler, A. Magno, A. Caflisch, D. Frenkel, E. Gazit, *Nat. Chem. Biol.* **2012**, *8*, 701; b) M. J. Webber, E. A. Appel, E. W. Meijer, R. Langer, *Nat. Mater.* **2015**, *15*, 13; c) Q. Hu, H. Li, L. Wang, H. Gu, C. Fan, *Chem. Rev.* **2018**, 10.1021/acs.chemrev.1027b00663.

[11] a) K. Tao, Z. Fan, L. Sun, P. Makam, Z. Tian, M. Ruegsegger, S. Shaham-Niv, D. Hansford, R. Aizen, Z. Pan, S. Galster, J. Ma, F. Yuan, M. Si, S. Qu, M. Zhang, E. Gazit, J. Li, *Nat. Commun.* **2018**, *9*, 3217; b) X. Lan, Q. Wang, *Npg Asia Materials* **2014**, *6*, e97.

[12] P. W. Rothemund, *Nature* **2006**, *440*, 297-302.

[13] a) F. Praetorius, B. Kick, K. L. Behler, M. N. Honemann, D. Weuster-Botz, H. Dietz, *Nature* **2017**, *552*, 84-87; b) S. Dey, C. Fan, K. V. Gothelf, J. Li, C. Lin, L. Liu, N. Liu, M. A. Nijenhuis, B. Saccà, F. C. Simmel, *Nature Reviews Methods Primers* **2021**, *1*, 1-24; c) F. Hong, F. Zhang, Y. Liu, H. Yan, *Chem. Rev.* **2017**, *117*, 12584-12640.

[14] W. Zhang, S. Mo, M. Liu, L. Liu, L. Yu, C. Wang, *Frontiers in Chemistry* **2020**, *8*, 1008.

[15] a) K. A. Dill, J. L. MacCallum, *Science* **2012**, *338*, 1042-1046; b) E. Khan, S. K Mishra, A. Kumar, *Protein and peptide letters* **2017**, *24*, 331-339.

[16] S. Liu, K. J. Edgar, *Biomacromolecules* **2015**, *16*, 2556-2571.

[17] A. Varki; R. Cummings; J. Esko; H. Freeze; P. Stanley; G. Hart; P.H. Seeberger, *Essentials of glycobiology*, 3rd ed., Cold Spring Harbor Laboratory Press, Cold Spring Harbor, N.Y., **2017**.

[18] J. Rojo, J. C. Morales, S. Penadés, in *Host-Guest Chemistry: Mimetic Approaches to Study Carbohydrate Recognition* (Ed.: S. Penadés), Springer Berlin Heidelberg, Berlin, Heidelberg, **2002**, pp. 45-92.

[19] Y. C. Lee, R. T. Lee, *Acc. Chem. Res.* **1995**, *28*, 321-327.

[20] C. Fasting, C. A. Schalley, M. Weber, O. Seitz, S. Hecht, B. Koksch, J. Dernedde, C. Graf, E.-W. Knapp, R. Haag, *Angew. Chem., Int. Ed.* **2012**, *51*, 10472-10498.

[21] J. L. Jiménez Blanco, C. Ortiz Mellet, J. M. García Fernández, *Chem. Soc. Rev.* **2013**, *42*, 4518-4531.

[22] a) M. Marradi, F. Chiodo, I. García, S. Penadés, *Chem. Soc. Rev.* **2013**, *42*, 4728-4745; b) Y. M. Chabre, R. Roy, *Chem. Soc. Rev.* **2013**, *42*, 4657-4708; c) F. Sansone, A. Casnati, *Chem. Soc. Rev.* **2013**, *42*, 4623-4639; d) L. L. Kiessling, J. C. Grim, *Chem. Soc. Rev.* **2013**, *42*, 4476-4491.

[23] a) Y. Habibi, L. A. Lucia, O. J. Rojas, *Chem. Rev.* **2010**, *110*, 3479-3500; b) R. M. Parker, G. Guidetti, C. A. Williams, T. Zhao, A. Narkevicius, S. Vignolini, B. Frka-Petesic, *Adv. Mater.* **2018**, *30*, 1704477; c) D. Klemm, F. Kramer, S. Moritz, T. Lindström, M. Ankerfors, D. Gray, A. Dorris, *Angew. Chem., Int. Ed.* **2011**, *50*, 5438-5466; d) P.-X. Wang, W. Y. Hamad, M. J. MacLachlan, *Nat. Commun.* **2016**, *7*, 11515; e) P.-X. Wang, W. Y. Hamad, M. J. MacLachlan, *Angew. Chem., Int. Ed.* **2016**, *55*, 12460-12464.

[24] a) P. Hassanzadeh, M. Kharaziha, M. Nikkhah, S. R. Shin, J. Jin, S. He, W. Sun, C. Zhong, M. R. Dokmeci, A. Khademhosseini, M. Rolandi, *J. Mater. Chem. B* **2013**, *1*, 4217-4224; b) M. Rolandi, R. Rolandi, *Adv. Colloid Interface Sci.* **2014**, *207*, 216-222; c) C. Zhong, A. Kapetanovic, Y. Deng, M. Rolandi, *Adv. Mater.* **2011**, *23*, 4776-4781.

[25] a) S. C. Fox, B. Li, D. Xu, K. J. Edgar, *Biomacromolecules* **2011**, *12*, 1956-1972; b) T. Liebert, S. Hornig, S. Hesse, T. Heinze, *J. Am. Chem. Soc.* **2005**, *127*, 10484-10485.

[26] D. Klemm, B. Heublein, H.-P. Fink, A. Bohn, *Angew. Chem. Int. Ed.* **2005**, *44*, 3358-3393.

[27] a) K. E. Broaders, S. Grandhe, J. M. J. Fréchet, *J. Am. Chem. Soc.* **2011**, *133*, 756-758; b) E. M. Bachelder, T. T. Beaudette, K. E. Broaders, J. Dashe, J. M. J. Fréchet, *J. Am. Chem. Soc.* **2008**, *130*, 10494-10495.

[28] J. P. F. Lagerwall, C. Schütz, M. Salajkova, J. Noh, J. Hyun Park, G. Scalia, L. Bergström, *Npg Asia Materials* **2014**, *6*, e80.

[29] I. F. Almeida, T. Pereira, N. H. C. S. Silva, F. P. Gomes, A. J. D. Silvestre, C. S. R. Freire, J. M. Sousa Lobo, P. C. Costa, *Eur. J. Pharm. Biopharm.* **2014**, *86*, 332-336.

[30] a) A. C. Ruthes, F. R. Smiderle, M. Iacomini, *Carbohydr. Polym.* **2015**, *117*, 753-761; b) M. Garcia-Vaquero, G. Rajauria, J. V. O'Doherty, T. Sweeney, *Food Research International* **2017**, *99*, 1011-1020.

[31] a) I. Cumpstey, *ISRN Organic Chemistry* **2013**, *2013*, 27; b) K. Jedvert, T. Heinze, *Journal of Polymer Engineering* **2017**, *37*, 845.

[32] D. Klemm, B. Heublein, H. P. Fink, A. Bohn, *Angew. Chem., Int. Ed.* **2005**, *44*, 3358-3393.

[33] R. J. Moon, A. Martini, J. Nairn, J. Simonsen, J. Youngblood, *Chem. Soc. Rev.* **2011**, *40*, 3941-3994.

[34] B. Thomas, M. C. Raj, J. Joy, A. Moores, G. L. Drisko, C. m. Sanchez, *Chemical Reviews* **2018**, *118*, 11575-11625.

[35] H. Kargarzadeh, M. Mariano, D. Gopakumar, I. Ahmad, S. Thomas, A. Dufresne, J. Huang, N. Lin, *Cellulose* **2018**, *25*, 1-39.

[36] D. Roy, M. Semsarilar, J. T. Guthrie, S. Perrier, *Chem. Soc. Rev.* **2009**, *38*, 2046-2064.

[37] a) Y. Guo, X. Wang, X. Shu, Z. Shen, R.-C. Sun, *J. Agric. Food Chem.* **2012**, *60*, 3900-3908; b) L. Dai, C.-L. Si, *Mater. Lett.* **2017**, *207*, 213-216.

[38] W. Thongsomboon, D. O. Serra, A. Possling, C. Hadjineophytou, R. Hengge, L. Cegelski, *Science* **2018**, *359*, 334-338.

[39] D. O. Serra, R. Hengge, in *Extracellular Sugar-Based Biopolymers Matrices*, Springer, **2019**, pp. 355-392.

[40] J. Jeffries, G. G. Fuller, L. Cegelski, *Microbiology insights* **2019**, *12*, 1178636119865234.

[41] I. Aranaz, M. Mengíbar, R. Harris, B. Miralles, N. Acosta, L. Calderón, Á. Sánchez, Á. Heras, *Current Chemical Biology* **2014**, *8*, 27-42.

[42] a) S. Ifuku, *Molecules* **2014**, *19*, 18367-18380; b) S. S. Silva, J. F. Mano, R. L. Reis, *Green Chemistry* **2017**, *19*, 1208-1220.

[43] C. Zhong, A. Cooper, A. Kapetanovic, Z. Fang, M. Zhang, M. Rolandi, *Soft Matter* **2010**, *6*, 5298-5301.

[44] B. Duan, X. Zheng, Z. Xia, X. Fan, L. Guo, J. Liu, Y. Wang, Q. Ye, L. Zhang, *Angewandte Chemie International Edition* **2015**, *54*, 5152-5156.

[45] S. N. Pawar, K. J. Edgar, *Biomaterials* **2012**, *33*, 3279-3305.

[46] a) N. Gour, C. S. Purohit, S. Verma, R. Puri, S. Ganesh, *Biochemical and Biophysical Research Communications* **2009**, *378*, 503-506; b) M. Salim, O. K. Abou-Zied, H. U. Kulathunga, A. Baskaran, U. R. Kuppusamy, R. Hashim, *RSC Adv.* **2015**, *5*, 55536-55543; c) J.-H. Ryu, E. Lee, Y.-b. Lim, M. Lee, *J. Am. Chem. Soc.* **2007**, *129*, 4808-4814.

[47] S. Gim, Y. Zhu, P. H. Seeberger, M. Delbianco, *WIRES Nanomed. Nanobi.* **2019**, *11*, e1558.

[48] a) A. Mitra, V. Sarkar, B. Mukhopadhyay, *ChemistrySelect* **2017**, *2*, 9958-9961; b) M. Mathiselvam, D. Loganathan, B. Varghese, *RSC Adv.* **2013**, *3*, 14528; c) B. P. Krishnan, S. Raghu, S. Mukherjee, K. M. Sureshan, *Chemical Communications* **2016**, *52*, 14089-14092; d) X. Guan, K. Fan, T. Gao, A. Ma, B. Zhang, J. Song, *Chemical Communications* **2016**, *52*, 962-965; e) M. J. Clemente, P. Romero, J. L. Serrano, J. Fitremann, L. Oriol, *Chem. Mater.* **2012**, *24*, 3847-3858; f) A. Chen, I. S. Okafor, C. Garcia, G. Wang, *Carbohydrate Research* **2018**, *461*, 60-75; g) N. P. Pathak, T. Halder, S. Dhara, S. Yadav, *Chemistry–A European Journal* **2017**, *23*, 11323-11329.

[49] S. Ustun Yaylaci, M. Sardan Ekiz, E. Arslan, N. Can, E. Kilic, H. Ozkan, I. Orujalipoor, S. Ide, A. B. Tekinay, M. O. Guler, *Biomacromolecules* **2016**, *17*, 679-689.

[50] G. Crini, *Chem. Rev.* **2014**, *114*, 10940-10975.

[51] a) F. Bellia, D. La Mendola, C. Pedone, E. Rizzarelli, M. Saviano, G. Vecchio, *Chem. Soc. Rev.* **2009**, *38*, 2756-2781; b) Q. D. Hu, G. P. Tang, P. K. Chu, *Acc. Chem. Res.* **2014**, *47*, 2017-2025; c) A. Martinez, C. Ortiz Mellet, J. M. Garcia Fernandez, *Chem. Soc. Rev.* **2013**, *42*, 4746-4773; d) B. V. Schmidt, C. Barner-Kowollik, *Angew. Chem., Int. Ed.* **2017**, *56*, 8350-8369; e) G. Wenz, *Angew. Chem., Int. Ed.* **1994**, *33*, 803-822.

[52] B. Kang, T. Opatz, K. Landfester, F. R. Wurm, *Chem. Soc. Rev.* **2015**, *44*, 8301-8325.

[53] a) H. S. Hahm, M. K. Schlegel, M. Hurevich, S. Eller, F. Schuhmacher, J. Hofmann, K. Pagel, P. H. Seeberger, *Proceedings of the National Academy of Sciences* **2017**, *114*, E3385-E3389; b) M. Panza, S. G. Pistorio, K. J. Stine, A. V. Demchenko, *Chem. Rev.* **2018**, *118*, 8105-8150; c) A. Pardo-Vargas, M. Delbianco, P. H. Seeberger, *Curr. Opin. Chem. Biol.* **2018**, *46*, 48-55; d) L. Wen, G. Edmunds, C. Gibbons, J. Zhang, M. R. Gadi, H. Zhu, J. Fang, X. Liu, Y. Kong, P. G. Wang, *Chemical Reviews* **2018**, *118*, 8151-8187.

[54] T. Misono, *Measurement Techniques and Practices of Colloid and Interface Phenomena* **2019**, 65-69.

[55] M. Kaushik, C. Fraschini, G. Chauve, J.-L. Putaux, A. Moores, *Transm. Electron Microsc. Theory Appl* **2015**.

[56] J. Majoinen, J. S. Haataja, D. Appelhans, A. Lederer, A. Olszewska, J. Seitsonen, V. Aseyev, E. Kontturi, H. Rosilo, M. Österberg, N. Houbenov, O. Ikkala, *J. Am. Chem. Soc.* **2014**, *136*, 866-869.

[57] A. Anžlovar, A. Krajnc, E. Žagar, *Cellulose* **2020**, *27*, 5785-5800.

[58] M. Chen, J. Parot, V. A. Hackley, S. Zou, L. J. Johnston, *Cellulose* **2021**, *28*, 1933-1946.

[59] K. Matsuo, H. Namatame, M. Taniguchi, K. Gekko, *Biochemistry* **2009**, *48*, 9103-9111.

[60] a) A. R. Engle, N. Purdie, J. A. Hyatt, *Carbohydrate Research* **1994**, *265*, 181-195; b) K. Conley, M. Whitehead, T. G. van de Ven, *Cellulose* **2017**, *24*, 479-486.

[61] K. M. Conley, L. Godbout, M. T. Whitehead, T. G. van de Ven, *Cellulose* **2017**, *24*, 5455-5462.

[62] a) M. Delbianco, A. Kononov, A. Poveda, Y. Yu, T. Diercks, J. s. Jiménez-Barbero, P. H. Seeberger, *J. Am. Chem. Soc.* **2018**, *140*, 5421-5426; b) P. Valverde, J. I. Quintana, J. I. Santos, A. Ardá, J. Jiménez-Barbero, *ACS Omega* **2019**, *4*, 13618-13630.

[63] C. F. Holder, R. E. Schaak, *ACS Nano* **2019**, *13*, 7359-7365.

[64] B. L. Nannenga, T. Gonen, *Nat. Methods* **2019**, *16*, 369-379.

[65] P. H. Seeberger, *Acc. Chem. Res.* **2015**, *48*, 1450-1463.

[66] a) Y. Yu, A. Kononov, M. Delbianco, P. H. Seeberger, *Chem. Eur. J.* **2018**, *24*, 6075-6078; b) A. A. Joseph, A. Pardo-Vargas, P. H. Seeberger, *J. Am. Chem. Soc.* **2020**, *142*, 8561-8564.

[67] a) L. Adler-Abramovich, E. Gazit, *Chem. Soc. Rev.* **2014**, *43*, 6881-6893; b) Z. L. Pianowski, N. Winssinger, *Chem. Soc. Rev.* **2008**, *37*, 1330-1336.

[68] C. Adelwöhrer, T. Takano, F. Nakatsubo, T. Rosenau, *Biomacromolecules* **2009**, *10*, 2817-2822.

[69] M. Delbianco, A. Kononov, A. Poveda, Y. Yu, T. Diercks, J. Jiménez-Barbero, P. H. Seeberger, *J. Am. Chem. Soc.* **2018**, *140*, 5421-5426.

[70] R. B. Best, G. E. Jackson, K. J. Naidoo, *J. Phys. Chem. B* **2001**, *105*, 4742-4751.

[71] M. R. Nilsson, *Methods* **2004**, *34*, 151-160.

[72] I. Colomer, A. E. R. Chamberlain, M. B. Haughey, T. J. Donohoe, *Nat. Rev. Chem.* **2017**, *1*, 0088.

[73] N. H. Andersen, R. B. Dyer, R. M. Fesinmeyer, F. Gai, Z. Liu, J. W. Neidigh, H. Tong, *J. Am. Chem. Soc.* **1999**, *121*, 9879-9880.

[74] a) O. Berger, L. Adler-Abramovich, M. Levy-Sakin, A. Grunwald, Y. Liebes-Peer, M. Bachar, L. Buzhansky, E. Mossou, V. T. Forsyth, T. Schwartz, Y. Ebenstein, F. Frolow, L. J. W. Shimon, F. Patolsky, E. Gazit, *Nat. Nanotechnol.* **2015**, *10*, 353; b) D. Pinotsi, A. K. Buell, C. M. Dobson, G. S. Kaminski Schierle, C. F. Kaminski, *ChemBioChem* **2013**, *14*, 846-850; c) D. Pinotsi, L. Grisanti, P. Mahou, R. Gebauer, C. F. Kaminski, A. Hassanali, G. S. Kaminski Schierle, *J. Am. Chem. Soc.* **2016**, *138*, 3046-3057; d) J. Shang, L. Ma, J. Li, W. Ai, T. Yu, G. G. Gurzadyan, *Sci. Rep.* **2012**, *2*, 792; e) A. Samanta, *J. Phys. Chem. B* **2006**, *110*, 13704-13716.

[75] a) C. Ren, H. Wang, D. Mao, X. Zhang, Q. Fengzhao, Y. Shi, D. Ding, D. Kong, L. Wang, Z. Yang, *Angew. Chem. Int. Ed.* **2015**, *127*, 4905-4909; b) X. Yu, Y.-C. Gao, H.-W. Li, Y. Wu, *Macromol. Rapid Commun.* **2020**, *41*, 2000198.

[76] Y. Yu, S. Gim, D. Kim, Z. A. Arnon, E. Gazit, P. H. Seeberger, M. Delbianco, *J. Am. Chem. Soc.* **2019**, *141*, 4833-4838.

[77] R. Chhabra, J. Sharma, Y. Liu, S. Rinker, H. Yan, *Adv. Drug Deliv. Rev.* **2010**, *62*, 617-625.

[78] a) C. H. Görbitz, *ChemComm* **2006**, 2332-2334; b) A. Brito, Y. M. Abul-Haija, D. S. Da Costa, R. Novoa-Carballal, R. L. Reis, R. V. Ulijn, R. A. Pires, I. Pashkuleva, *Chem. Sci.* **2019**, *10*, 2385-2390; c) M. Ghosh, S. Bera, S. Schiffmann, L. J. W. Shimon, L. Adler-Abramovich, *ACS Nano* **2020**, *14*, 9990-10000.

[79] a) S. Brahmachari, Z. A. Arnon, A. Frydman-Marom, E. Gazit, L. Adler-Abramovich, *ACS Nano* **2017**, *11*, 5960-5969; b) E. Gazit, *Annu. Rev. Biochem.* **2018**, *87*, 533-553; c) M. Reches, E. Gazit, *Science* **2003**, *300*, 625-627.

[80] E. Gazit, *J. Nanobiotechnology* **2005**, *1*, 286-288.

[81] a) Z. Gan, H. Xu, *Macromol. Rapid Commun.* **2017**, *38*, 1700370; b) X. Yan, P. Zhu, J. Li, *Chem. Soc. Rev.* **2010**, *39*, 1877-1890; c) V. Nguyen, R. Zhu, K. Jenkins, R. Yang, *Nature communications* **2016**, *7*, 1-6.

[82] R. Prathapan, R. F. Tabor, G. Garnier, J. Hu, *ACS Appl. Bio. Mater.* **2020**, *3*, 1828-1844.

[83] a) J. H. Lee, R. M. Brown, S. Kuga, S.-i. Shoda, S. Kobayashi, *PNAS* **1994**, *91*, 7425-7429; b) Y. Yataka, T. Sawada, T. Serizawa, *Langmuir* **2016**, *32*, 10120-10125; c) P. de Andrade, J. C. Muñoz-García, G. Pergolizzi, V. Gabrielli, S. Nepogodiev, D. Iuga, L. Fábián, R. Nigmatullin, M. A. Johns, R. Harniman, **2020**.

[84] J. Morris, J. Bietsch, K. Bashaw, G. Wang, *Gels* **2021**, *7*, 24.

[85] a) A. Kapros, A. Balázs, V. Harmat, A. Háló, L. Budai, I. Pintér, D. K. Menyhárd, A. Perczel, *Chem. Eur. J.* **2020**, *26*, 11643-11655; b) C. He, S. Wu, D. Liu, C. Chi, W. Zhang, M. Ma, L. Lai, S. Dong, *J. Am. Chem. Soc.* **2020**, *142*, 17015-17023; c) R. Liu, R. Zhang, L. Li, Z. Kochovski, L. Yao, M.-P. Nieh, Y. Lu, T. Shi, G. Chen, *J. Am. Chem. Soc.* **2021**.

[86] a) M. Jesus, S. Penadés, *Glycoconj. J.* **2004**, *21*, 149-163; b) S. Gim, G. Fittolani, Y. Nishiyama, P. H. Seeberger, Y. Ogawa, M. Delbianco, *Angew. Chem. Int. Ed.* **2020**, *132*, 22766-22772.

[87] a) Y. Yu, T. Tyrikos-Ergas, Y. Zhu, G. Fittolani, V. Bordoni, A. Singhal, R. J. Fair, A. Grafmüller, P. H. Seeberger, M. Delbianco, *Angew. Chem. Int. Ed.* **2019**, *58*, 13127-13132; b) M. K. Panda, K. Bhaskar Pal, G. Raj, R. Jana, T. Moriwaki, G. D. Mukherjee, B. Mukhopadhyay, P. Naumov, *Cryst. Growth Des.* **2017**, *17*, 1759-1765.

[88] a) J. L. Asensio, A. Ardá, F. J. Cañada, J. Jiménez-Barbero, *Acc. Chem. Res.* **2013**, *46*, 946-954; b) G. Terraneo, D. Potenza, A. Canales, J. Jiménez-Barbero, K. K. Baldridge, A. Bernardi, *J. Am. Chem. Soc.* **2007**, *129*, 2890-2900; c) K. Ramirez-Gualito, R. Alonso-Rios, B. Quiroz-Garcia, A. Rojas-Aguilar, D. Diaz, J. Jimenez-Barbero, G. Cuevas, *J. Am. Chem. Soc.* **2009**, *131*, 18129-18138.

[89] a) Y. Ogawa, J.-L. Putaux, *Cellulose* **2019**, *26*, 17-34; b) R. M. Glaeser, *J. Ultrastruct. Res.* **1971**, *36*, 466-482.

[90] a) C. G. Jones, M. W. Martynowycz, J. Hattne, T. J. Fulton, B. M. Stoltz, J. A. Rodriguez, H. M. Nelson, T. Gonen, *ACS Cent. Scl.* **2018**, *4*, 1587-1592; b) M. Gallagher-Jones, C. Glynn, D. R. Boyer, M. W. Martynowycz, E. Hernandez, J. Miao, C.-T. Zee, I. V. Novikova, L. Goldschmidt, H. T. McFarlane, G. F. Helguera, J. E. Evans, M. R. Sawaya, D. Cascio, D. S. Eisenberg, T. Gonen, J. A. Rodriguez, *Nature Structural & Molecular Biology* **2018**, *25*, 131-134; c) J. A. Rodriguez, M. I. Ivanova, M. R. Sawaya, D. Cascio, F. E. Reyes, D. Shi, S. Sangwan, E. L. Guenther, L. M. Johnson, M. Zhang, L. Jiang, M. A. Arbing, B. L. Nannenga, J. Hattne, J. Whitelegge, A. S. Brewster, M. Messerschmidt, S. Boutet, N. K. Sauter, T. Gonen, D. S. Eisenberg, *Nature* **2015**, *525*, 486-490; d) L. Palatinus, P. Brázda, P. Boullay, O. Perez, M. Klementová, S. Petit, V. Eigner, M. Zaarour, S. Mintova, *Science* **2017**, *355*, 166-169.

[91] a) O. Panova, X. C. Chen, K. C. Bustillo, C. Ophus, M. P. Bhatt, N. Balsara, A. M. Minor, *Micron* **2016**, *88*, 30-36; b) D. N. Johnstone, C. S. Allen, M. Danaie, R. C. Copley, J. Brum, A. I. Kirkland, P. A. Midgley, *Microsc. Microanal.* **2019**, *25*, 1746-1747.

[92] a) J. Sugiyama, R. Vuong, H. Chanzy, *Macromolecules* **1991**, *24*, 4168-4175; b) Y. Nishiyama, P. Langan, H. Chanzy, *J. Am. Chem. Soc.* **2002**, *124*, 9074-9082.

[93] C. Janiak, *Journal of the Chemical Society, Dalton Transactions* **2000**, 3885-3896.

[94] J. Zielkiewicz, *The Journal of chemical physics* **2005**, *123*, 104501.

[95] D. Van Der Spoel, E. Lindahl, B. Hess, G. Groenhof, A. E. Mark, H. J. C. Berendsen, *J. Comput. Chem.* **2005**, *26*, 1701-1718.

[96] a) J. D. Dunitz, A. Gavezzotti, *Angew. Chem. Int. Ed.* **2005**, *44*, 1766-1787; b) G. R. Desiraju, *J. Am. Chem. Soc.* **2013**, *135*, 9952-9967; c) E. R. T. Tiekink, *ChemComm* **2014**, *50*, 11079-11082.

[97] a) I. Usov, G. Nyström, J. Adamcik, S. Handschin, C. Schütz, A. Fall, L. Bergström, R. Mezzenga, *Nature communications* **2015**, *6*, 1-11; b) Y. Ogawa, *Nanoscale* **2019**, *11*, 21767-21774; c) Y. Ogawa, S. Kimura, M. Wada, *J. Struct. Biol.* **2011**, *176*, 83-90.

[98] M. Liu, L. Zhang, T. Wang, *Chem. Rev.* **2015**, *115*, 7304-7397.

[99] K. Nagy-Smith, P. J. Beltramo, E. Moore, R. Tycko, E. M. Furst, J. P. Schneider, *ACS Cent. Scl.* **2017**, *3*, 586-597.

[100] D. M. Raymond, B. L. Nilsson, *Chem. Soc. Rev.* **2018**, *47*, 3659-3720.

[101] S. Bera, B. Xue, P. Rehak, G. Jacoby, W. Ji, L. J. W. Shimon, R. Beck, P. Král, Y. Cao, E. Gazit, *ACS Nano* **2020**, *14*, 1694-1706.

[102] F. Xu, I. J. Khan, K. McGuinness, A. S. Parmar, T. Silva, N. S. Murthy, V. Nanda, *J. Am. Chem. Soc.* **2013**, *135*, 18762-18765.

[103] K. Sakakibara, J. P. Hill, K. Ariga, *Small* **2011**, *7*, 1288-1308.

[104] S. Zhang, *Nature Biotechnology* **2003**, *21*, 1171-1178.

[105] D. F. van der Vliet, C. Wang, D. Tripkovic, D. Strmcnik, X. F. Zhang, M. K. Debe, R. T. Atanasoski, N. M. Markovic, V. R. Stamenkovic, *Nature Materials* **2012**, *11*, 1051-1058.

[106] a) X. Gu, L. Shaw, K. Gu, M. F. Toney, Z. Bao, *Nature Communications* **2018**, *9*, 534; b) Y. Diao, B. C. K. Tee, G. Giri, J. Xu, D. H. Kim, H. A. Becerril, R. M. Stoltenberg, T. H. Lee, G. Xue, S. C. B. Mannsfeld, Z. Bao, *Nature Materials* **2013**, *12*, 665-671.

[107] T. Zhang, H. Qi, Z. Liao, Y. D. Horev, L. A. Panes-Ruiz, P. S. Petkov, Z. Zhang, R. Shivhare, P. Zhang, K. Liu, V. Bezugly, S. Liu, Z. Zheng, S. Mannsfeld, T. Heine, G. Cuniberti, H. Haick, E. Zschech, U. Kaiser, R. Dong, X. Feng, *Nature Communications* **2019**, *10*, 4225.

[108] J. Kao, K. Thorkelsson, P. Bai, Z. Zhang, C. Sun, T. Xu, *Nature Communications* **2014**, *5*, 4053.

[109] a) Z. Qiu, C. Yan, J. Lu, W. Yang, *Macromolecules* **2007**, *40*, 5047-5053; b) H. Kajioka, S. Yoshimoto, K. Taguchi, A. Toda, *Macromolecules* **2010**, *43*, 3837-3843.

[110] a) L. Xu, A. Sharma, S. W. Joo, *Macromolecules* **2012**, *45*, 6628-6633; b) B. J. Berne, J. D. Weeks, R. Zhou, *Annu. Rev. Phys. Chem.* **2009**, *60*, 85–103; c) J. Chen, S. Qin, X. Wu, Chu, P. K, *ACS Nano* **2016**, *10*, 832-838; d) V. Castelletto, A. M. Chippindale, I. W. Hamley, S. Barnett, A. Hasan, K. H. A. Lau, *ChemComm* **2019**, *55*, 5867-5869.

[111] Y. Zhu, T. Tyrikos-Ergas, K. Schiefelbein, A. Grafmüller, P. H. Seeberger, M. Delbianco, *Org. Biomol. Chem.* **2020**, *18*, 1349-1353.

[112] a) S. Purser, P. R. Moore, S. Swallow, V. Gouverneur, *Chem. Soc. Rev.* **2008**, *37*, 320-330; b) J. D. Martínez, A. I. Manzano, E. Calviño, A. d. Diego, B. Rodriguez de Francisco, C. Romanò, S. Oscarson, O. Millet, H.-J. Gabius, J. Jiménez-Barbero, F. J. Cañada, *J. Org. Chem.* **2020**, *85*, 16072-16081.

[113] a) B. Linclau, A. Ardá, N.-C. Reichardt, M. Sollogoub, L. Unione, S. P. Vincent, J. Jiménez-Barbero, *Chem. Soc. Rev.* **2020**, *49*, 3863-3888; b) J. C. Biffinger, H. W. Kim, S. G. DiMagno, *ChemBioChem* **2004**, *5*, 622-627.

[114] a) C. J. Pace, J. Gao, *Acc. Chem. Res.* **2013**, *46*, 907-915; b) T. He, A. Gershenson, S. J. Eyles, Y.-J. Lee, W. R. Liu, J. Wang, J. Gao, M. F. Roberts, *J. Biol. Chem.* **2015**, *290*, 19334-19342.

[115] C. Guan, X. Liu, A. M. Elshahawy, H. Zhang, H. Wu, S. J. Pennycook, J. Wang, *Nanoscale Horiz.* **2017**, *2*, 342-348.

[116] a) P. Makam, E. Gazit, *Chem. Soc. Rev.* **2018**, *47*, 3406-3420; b) I. R. Sasselli, Z. Syrgiannis, *Eur. J. Org. Chem.* **2020**, *2020*, 5305-5318.

[117] T. Shimizu, M. Masuda, *Mol. Cryst.* **1997**, *295*, 197-200.

[118] J. Majoinen, J. Hassinen, J. S. Haataja, H. T. Rekola, E. Kontturi, M. A. Kostiainen, R. H. Ras, P. Törmä, O. Ikkala, *Adv. Mater.* **2016**, *28*, 5262-5267.

[119] S. Gim, G. Fittolani, Y. Yu, Y. Zhu, P. H. Seeberger, Y. Ogawa, M. Delbianco, *Chem. Eur. J.* **2021**.

[120] a) F. T. Bosman, I. Stamenkovic, *The Journal of Pathology* **2003**, *200*, 423-428; b) J. C. Henderson, S. M. Zimmerman, A. A. Crofts, J. M. Boll, L. G. Kuhns, C. M. Herrera, M. S. Trent, *Annual review of microbiology* **2016**, *70*, 255-278.

[121] a) G. Rivas, S. K. Vogel, P. Schwille, *Current Opinion in Chemical Biology* **2014**, *22*, 18-26; b) B. Ramm, P. Schwille, *Microbial biotechnology* **2019**, *12*, 74-76; c) P. Schwille, J. Spatz, K. Landfester, E. Bodenschatz, S. Herminghaus, V. Sourjik, T. J. Erb, P. Bastiaens, R. Lipowsky, A. Hyman, P. Dabrock, J.-C. Baret, T. Vidakovic-Koch, P. Bieling, R. Dimova, H. Mutschler, T. Robinson, T.-Y. D. Tang, S. Wegner, K. Sundmacher, *Angew. Chem. Int. Ed.* **2018**, *57*, 13382-13392.

[122] D. O. Serra, A. M. Richter, R. Hengge, *Journal of bacteriology* **2013**, *195*, 5540-5554.

[123] a) H.-C. Flemming, J. Wingender, U. Szewzyk, P. Steinberg, S. A. Rice, S. Kjelleberg, *Nature Reviews Microbiology* **2016**, *14*, 563-575; b) L. Hall-Stoodley, J. W. Costerton, P. Stoodley, *Nature reviews microbiology* **2004**, *2*, 95-108.

[124] M. M. Barnhart, M. R. Chapman, *Annu. Rev. Microbiol.* **2006**, *60*, 131-147.

[125] H.-C. Flemming, J. Wingender, *Nature Reviews Microbiology* **2010**, *8*, 623-633.

[126] L. Gualdi, L. Tagliabue, S. Bertagnoli, T. Ierano, C. De Castro, P. Landini, *Microbiology* **2008**, *154*, 2017-2024.

[127] J. Jeffries, W. Thongsomboon, J. A. Visser, K. Enriquez, D. Yager, L. Cegelski, *Biopolymers* **2021**, *112*, e23395.

[128] X. Wang, D. R. Smith, J. W. Jones, M. R. Chapman, *J. Biol. Chem.* **2007**, *282*, 3713-3719.

[129] a) S. Tomaselli, V. Esposito, P. Vangone, N. A. J. van Nuland, A. M. J. J. Bonvin, R. Guerrini, T. Tancredi, P. A. Temussi, D. Picone, *ChemBioChem* **2006**, *7*, 257-267; b) N. Hirota, Y. Goto, K. Mizuno, *Protein science* **1997**, *6*, 416-421.

[130] a) P. Lembré, C. Vendrely, P. D. Martino, *Protein and peptide letters* **2013**, *20*, 942-946; b) Q. Qi, T.-X. Zhao, B.-L. An, X.-Y. Liu, C. Zhong, *Chinese Chemical Letters* **2017**, *28*, 1062-1068.

[131] M. Biancalana, S. Koide, *Biochimica et Biophysica Acta (BBA)-Proteins and Proteomics* **2010**, *1804*, 1405-1412.

[132] M. Sleutel, I. Van den Broeck, N. Van Gerven, C. Feuillie, W. Jonckheere, C. Valotteau, Y. F. Dufrêne, H. Remaut, *Nat. Chem. Biol.* **2017**, *13*, 902-908.

[133] M. Biancalana, S. Koide, *Biochimica et Biophysica Acta (BBA) - Proteins and Proteomics* **2010**, *1804*, 1405-1412.

[134] S. L. Gras, L. J. Waddington, K. N. Goldie, in *Protein Folding, Misfolding, and Disease: Methods and Protocols* (Eds.: A. F. Hill, K. J. Barnham, S. P. Bottomley, R. Cappai), Humana Press, Totowa, NJ, **2011**, pp. 197-214.

[135] X. Dai, W. Hou, Y. Sun, Z. Gao, S. Zhu, Z. Jiang, *International journal of molecular sciences* **2015**, *16*, 10526-10536.

[136] C.-C. Liu, N. Zhao, Y. Yamaguchi, J. R. Cirrito, T. Kanekiyo, D. M. Holtzman, G. Bu, *Science Translational Medicine* **2016**, *8*, 332ra344-332ra344.

[137] K. Broersen, W. Jonckheere, J. Rozenski, A. Vandersteen, K. Pauwels, A. Pastore, F. Rousseau, J. Schymkowitz, *Protein Engineering, Design and Selection* **2011**, *24*, 743-750.

[138] O. M. Vanderfleet, E. D. Cranston, *Nat. Rev. Mater.* **2021**, *6*, 124-144.